

Development of an FPGA-based MI sensor system  
for high compatibility and high resolution

Graduate school of engineering, Nagoya university  
SHI KE

2020 年度（令和二年度） 博士論文

FPGA を用いた高互換性と高分解能を実現する  
MI センサーシステムの開発

名古屋大学 工学研究科

電子工学専攻 博士後期課程

史 柯

（内山 研究室）

## **Abstract**

The MI sensor system is studied in this research. Due to the limitation of conventional MI sensor system based on the sample and hold circuit, a novel MI sensor system with an Op-amp integration is proposed in this research. The principle and the structure of the author proposed system are introduced in this thesis. Proposed system is a hybrid analog/digital system developed via FPGA. Therefore, the development of the proposed sensor system consists of two parts (Program and circuit). The characteristic of the proposed sensor system is investigated. As a result, the proposed sensor system shows high resolution and high compatibility with the different types of MI sensors. Additionally, the output of the MI sensor analyzed and discussed in this paper, depending on our calculation, the characteristic of the proposed system is close to our simulation.

## Contents

Chapter 1 Introduction .....	1
1.1 Beginning .....	1
1.2 Magnetic sensors.....	1
1.2.1 Hall effect sensor .....	2
1.2.2 Magneto Resistive (MR) sensor .....	3
1.2.3 Giant-Magneto-Resistance (GMR) sensor .....	4
1.2.4 Tunnel Magneto Resistance (TMR) sensor .....	6
1.2.5 Fluxgate sensor.....	7
1.2.6 Superconducting-Quantum-Interference-Device.....	8
1.3 Magnetic signals and magnetic sensors .....	10
1.4 Characteristics of sensors.....	11
1.5 Summary.....	12
1.6 Outline of the Thesis .....	13
Chapter 2 MI sensor and previous research .....	14
2.1 Introduction.....	14
2.2 Sensing principle.....	14
2.2.1 MI sensor .....	14
2.2.2 Skin effect.....	15
2.2.3 GMI effect .....	17
2.2.4 Demagnetizing field .....	19
2.2.5 Off-diagonal MI sensor .....	20
2.3 Digital devices.....	22
2.3.1 Field-Programmable Gate Array (FPGA) .....	22
2.3.2 Time Analog to Digital Converter (TAD).....	23
2.4 MI sensor system .....	25
2.4.1 CMOS IC type MI sensor system .....	25
2.4.2 FPGA type MI sensor system .....	27
2.4.3 TAD type MI sensor system.....	28
2.4.4 Improved TAD type MI sensor system.....	31

2.5 Discussion .....	33
2.6 Summary .....	36
Chapter 3 Design and method .....	38
3.1 Beginning .....	38
3.2 Op-amp integrator.....	40
3.3 Analog-to-Digital Converter (ADC) .....	41
3.4 System architecture .....	42
3.5 Data analysis .....	44
3.6 System test.....	45
3.7 Summary .....	47
Chapter 4 MI gradiometer .....	48
4.1 Introduction.....	48
4.2 Development.....	48
4.3 Sensor circuit .....	50
4.4 Timing chart.....	52
4.5 Magnetic field to output voltage characteristic .....	53
4.6 Weak magnetic detection .....	55
4.7 Differential signaling .....	56
4.8 System simplification .....	57
4.9 Summary.....	58
Chapter 5 MI magnetometer .....	59
5.1 Improvement of the proposed MI magnetometer .....	59
5.2 Pick-up coil .....	59
5.3 Magnetic field to voltage characteristic .....	65
5.4 Full scale and linearity.....	68
5.5 Noise spectral density .....	71
5.6 Improvement of the proposed MI magnetometer .....	73
5.7 System simplification .....	74
5.8 Summary.....	76
Chapter 6 Conclusions and future outlook .....	77
6.1 Discussion .....	77
6.2 Future work.....	78

6.3 Conclusion.....	79
Acknowledgements.....	82
Appendix.....	83
I. Program of FPGA.....	83
II. Characteristics of ADC with Averaging digital filter .....	90
Publication.....	91

# Chapter 1 Introduction

## 1.1 Beginning

Sensors can be used to sense a lot of different physical quantities such as movement, thermal, optical, magnetic energy, etc. Since the first modern sensor is invented, Innumerable forms of sensors based on a variety of principles have been developed, it is becoming more and more important in our life especially in the Internet of Things (IoT), such as smart devices, autonomous cars, or computers, all of these techniques used sensors. The main purpose of sensors is to collect data from the environment surrounding us. [1]

## 1.2 Magnetic sensors

Magnetic sensor is a device that measures the magnitude, orientation, or relative change of a magnetic field, which is used in many applications, such as Geomagnetic survey, Foreign Matter Detection, or Detection of Biomagnetism. There are several ways to sense magnetic fields, such as mechanical, electronic, and spintronic.

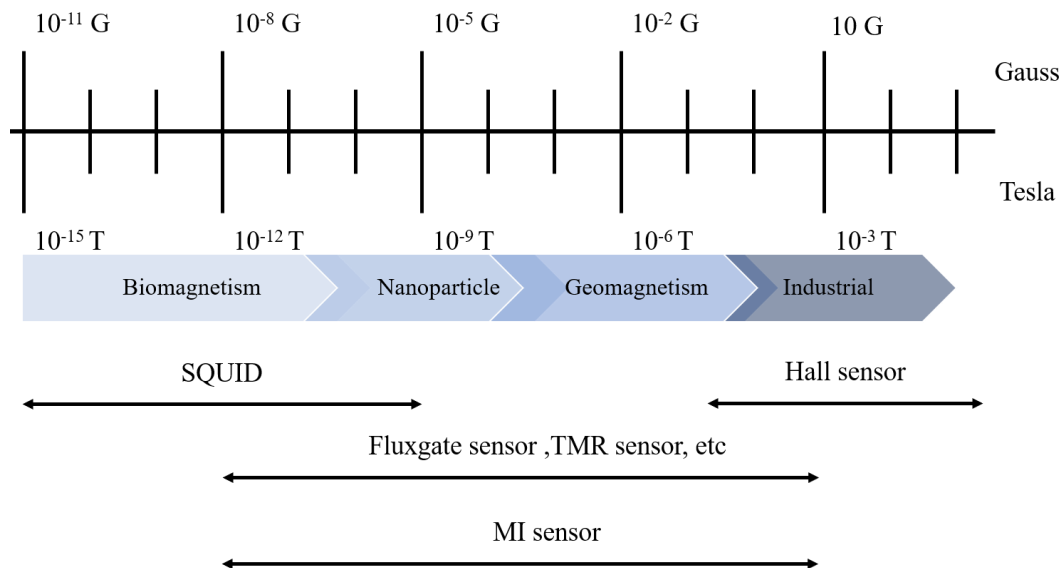


**Fig. 1.1 The magnetic field in our world and dynamic range of various magnetic sensors.**

Hall sensors are commonly used in the magnetism of industry (milli Tesla), high accuracy magnetic sensor like Tunnel Magneto Resistance (TMR) sensors, Fluxgate sensors are generally used in weak magnetism detection field (micro Tesla, nano Tesla, pico Tesla), Superconducting-Quantum-Interference-Device (SQUID) is an ultra-sensitivity magnetic sensor capable of measuring very weak bio-magnetic fields (femto Tesla), as shown in Fig. 1.1. [2]

### 1.2.1 Hall effect sensor

A magnetic field with a perpendicular portion is set to a charge with  $q$  and moving with a velocity of  $V$ , the charge is subjected to an induced force directed at right angles to the plane spanned by  $V$  and  $B$ , as shown in Fig.1.2 It was found by Lorentz experimentally in the 19th century. The induced force is defined as Lorentz force and the magnitude of Lorentz force was found to be proportional to:

$$F = qV \times B \quad (1.1)$$

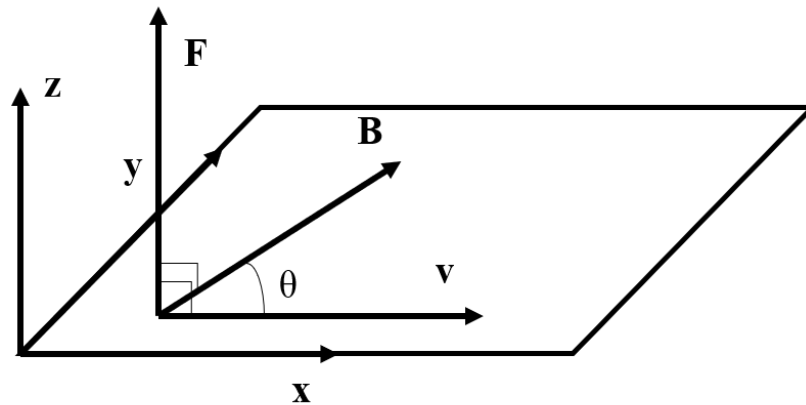
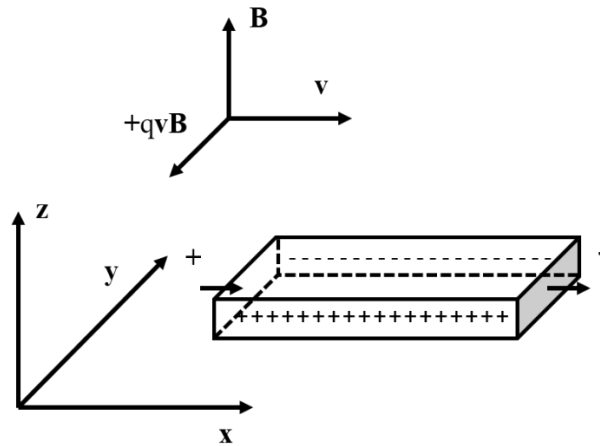


Fig. 1.2 Schematic of the Lorentz force.

Current in conductor and semiconductor consists of the movement of carriers, typically electrons, holes, or ions. A magnetic field with a perpendicular portion is set to a conductor or semiconductor, the moving paths of carriers in the current curved due to Lorentz force. Thus, carriers accumulate on one side of the samples, equal and opposite carriers accumulated on the other side. The carriers in the sample are

influenced by both electric field and magnetic field to reach a steady-state, so a steady electric potential proportional to magnitude of the applied magnetic field is established as long as the carriers are flowing through the sample. It was observed in 1879 by Edwin Hall, and defined as the Hall effect. Hall effect sensor is a device to sense magnitude of an applied magnetic field based on Hall effect which is schematically depicted in Fig. 1.3.



**Fig. 1.3 Schematic of the hall effect sensor.**

## 1.2.2 Magneto Resistive (MR) sensor

The relation between the electrical resistance of the material (often ferromagnetic) and an applied magnetic field is defined as magneto resistivity. The movement of electrons in materials influenced by the electromagnetic phenomena caused by an applied magnetic field. Thus, variation of resistance depending on magnitude of the applied magnetic field is referred to as:

$$MR = \frac{R(H) - R(H = 0)}{R(H = 0)} = \frac{\Delta R}{R} \quad (1.2)$$

The  $R(H)$  (often expressed as a percentage) is the resistance of the material with an applied magnetic field  $H$ . Thus, sensitivity of magneto resistive effects is defined as:

$$S = \frac{\Delta R}{R} / H_s \quad (1.3)$$

The sensitivity  $S$  is express as % / Oe and  $H_s$  is the minimum value of the applied magnetic field which causes saturation of magneto resistive effect.

Generally, electrons forced by Lorentz force in an applied field lead to the movement trajectories of electrons in non-magnetic metals changes. Thus, the free path of electrons between two collisions is reduced which leads to an increase of the resistance in non-magnetic metals, as depicted in Fig.1.4. Variation of resistance depending on the Lorentz force is defined as positive or normal magnetoresistance. [3]

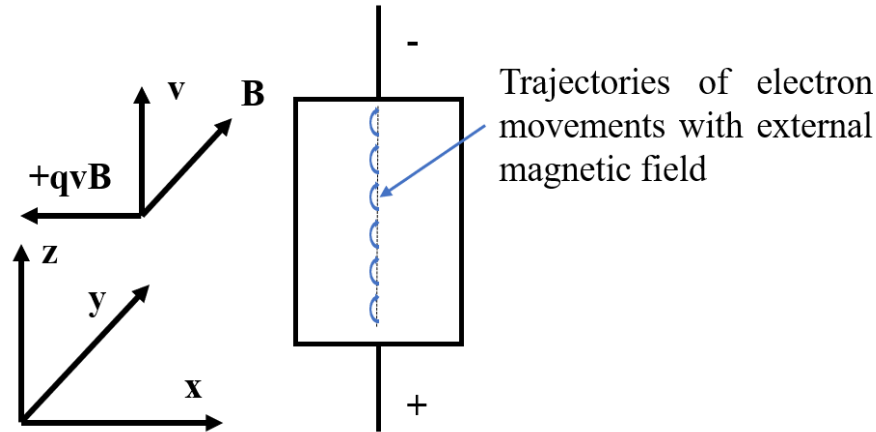


**Fig. 1.4 Principle of the Magneto Resistive sensor.**

### 1.2.3 Giant-Magneto-Resistance (GMR) sensor

The Giant magnetoresistance is observed in the ferromagnetic layers which are separated by a non-magnetic or an antiferromagnetic metallic thin film by A. Fert and P. Grunberg as shown in Fig.1.5. [4] [5] The giant magnetoresistance can be explained through the behavior of the spin-resolved density of states in the Stoner model as depicted in Fig.1.6.

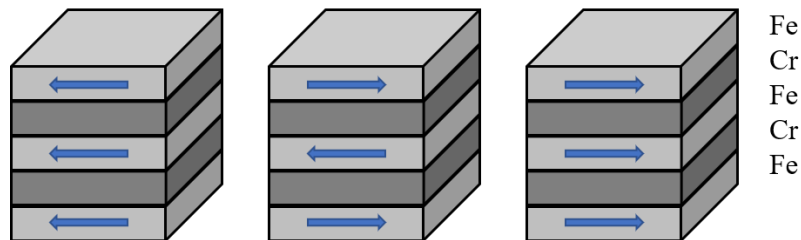


**Fig. 1.5 Schematic of the Giant Magneto Resistive sensor.**

The effective mass of 4s electrons lower than that of 3d electrons. Therefore, the transmission of electricity is carried out by electrons (4s). A high density of states (Dos)

of electrons (3d) at Fermi energy leads to electrons (4s) scattered into empty Dos of the electrons (3d). Owing to the exchange splitting of the Dos for electrons (3d). The scattering odds for an antiparallel alignment in both side of ferromagnetic thin films is much higher than that for the parallel alignment. Therefore, the resistivity of the ferromagnetic multilayer depends on the relative orientations of magnetization in the thin-film system. [3]

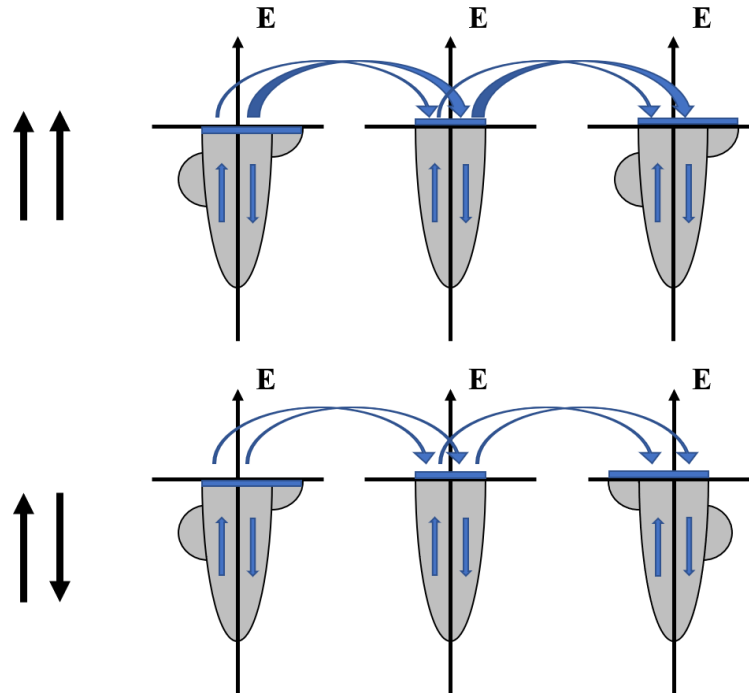


**Fig. 1.6 Transmission of the electrons with up spin and down spin in the Stoner model depending on the relative orientation of the magnetization of the multilayer.**

Parallel orientation of ferromagnetic multilayer depending on the applied magnetic field, thus, the resistance changes with the external magnetic field significantly. Compare to the normal magnetoresistance, this significant variation is defined as the "Giant" MagnetoResistance effect (GMR).

The resistivity of the ferromagnetic multilayer can be explained using the spin channel model as shown in Fig.1.7 The total resistance  $R$  is determined by the parallel connection of the resistance for majority electrons  $R_{\uparrow}$  and minority electrons  $R_{\downarrow}$  as:

$$R = \frac{R_{\uparrow} \cdot R_{\downarrow}}{R_{\uparrow} + R_{\downarrow}} \quad (1.4)$$

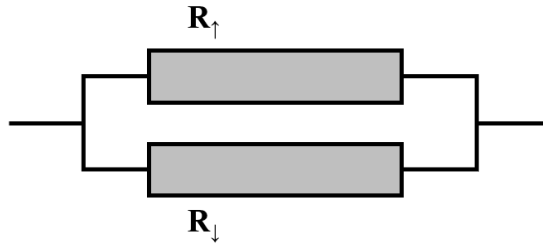


**Fig. 1.7 Spin channel model.**

Therefore, the equivalent circuit diagram of the ferromagnetic multilayer with parallel and antiparallel relative orientation is shown in Fig.1.8. The channel corresponds to spin up and spin down shown different resistivity due to the parallel or antiparallel relative orientation. Due to its parallel relative orientation, the resistivity corresponds to spin up is low and spin down is high, as shown in the left of Fig.1.8. As for the right of Fig.1.8. Due to its antiparallel relative orientation, the resistivity corresponds to spin up and down is high. [3]

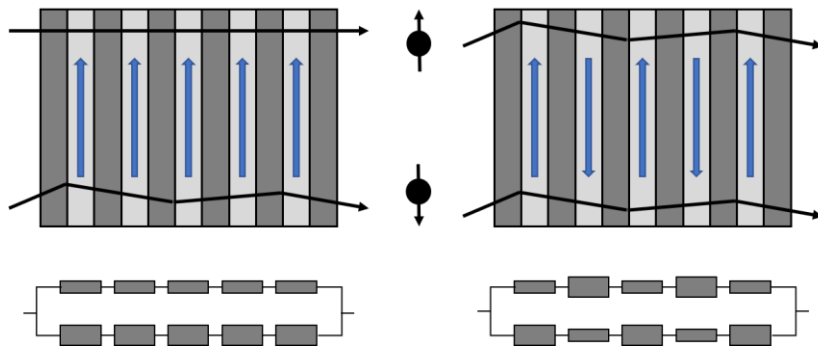


**Fig. 1.8 The equivalent circuit diagram of the ferromagnetic multilayer.**

### 1.2.4 Tunnel Magneto Resistance (TMR) sensor

The thin film for separating ferromagnetic layers in GMR was replaced with an insulating barrier, as shown in Fig.1.9. The thickness of the insulating barrier is thin enough to allow quantum tunneling. Thus, the electric current only depends on quantum mechanical tunneling instead of diffusive transport. The electron remains the spin orientation after quantum mechanical tunneling. The tunneling current depends on the

relative magnetization of two ferromagnetic thin layers is shown in Fig.1.10. The entire resistivity for the antiparallel orientation is higher than that for the parallel orientation, it is similar to GMR but with a higher variation in resistivity. [3] [6] [7]

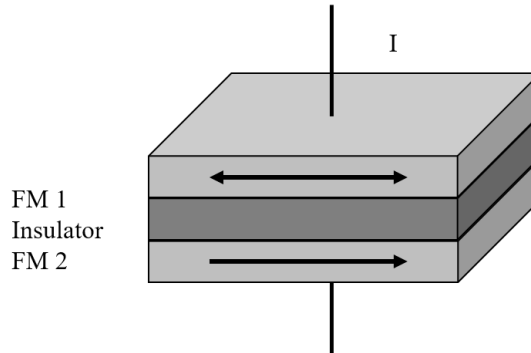


**Fig. 1.9 The structure of Tunnel Magneto Resistance sensor.**

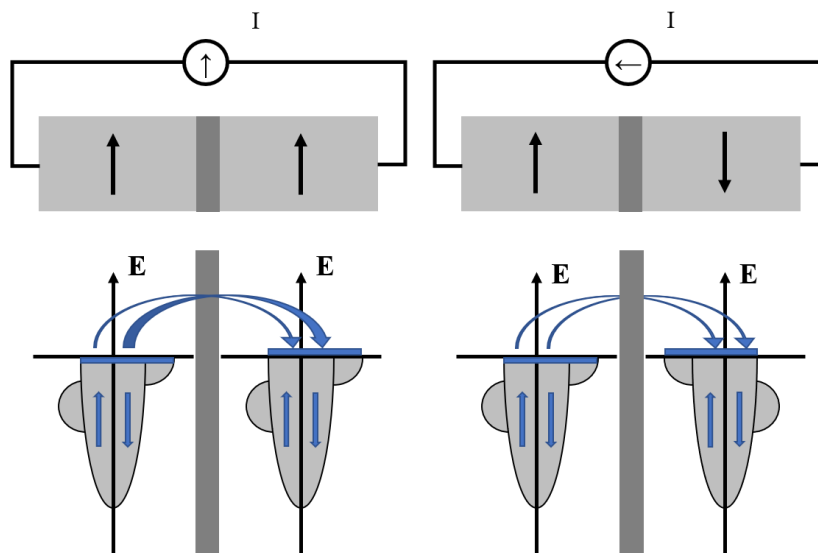


**Fig. 1.10 Transmission of the electrons with up spin and down spin in the Stoner model.**

### 1.2.5 Fluxgate sensor

The fluxgate sensor was invented by G. Goubau and H. Aschenbrenner in 1936, it was used in Project Apollo and World War II. [8] [9] The Fluxgate sensor generally consists of a high permeability core surrounded by coils (exciting coil and pick-up coil), as shown in Fig.1.11(a). The exciting coil is driven by an alternating current which leads to an alternating cycle of magnetic saturation in the permeability core, as shown in

Fig.1.11(b)(1). The saturation of the core depends on the alignment of the applied magnetic field (parallel or antiparallel), it is easy to achieve saturated in alignment with the parallel magnetic field and hard in antiparallel orientation, as depicted in Fig.1.11(b)(2). One of the cores gets the saturation state induced a change in magnetic flux in pick-up coil, as shown in Fig.1.11(b)(3). The change in magnetic flux detected by pick up coil as depicted in Fig.1.11(b)(4). Generally, output in pick-up coil integrated by an integral circuit, thus the output of integrator circuit proportional to the magnetic field. [10]

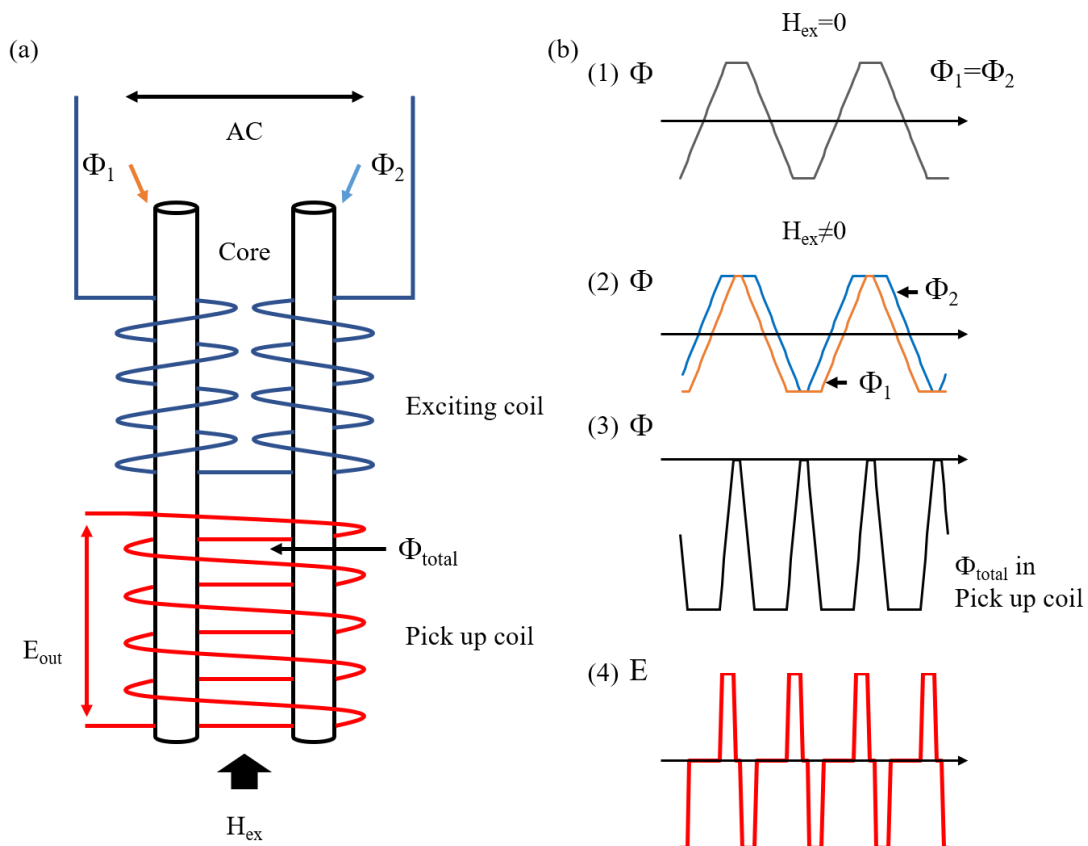


**Fig. 1.11 (a) Basic schematic of FluxGate. (b) Operation mode of FluxGate.**

## 1.2.6 Superconducting-Quantum-Interference-Device

SQUID (Superconducting-Quantum-Interference-Device) is an ultra-resolution magnetometer based on superconducting loops containing Josephson junctions, as shown in Fig.1.13(a) A Josephson junction is a quantum mechanical device that is two

parts of superconductors separated by a thin slice of an insulator, as shown in Fig.1.12(a). At zero flux, due to tunneling, a direct current crossing the insulator, the magnitude of this DC Josephson current depending on the phase difference of wavefunctions of the two superconductors. The voltage of the Josephson junction varies as current until the current is reduced to critical current  $I_c$  or lower after which the voltage drops to zero rather sharply, as shown in Fig.1.12(b).

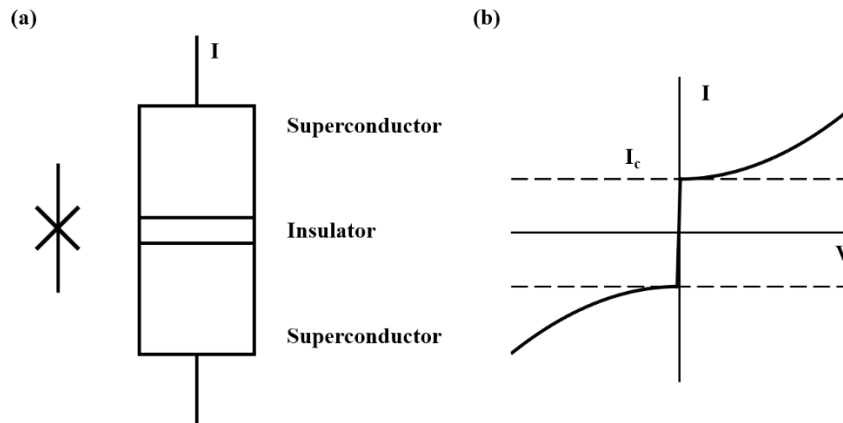


**Fig. 1.12 (a) Structure of the Josephson junction. (b) Current–voltage characteristic of the Josephson junction.**

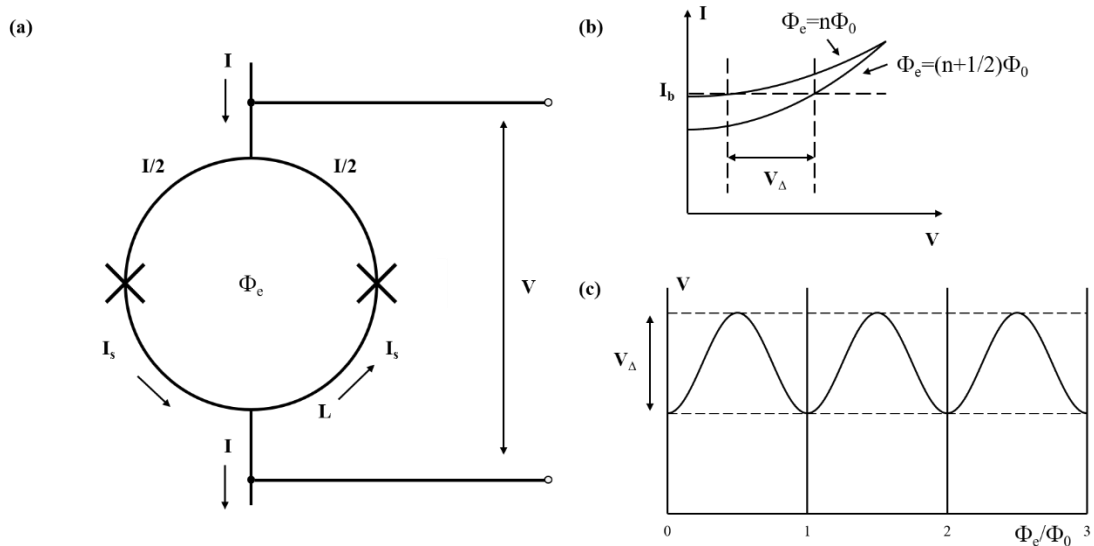


**Fig. 1.13 (a) The basic structure (superconductor rings) of the DC SQUID. (b) The effect of the applied magnetic field on current-voltage characteristics. (c) Magnetic field to output voltage characteristic.**

The phase of current change must be an integer multiple of  $2\pi$  in the superconductor

rings like the electron in atoms orbital. The magnetic flux threading the superconductor rings is quantized like the orbits of electrons in atoms are quantized. A screening current  $I_s$  induced by an external magnetic field  $\Phi_e$ . The input current  $I$  split into the two sides equally, as shown in Fig.1.13(a). Thus, the current in the superconductor rings became  $I/2 + I_s$  and  $I/2 - I_s$ . When the DC SQUID is biased with a current  $2I_b$  ( $I_b > I_c$ ), a voltage appears across the junction while the magnetic field swing between  $\Phi_e = n\Phi_0$  and  $\Phi_e = (n+1/2)\Phi_0$ , as shown in Fig.1.13(b). Consequently, the voltage of Josephson junction to swing between two extrema which we can measure. as shown in Fig.1.13(c). [11] [12] [13]

### 1.3 Magnetic signals and magnetic sensors

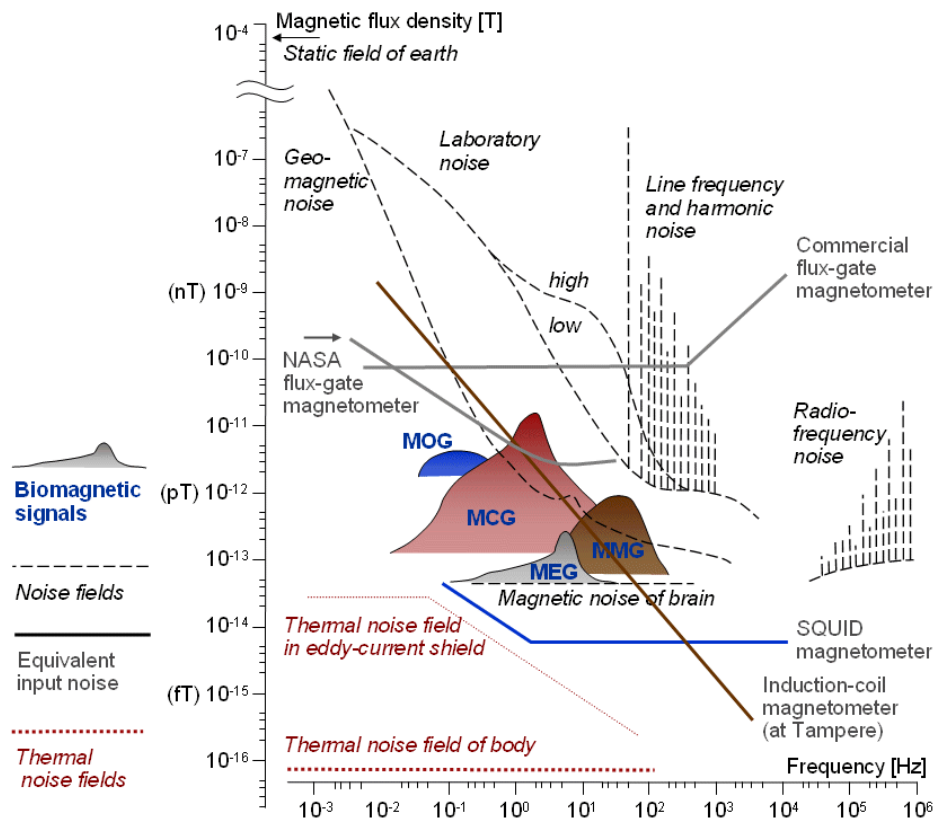


Fig. 1.14 Magnetic signals produced by various sources.

The magnetic signal around us with different frequencies and amplitudes is produced by various sources, as shown in Fig.1.14. The magnitude of magnetic field in Earth from 20 micro Tesla ( $\mu T$ ) to 80  $\mu T$  according to the location, and the oscillation of

magnetic field in Earth is about 100 nano Tesla(nT), and variations of magnetic field owing to magnetic anomalies can be down to pico tesla (pT) level. [14]

Magnetic sensors we discussed before is widely used in various applications. Each of these techniques has advantages and limitations. [15] [16] Hall sensors can be integrated into chips easily with low cost but poor sensitivity. SQUID is the only instrument that is sensitive enough for high-quality biomagnetic measurements. In order to maintain superconductivity, the entire device needs to operate within a low temperature, the cost is too expensive and the entire system is bulky.

## 1.4 Characteristics of sensors

There are several important characteristics of sensors:

- i. Sensitivity: The sensitivity is the derivative of the output with respect to the input physical quantity.
- ii. Range: The range of the sensor is the maximum and minimum values of input physical quantity that can be measured.
- iii. Precision: The precision is the reproducibility of measurement or the result of measurement will maintain the same level with the same input physical quantity.
- iv. Resolution: The Resolution is defined as to produce a standardized output change required the minimum input physical quantity change.
- v. Accuracy: The accuracy of a sensor indicates how much the sensor signal correctly represents the measured physical quantity.
- vi. Offset: An offset means the difference between the actual output value and the ideal output.
- vii. Linearity: The degree of the actual measured curve of a sensor resemblance to a straight line.
- viii. Hysteresis: The value of a physical quantity lags behind changes in the effect causing it.
- ix. Response Speed: The time required for a sensor to react to a new input physical quantity.

The smart devices of the Internet of Things (IoT) to acquire the chemical and physical parameters surrounding us through sensors. In this scenario, sensors in smart devices with the characteristics of micro size, low-power consumption, and low-cost are becoming one of the main priorities. Only in this way, sensors can be integrated aside with a System on a Chip (SoC).

There is a brief comparison between MI sensor and some other magnetic sensors, as shown in Fig.1.15. [17] [18]

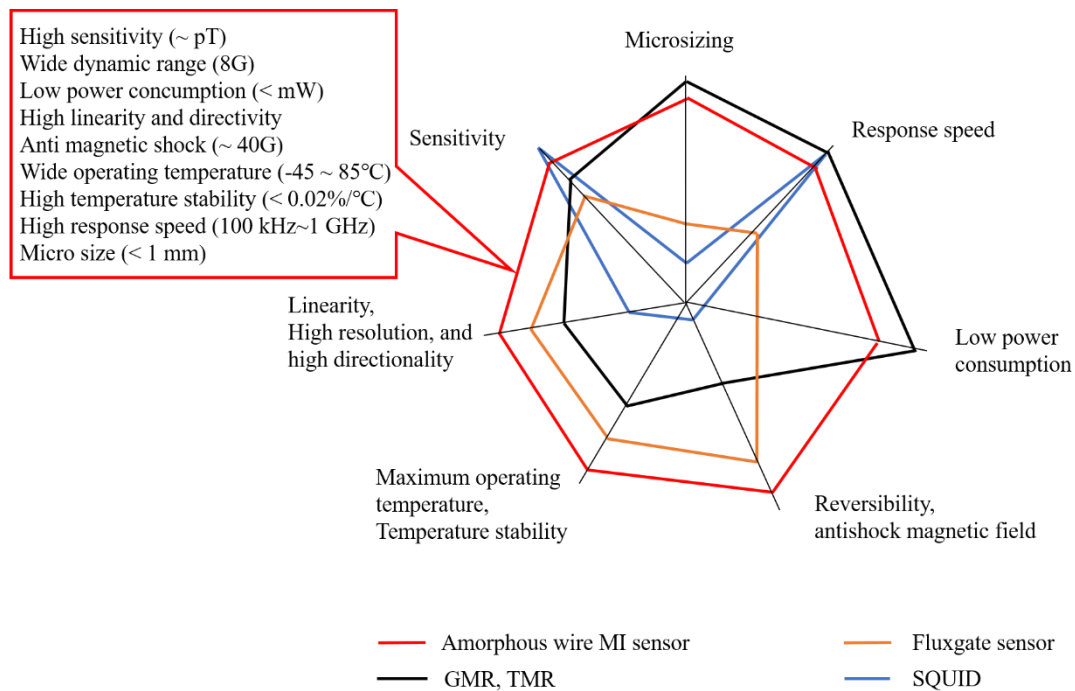


**Fig. 1.15 Comparison of seven sensor features among magnetic sensors.**

## 1.5 Summary

Magnetic-impedance (MI) or Giant Magneto-Impedance (GMI) sensor is a magnetic sensor based on Magnetic-impedance effect with High Sensitivity, Fast speed Response, and Low Power Consumption. MI sensor has a Wide Dynamic Range, from the magnetism of industry (milli Tesla) to the magnetism of the living body(pico Tesla), which can be expected to be used in autonomous vehicles, wearable computers, and biomagnetic detection.

The MI sensors show great potentials for IoT. The purpose of this research is to

improve the MI sensor system to suitable the future applications of IoT.

## **1.6 Outline of the Thesis**

In chapter 1: The background, such as magnetic signals and applications of the magnetic sensor is introduced. The history and comparison of magnetic sensors are surveyed. Due to the requirements of the sensors in future applications, the purpose of this research is proposed.

In chapter 2: Detail and principle of the MI sensor are discussed, the system of the MI sensor and the previous research is discussed. The limitation of the conventional system in future applications is discussed. Thus, the purpose of this research is to improve the limitations of conventional systems.

In chapter 3: The previous research of the author is introduced. So as to improve limitation of sample/hold type MI sensor, a novel system is proposed by combining the conventional system and the author's previous research. The design of an improved MI sensor system and experimental procedures are explained.

In chapter 4: The proposed system is designed and discussed, after the operation of the proposed system is confirmed, the MI gradiometer based on the proposed system is studied and tested.

In chapter 5: So as to improve capability of the author proposed system to be applied to the biomagnetic measurement, the proposed system is investigated and improved. The magnetometer based on the improved proposed system is studied.

In chapter 6: The conclusion and discussion of this research.

# Chapter 2 MI sensor and previous research

## 2.1 Introduction

The MI sensor technology is based on the amorphous wire. Unlike the crystals, the arrangement of atoms without long-range order in materials is called amorphous solid. The Magneto Impedance effect that impedance of soft magnetic materials was influenced by the external magnetic field was first observed in the 1930s. [19] [20] Similar phenomena in amorphous wire was observed in the 1990s, but the impedance of amorphous wire that driven by a high-frequency AC varies significantly with the external magnetic field, in order to distinguish from the phenomena observed in the 1930s, it is defined as Giant Magneto Impedance. [21] [22]

## 2.2 Sensing principle

### 2.2.1 MI sensor

The amorphous wire used in MI sensor technology produced by using the rapidly quenched spinning method in rotating water. Due to this unique method, the magnetic anisotropy of the outer shell and the inner core of the amorphous wire is different. The magnetic anisotropy of the inner core was induced by the shape of the inner core. The direction of the easy axis of magnetization is the circumferential direction at the surface of the wire, thus, it can be easily magnetized by applied magnetic field and current, as depicted in Fig.2.1. [10]

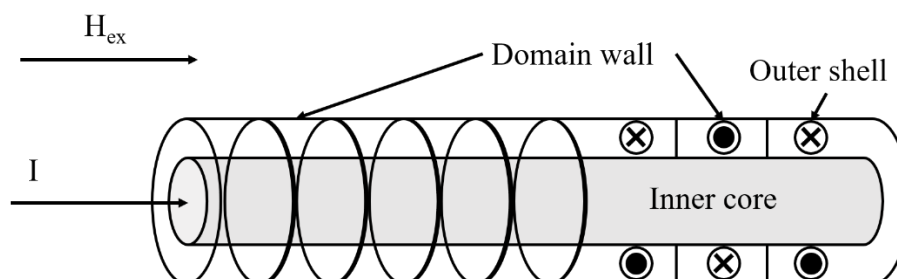
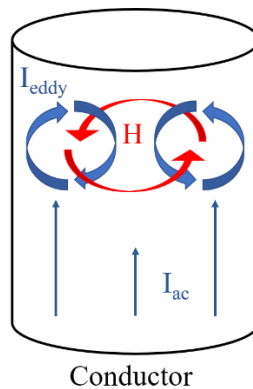


Fig. 2.1 Domain wall model of amorphous wire.

## 2.2.2 Skin effect

When an alternating current (AC) flows through a conductor, the distribution of the current is almost concentrated at the surface of the conductor. Different from the direct current (DC), an alternating magnetic field induced by the alternating current lead to an eddy current, due to this mechanism, the current close to the inner of the conductor was depressed by the eddy current, and the current close to the surface was enhanced by this eddy current, as depicted in Fig.2.2. [10]



**Fig. 2.2 Illustration of the skin effect in the conductor.**

Magnetic field and electric field at surface of the conductor is schematically in Fig.2.3.

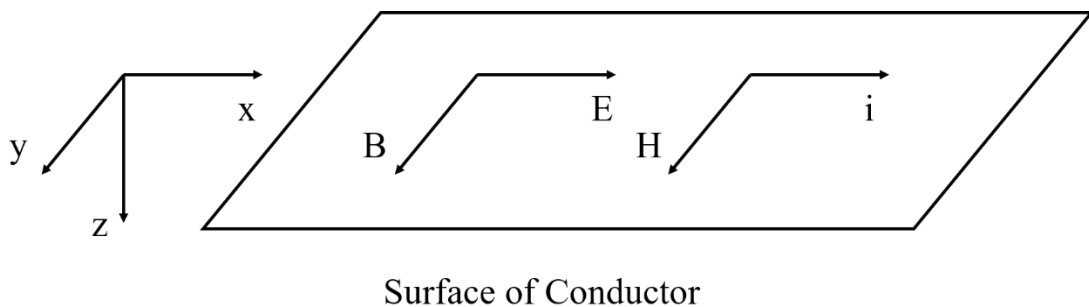


**Fig. 2.3 The surface model of the conductor.**

Skin effect can be explained using Maxwell's equations by:

$$\nabla \times \mathbf{E} = -\frac{\partial \mathbf{B}}{\partial t} \quad (2.1)$$

$$\nabla \times \mathbf{H} = \mathbf{i} \quad (2.2)$$

$$\nabla \cdot \mathbf{B} = 0 \quad (2.3)$$

$$\nabla \cdot \mathbf{i} = 0 \quad (2.4)$$

$$\mathbf{B} = \mu \mathbf{H} \quad (2.5)$$

$$\mathbf{E} = \rho \mathbf{i} \quad (2.6)$$

The magnetic field is a function of  $z$  in the  $y$ -direction. The electric field is a function of  $x$  in the  $z$ -direction.

$$\frac{\partial E_x}{\partial z} = -\frac{\mu \partial H_y}{\partial t} \quad (2.7)$$

$$-\frac{\partial H_y}{\partial z} = \frac{1}{\rho} E_x \quad (2.8)$$

By using Maxwell's equations, we obtain:

$$\frac{\partial^2 E_x}{\partial z^2} - \frac{\mu}{\rho} \cdot \frac{\partial E_x}{\partial t} = 0 \quad (2.9)$$

$$\frac{\partial^2 H_y}{\partial z^2} - \frac{\mu}{\rho} \cdot \frac{\partial H_y}{\partial t} = 0 \quad (2.10)$$

The alternating electric field can be considered as  $E_x(z) = E_m \exp(-j\omega t)$ , we obtain:

$$\frac{\partial^2 E_x}{\partial z^2} + j \frac{\omega \mu}{\rho} E_x = 0 \quad (2.11)$$

The alternating electric field related to  $z$ -direction and time can be defined as  $E_x(z) = A \exp(-kz) \cdot \exp(-j\omega t)$  and Substituted into Equation, we obtain:

$$E_x(z) = E_m \exp\left(-\frac{z}{\delta}\right) \cdot \exp\left\{-j\left(\omega t - \frac{z}{\delta}\right)\right\} \quad (2.12)$$

$$\delta = \sqrt{\frac{2\rho}{\omega\mu}} \quad (2.13)$$

The distribution of current can be calculated by:

$$|I| = \int |i(r)| 2\pi r dr \quad (2.14)$$

The current  $i(r)$  in equation is:

$$|i(r)| = \left| \frac{E_m}{\rho} \right| \exp\left(\frac{r-a}{\delta}\right) \quad (2.15)$$

Thus, the distribution of applied magnetic field of conductor is:

$$|H(r)| = \frac{|I(r)|}{2\pi r} \quad (2.16)$$

Due to the skin effect, the magnetic field in conductor is concentrated at the surface of the conductor, as depicted in Fig.2.4.

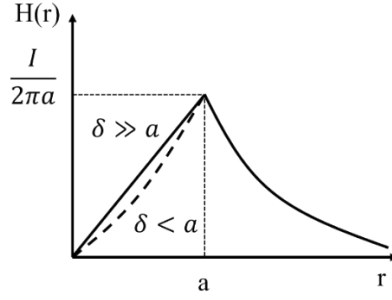


**Fig. 2.4 Distribution of magnetic field in conductor.**

### 2.2.3 GMI effect

The GMI effect in the amorphous wire can be explained by using Maxwell's equations too. A wire with radius  $a$ , length  $l$ , and resistance  $\rho$  flowthrough an alternating current  $I = I_m \exp(j\omega t)$ , the magnetic and electric field of amorphous wire schematically in Fig.2.5. [10]

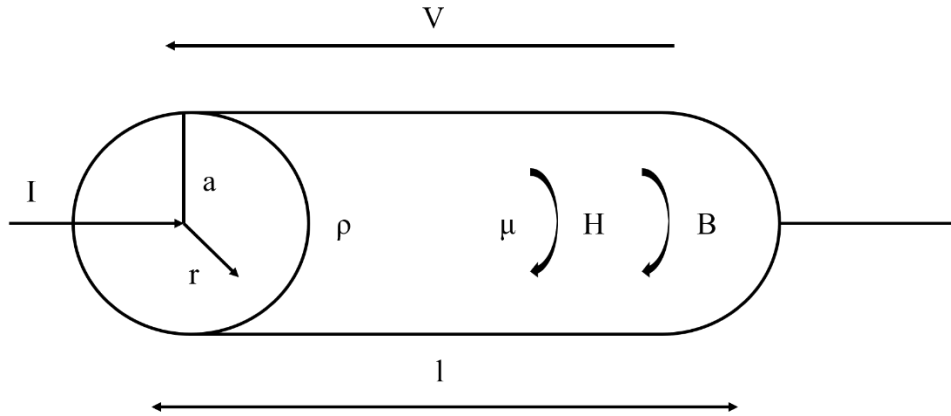


**Fig. 2.5. Schematic of amorphous wire driven by AC current.**

The Maxwell's equations in the wire are given by (2.1) to (2.6).

The magnetic field in the circumferential direction is  $H = H_m \exp(j\omega t)$ , we obtain:

$$\nabla \times E = -j\omega\mu H \quad (2.17)$$

$$\nabla \times \nabla \times E = -j \frac{\omega\mu}{\rho} E \quad (2.18)$$

According to the formula:

$$\nabla \times \nabla \times A = \nabla(\nabla \cdot A) - \nabla^2 A \quad (2.19)$$

We obtain:

$$\nabla \times \nabla \times E = \nabla(\nabla \cdot E) - \nabla^2 E \quad (2.20)$$

The electric field in the long axis is given by:

$$E = E_z \quad (2.21)$$

Thus, E can be calculated by:

$$\nabla^2 E_z - j \frac{\omega \mu}{\rho} E_z = 0 \quad (2.22)$$

Because E is related to r only, thus, E can be expressed into cylindrical coordinates by:

$$\Delta E_z = \frac{1}{r} \frac{\partial}{\partial r} \left( r \frac{\partial E_z}{\partial r} \right) \quad (2.23)$$

Substitute the equation into the equation, we obtain:

$$\frac{1}{r} \frac{\partial}{\partial r} \left( r \frac{\partial E_z}{\partial r} \right) + k^2 E_z = 0 \quad (2.24)$$

$$\frac{\partial^2 E_z}{\partial r^2} + \frac{\partial E_z}{r \partial r} + k^2 E_z = 0 \quad (2.25)$$

Here.

The equation can be calculated by using the Bessel's equation:

$$y'' + \frac{y'}{x} + \left(1 - \frac{\nu}{x^2}\right) y = 0 \quad (2.26)$$

The E can be expressed as:

$$E_z(r) = A J_0(kr) = \frac{E_z(a)}{J_0(ka)} J_0(kr) \quad (2.27)$$

The relation between magnetic and electric field can be obtained using the equation in cylindrical coordinates as:

$$\nabla \times E = -j\omega\mu H = -\frac{\partial E_z}{\partial r} \quad (2.28)$$

We obtain:

$$H = -\frac{j}{\omega\mu} \cdot \frac{\partial E_z}{\partial r} \quad (2.29)$$

The equation can be calculated by using A, we obtain:

$$H(r) = \frac{jkA}{\omega\mu} J_1(kr) \quad (2.30)$$

$$H(a) = \frac{jkA}{\omega\mu} J_1(ka) = \frac{I}{2\pi a} \quad (2.31)$$

Thus, the E can be expressed as:

$$E_z(a) = -\frac{j\omega\mu J_0(ka)I}{2\pi ka J_1(ka)} \quad (2.32)$$

The power consumption of the wire can be calculated by using Poynting vector  $E \times \bar{H}$  and  $V\bar{I}$  as:

$$V\bar{I} = -\iint (E \times \bar{H}) ds = \iiint iE dv + \frac{\partial}{\partial t} \iiint \frac{\mu H^2}{2} dv = E_z(a)\overline{H(a)}2\pi al = E_z(a)l\bar{I} \quad (2.33)$$

Thus, the impedance of the wire can be expressed as:

$$Z = \frac{V}{I} = \frac{E_z(a)l}{I} = -j \frac{\omega\mu J_0(ka)}{2\pi ka J_1(ka)} \cdot \frac{ka}{ka} = \frac{1}{2} R_{dc} ka \frac{J_0(ka)}{J_1(ka)} \quad (2.34)$$

When the frequency of the alternating current is high enough, the impedance of the wire can be expressed as:

$$Z \approx \frac{a}{2\sqrt{2\rho}} R_{dc} (1 + j) \sqrt{\omega\mu} \quad (2.35)$$

The value of the permeability  $\mu$  depends on magnitude of external magnetic field, thus, impedance of the wire also changes with the applied magnetic field, by using this way, a magnetic quantity converted to an electrical quantity, as shown in Fig.2.6. [18]

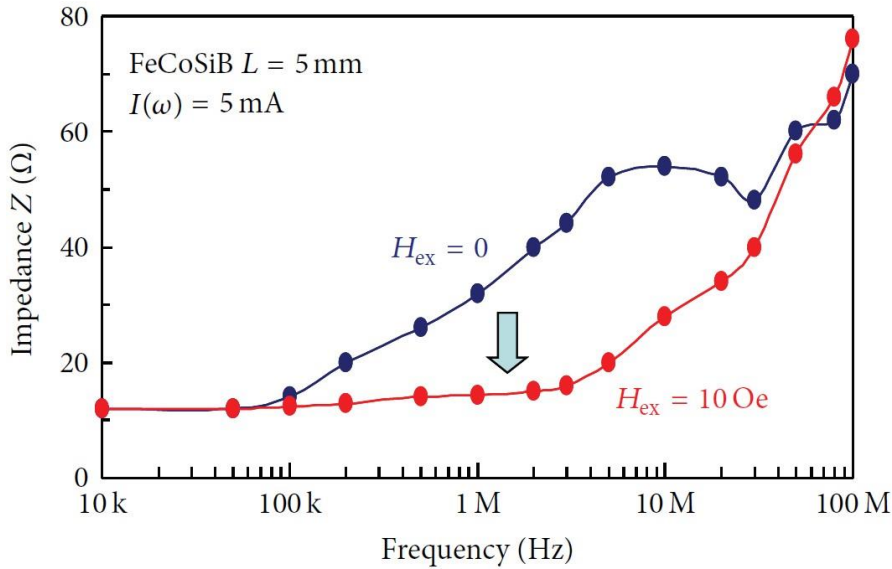


**Fig. 2.6. Giant Magneto-Impedance Effect.**

## 2.2.4 Demagnetizing field

In order to develop the high-performance micro-size sensor, there is a need for minifying the size of the MI sensor. Both demagnetizing field and noise of the amorphous wire is from the inner core, as shown in Fig. 2.7, the demagnetizing field in

the cylindrical type magnetic material can be expressed as:

$$H_{dem}(x) = \frac{a^2}{4} \left\{ \left( \frac{l}{2} - x \right)^{-2} + \left( \frac{l}{2} + x \right)^{-2} \right\} \quad (2.36)$$

Thus, the sensitivity of the MI sensor depressed by minifying the length of the amorphous wire. It is hard to maintain the high sensitivity of the MI sensor with micro size. On the other hand, one of the disadvantages of the MI sensor is non-linearity. So as to fix non-linearity problem in MI sensor, a direct magnetic field source need to be set aside for the MI sensor like the GMR sensor. In addition, the output of the sensor needs to be improved by a feedback circuit. [10]

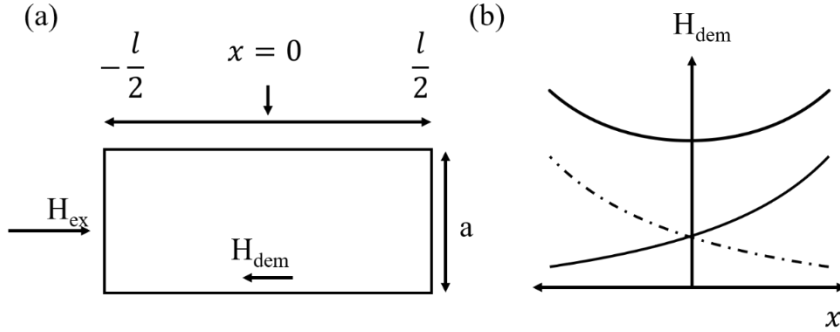


**Fig. 2.7. (a) Model of the demagnetizing field in the amorphous wire. (b) Distribution of demagnetizing field.**

### 2.2.5 Off-diagonal MI sensor

So as to fix non-linearity problem of MI sensor, a new principle of MI sensor was invented by using a pick-up coil. [10] [23] The new type of MI sensor composed of amorphous wire wrapped by pick-up coil, as shown in Fig.2.8.

Compare with the magneto impedance sensor, the ratio between the voltage induced in pick-up coil and the current flow through amorphous wire is defined as off-diagonal impedance as:

$$Z_C = \frac{V_C}{I} \quad (2.37)$$

Thus, the new type of MI sensor is also called off-diagonal GMI sensor. The alternating current flow through the amorphous wire was replaced by a pulse current,

thus, the pulse current generated by a CMOS-IC which can be easily integrated. The power consumption of pulse current can be adjusted by changing the frequency of it.

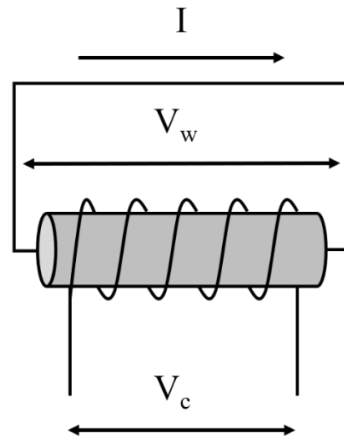


**Fig. 2.8 Structure of the Off-diagonal MI sensor.**

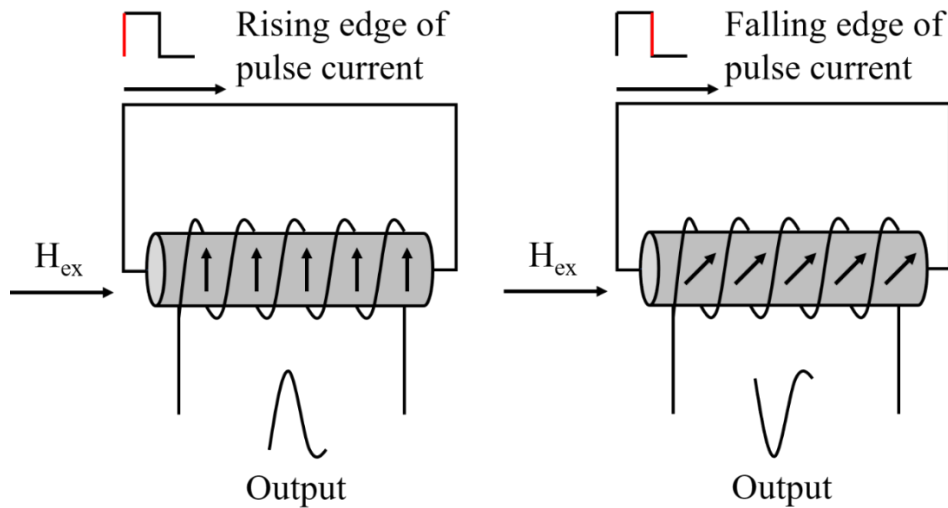


**Fig. 2.9 Operation of the Off-diagonal MI sensor.**

Basic principle of off-diagonal MI sensor is shown in Fig.2.9. Due to skin effect, the direction of magnetization at the surface of the amorphous wire is controlled by a pulse current flowthrough it. The direction of magnetization changes into the circumferential direction at the rising edge of the pulse current. As for the falling edge, direction of magnetization changes through the external magnetic field. The magnetic flux in the pick-up coil changes alternately, due to Lenz's law, an induced voltage output by the pick-up coil can be expressed as:

$$e_p = N \frac{\Delta\Phi}{t_r} \quad (2.38)$$

A high sensitivity microsensor with high linearity was invented in 1997, a reliable MI sensor with high-temperature stability was invented in 1999 by using analog switches. The MI sensor was commercialized by Aichi Steel Corporation in 2005 and wild used in smartphones and wearable devices, etc. [16][17][18] Three types of MI sensor system has been developed before:

- 1) CMOS IC type.
- 2) FPGA type.
- 3) TAD type.

## **2.3 Digital devices**

### **2.3.1 Field-Programmable Gate Array (FPGA)**

In the previous research, A Field-Programmable Gate Array (FPGA) is used to develop the MI sensor system. FPGA is an integrated circuit and the function of FPGA can be reconfigured infinitely by using a hardware description language (HDL). Once the function is configured by the HDL, the FPGA can be considered as an application-specific integrated circuit (ASIC), therefore, FPGA play a remarkable role in the development of the embedded system.

Generally, the FPGA consists of plenty of logic gates interconnected by the wire, the information of connection can be reconfigured by HDL and saved in the memory. The FPGA communicates with other devices via In/Out pin (I/O pin), as shown in Fig.2.10.

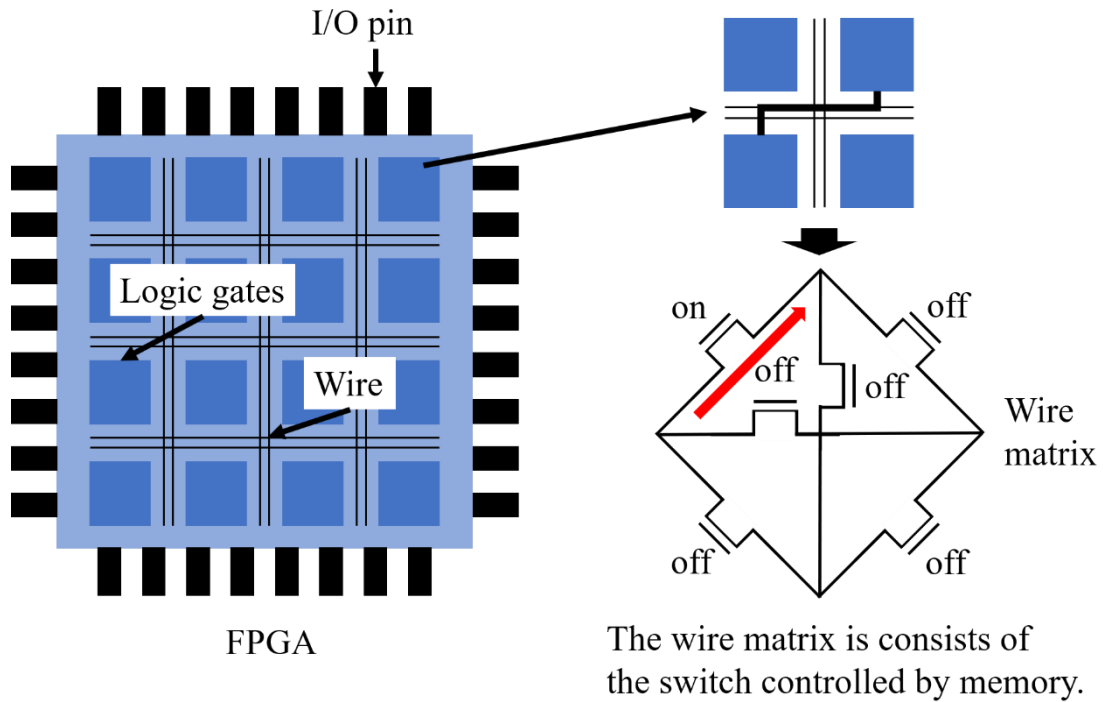


**Fig. 2.10 Basic structure of the FPGA.**

### 2.3.2 Time Analog to Digital Converter (TAD)

Generally, output of sensor circuit is a non-digital signal, in order to transfer it to a digital signal which we can use. A device called Analog to Digital Converter (ADC) is used to achieve A/D conversion. [24] [25] A time-based ADC called Time Analog-to-Digital converter (TAD) have been used in previous research. [26]

TAD is an all-digital A/D converter that the entire ADC consists of a digital circuit. An analog signal is converted to a digital signal in TAD via Delay Unit. The schematic of TAD depicted in Fig.2.11. It takes time for an input pulse signal output by the Delay Unit, the delay time  $T_d$  is expressed as:

$$T_d = AV_{in}(V_{in} - V_{th})^a: a = 1.4 \text{ to } 1.6 \quad (2.39)$$

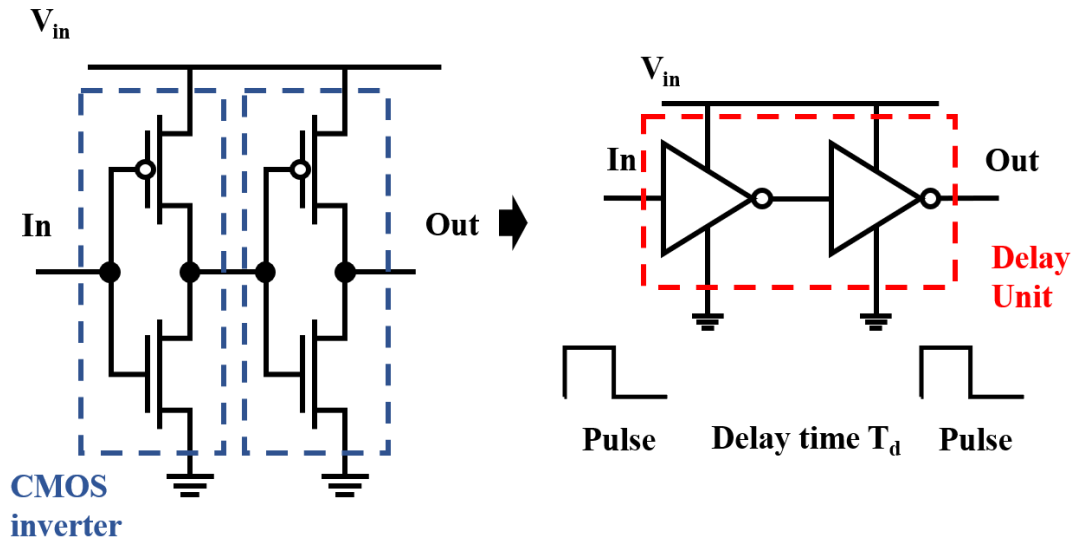


Fig. 2.11 Basic structure of the Delay Unit Line.

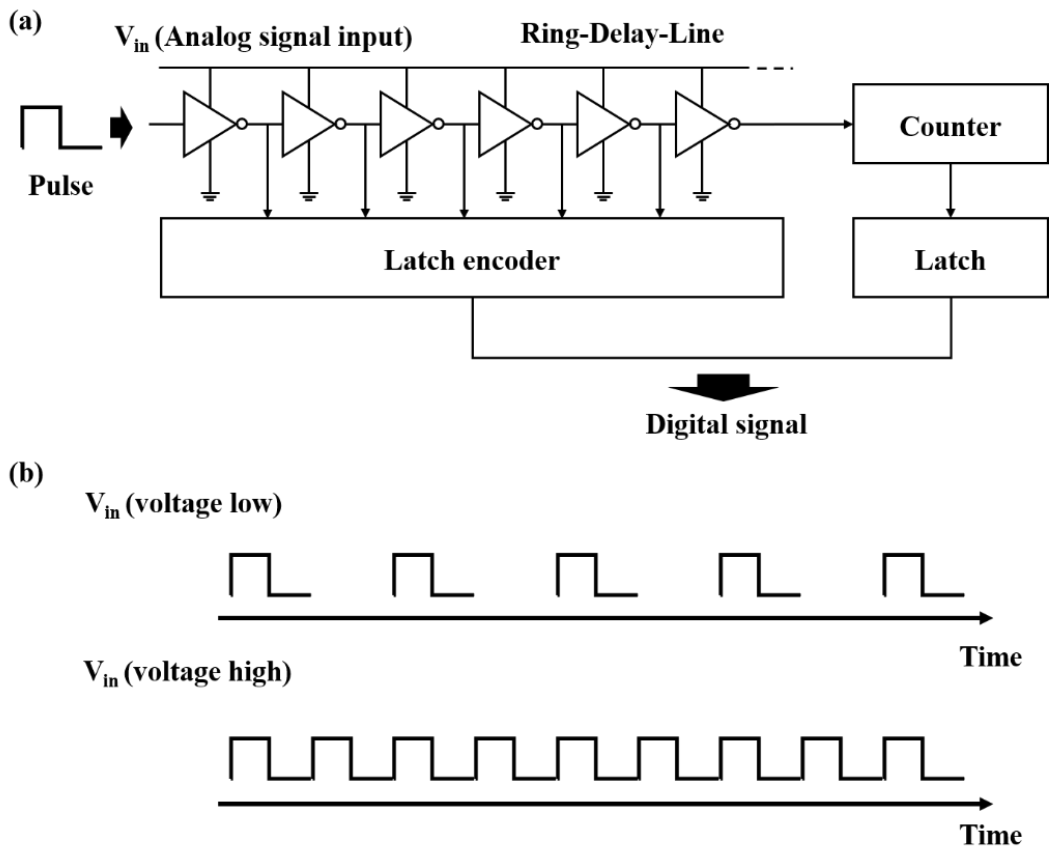


Fig. 2.12(a) Basic structure of the TAD. (b) Schematic of the AD conversion of TAD.

The parameter  $A$  and  $\alpha$  is a constant value depending on the process technology. Thus, the input analog signal can be converted to a pulse looping in the Ring-Delay-

Line. The number of the Delay Unit which the pulse passthrough is depending on the power supply, the result is recorded by counter and encoder as shown in Fig.2.12(a). The pulse recorded by the counter is shown in Fig.2.12(b). [27] [28]

## 2.4 MI sensor system

### 2.4.1 CMOS IC type MI sensor system

The basic stable MI sensor circuit is schematically in Fig.2.13. The pulse current flow through the amorphous wire is generated by a CMOS multi-vibrator. The output voltage of pick-up coil is saved by the sample and hold (S/H) circuit for 20ns. Thus, AC signal from the pick-up coil is converted to a DC signal, and processed by in signal processing circuit. Pulse current is set to 500K Hz with a pulse width of 120ns in the CMOS IC type sensor system, however, the pulse width is also depending on the output waveform of the sensor. To reveal output of the sensor corresponds to rising edge and falling edge, pulse current is set to 1M Hz with a pulse width of 500 ns. The signal processing of the MI sensor circuit is schematically in Fig.2.14. Analog switch (AS) in the sample and hold circuit is controlled by a control signal generated by the CMOS multi-vibrator too. [10] [18]

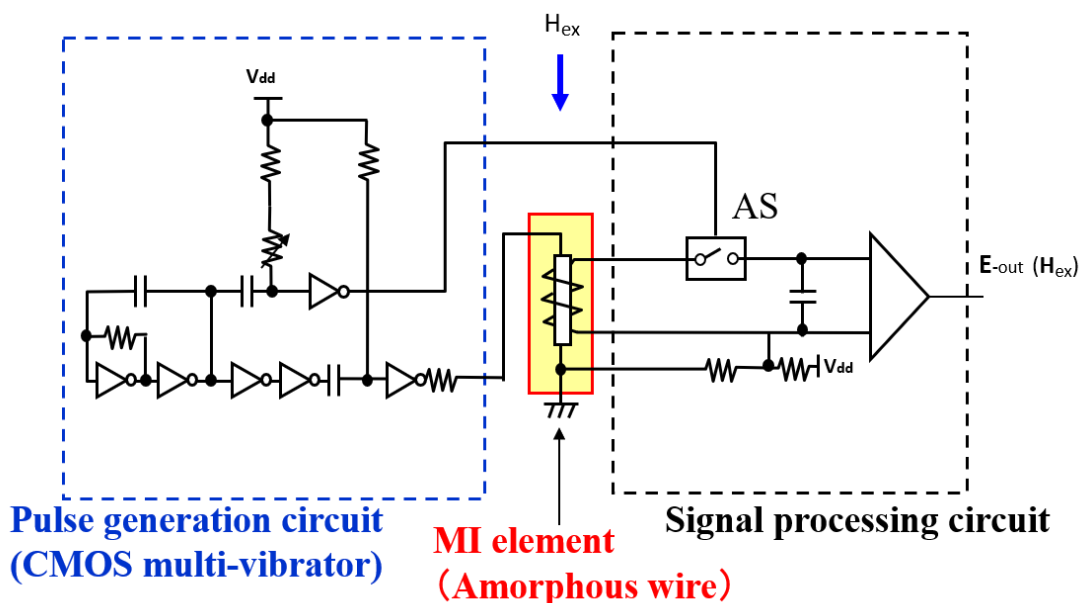
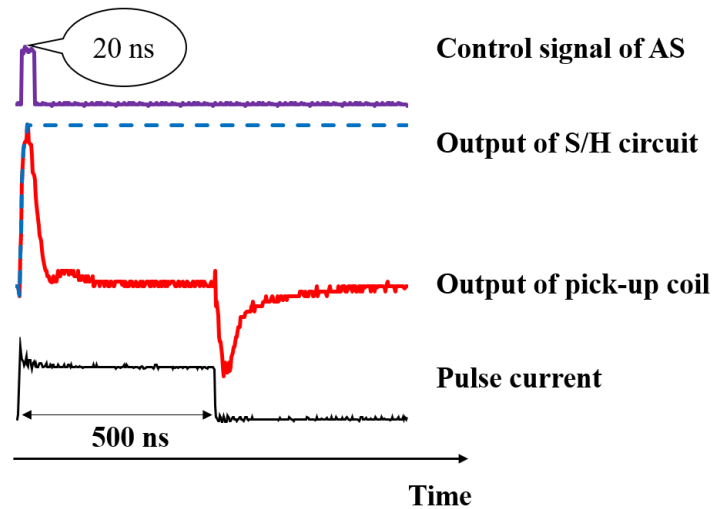


Fig. 2.13 Basic structure of the CMOS IC-type MI sensor circuit.



**Fig. 2.14 Operation of synchronous peak detection (S/H circuit) in the MI sensor system.**

Generally, a sensor system of any sensor consists of a sensor head, sensor circuit, Analog to Digital Converter (ADC). The structure of the MI sensor system used in this research can be considered as:

- 1) Sensor head.
- 2) Sampling circuit to sample the output of the sensor.
- 3) Signal processing circuit.
- 4) The analog output of the sensor circuit is converted to a Digital signal through A/D Converter.
- 5) Data processing.

Generally, S/H circuits and peak detectors are used in AC to DC devices, the peak value of the input signal of peak detectors can be saved in a capacitor automatically as shown in Fig.2.15. The capacitor used in the peak detector is charged through the diode by the input signal, if the circuit detects a higher peak value, it is stored in the capacitor until it is discharged. It sounds like a suitable solution for MI sensors, but considering nonlinear and temperature stability of the diode, it is not an appropriate way to be used in the sensor system.

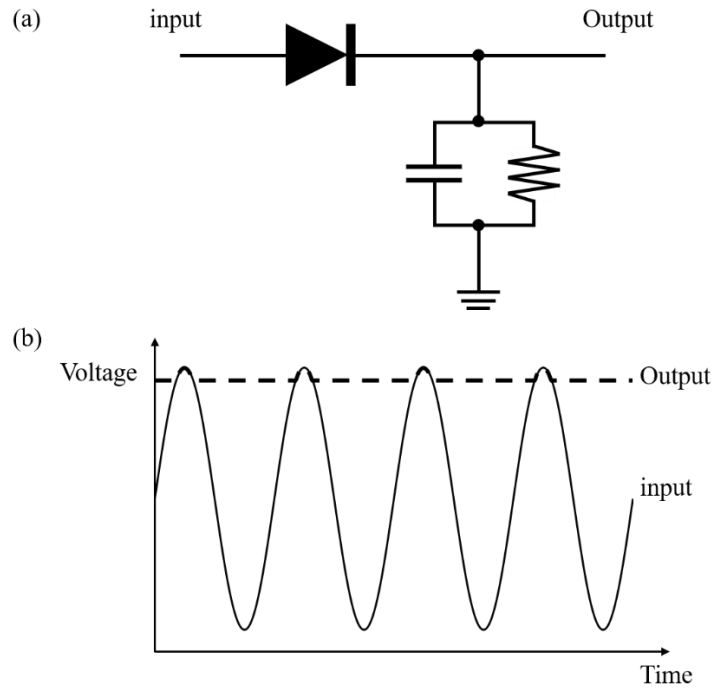


**Fig. 2.15 (a) Basic structure of peak detector. (b) Operation of peak detector.**

## 2.4.2 FPGA type MI sensor system

The pulse generation circuit consists of COMS IC which can be replaced by FPGA. The new sensor system combines with FPGA is schematically in Fig.2.16. Due to the capability of FPGA, the time dependence characteristic of the MI sensor can be investigated easily in the FPGA type system. Depending on the previous research, the sensitivity and the noise level of the FPGA type system are equal to the CMOS IC type MI sensor system, thus, the CMOS multi-vibrator can be replaced by FPGA.

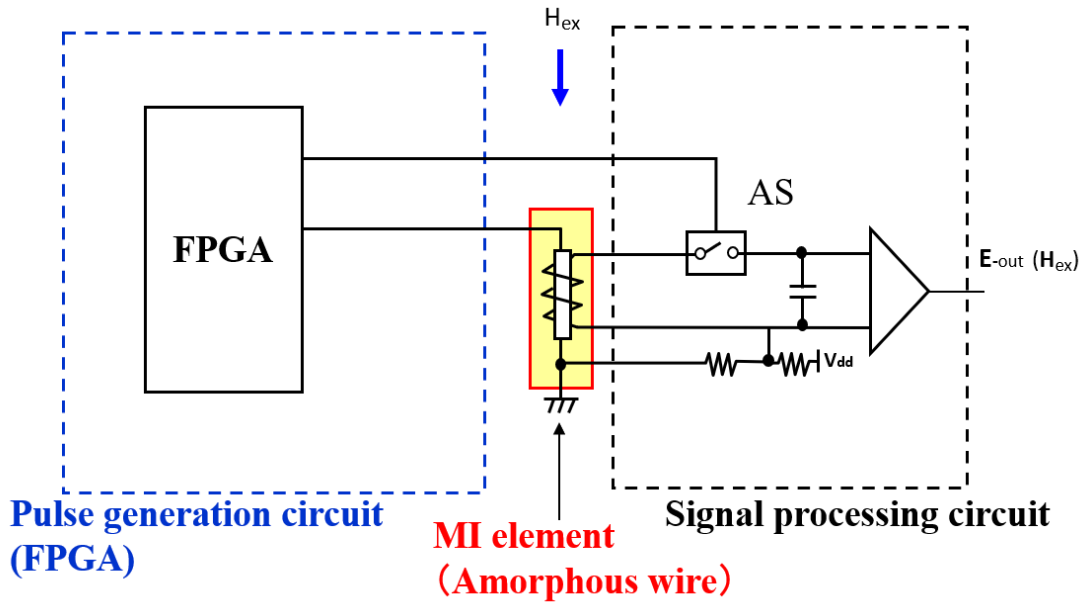


Fig. 2.16 Structure of a FPGA type MI sensor system.

### 2.4.3 TAD type MI sensor system

The MI sensor system include an ADC is depicted in Fig.2.17. It takes time (acquisition time) for the ADC to acquire and convert an analog signal to a digital value. Compare to the ADC based on the comparator, the TAD converts an analog signal to a digital value continuously. Thus, the entire TAD can be considered as an integrator. The TAD can be used as the ADC based on the comparator, [29] or the TAD type MI sensor system can be set up as Fig.2.18. [30] Output of sensor converted by the TAD directly. The input signal to swing between the maximum and the minimum ( $V_{th}$ ) of the operating voltage, thus, the input signal input into TAD with an appropriate biased voltage.

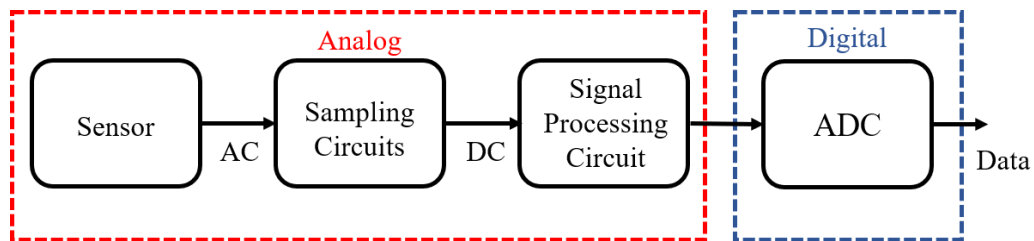


Fig. 2.17 Structure of MI sensor system with conventional ADC.

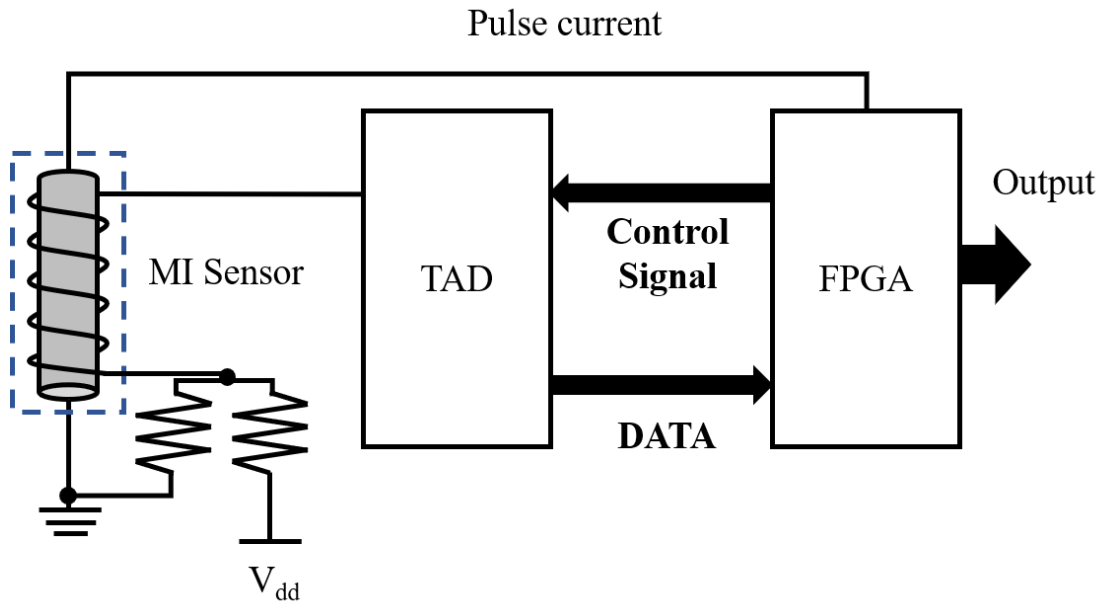


Fig. 2.18 Structure of TAD type MI sensor system.

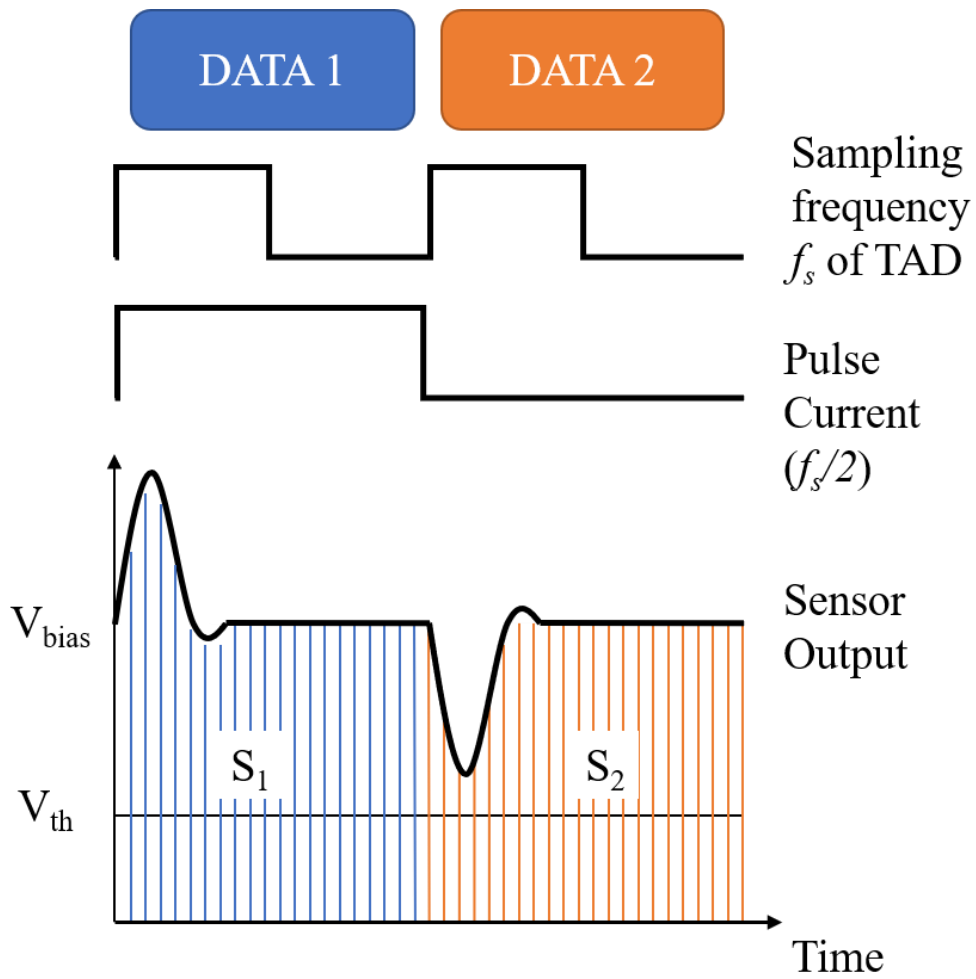


Fig. 2.19 Principle of the TAD type MI sensor system.

Due to the integrating function of TAD, output of the pick-up coil is converted to a digital value in TAD, an AC voltage input signal can be considered as a DC voltage equal to an average DC voltage value. Output of pick-up coil corresponds to rising and falling edge of pulse current has an opposite response to the external magnetic field. So as to maximum the output of the entire sensor system, TAD converts two output separately. Frequency of the pulse current is related to operating frequency of TAD, conversion of output of MI sensor corresponds to the rising and falling edge of pulse current can be expressed as  $S_1$  and  $S_2$ . The output of the sensor can be obtained by taking the difference between the  $DATA1$  and  $DATA2$  by using the FPGA, we obtain  $S_1 - S_2$ . The calculation of the TAD type MI sensor system is depicted in Fig.2.19. Due to this simple structure, the TAD type MI sensor system shows great potential in integration.

The resolution of TAD based MI sensor system is related to the performance of the sensor head and the resolution of TAD. [29] The output  $DATA$  of TAD  $DT$  with input voltage can be expressed as:

$$DT = (1/f_s)[(V_{in} - V_{th})^\alpha / AV_{in}] \quad (2.40)$$

Sampling frequency	Resolution
1M Hz	244 $\mu$ V/LSB
500K Hz	122 $\mu$ V/LSB
100K Hz	24.4 $\mu$ V/LSB
10K Hz	2.44 $\mu$ V/LSB

**Tab.1 The influence of the sampling frequency of the TAD (180nm) on the resolution.**

Thus, the resolution of TAD type MI sensor system with the same sensor head is depending on the sampling frequency  $f_s$  of TAD and the parameter  $A$  and  $\alpha$  (constant value of TAD depending on the process technology), it means we can enhance

resolution of MI sensor system by reducing sampling frequency of TAD (the frequency of the pulse current  $f_s/2$  reduced too) or using a better design rule. The performance of TAD used in this research with different sample frequency is shown in Tab.1. The performance of TAD related to the design rule is shown in Fig.2.20.

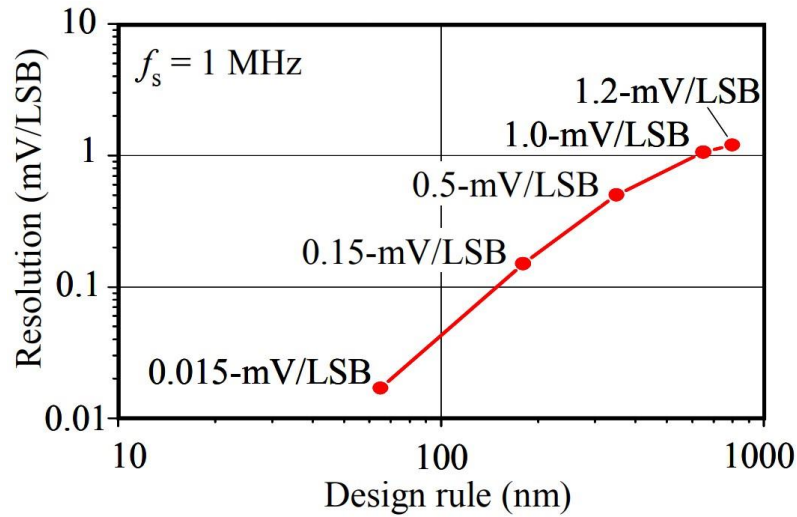


**Fig. 2.20** The influence of the design rule of the TAD on the resolution. [26] [27] [28]

## 2.4.4 Improved TAD type MI sensor system

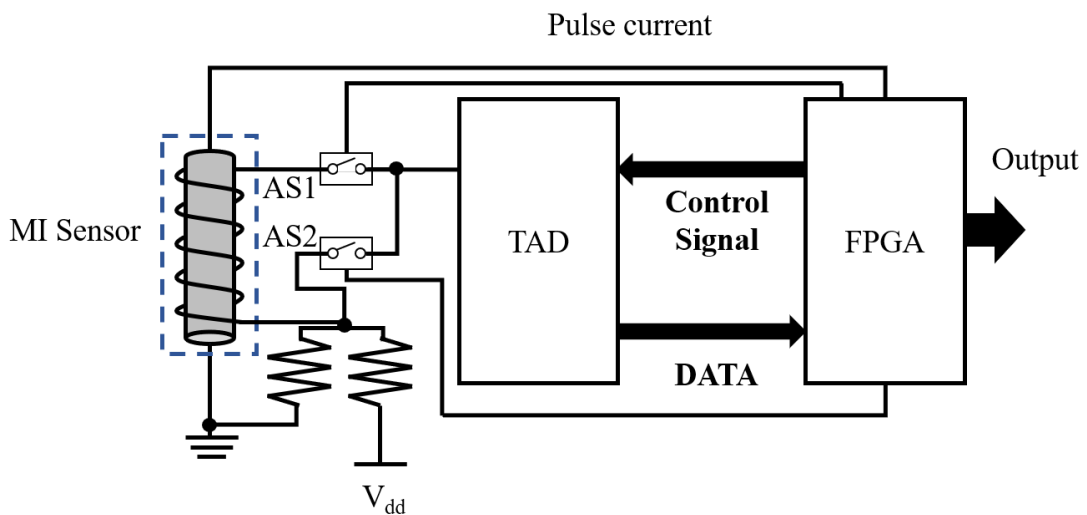


**Fig. 2.21** Basic circuit of the improved TAD type MI sensor system.

Resolution of TAD type MI sensor system is enhanced by combining the TAD with an FPGA controlled sensor circuit. Output of MI sensor corresponds to rising and

falling edge of pulse current is separated by an FPGA controlled AS as shown in Fig.2.21.

The output of TAD is calculated by FPGA to get the output of the sensor. The TAD is controlled by FPGA via a sampling clock, the output of TAD transmitted to FPGA through parallel communication. The illustration of the system is depicted in Fig.2.22.

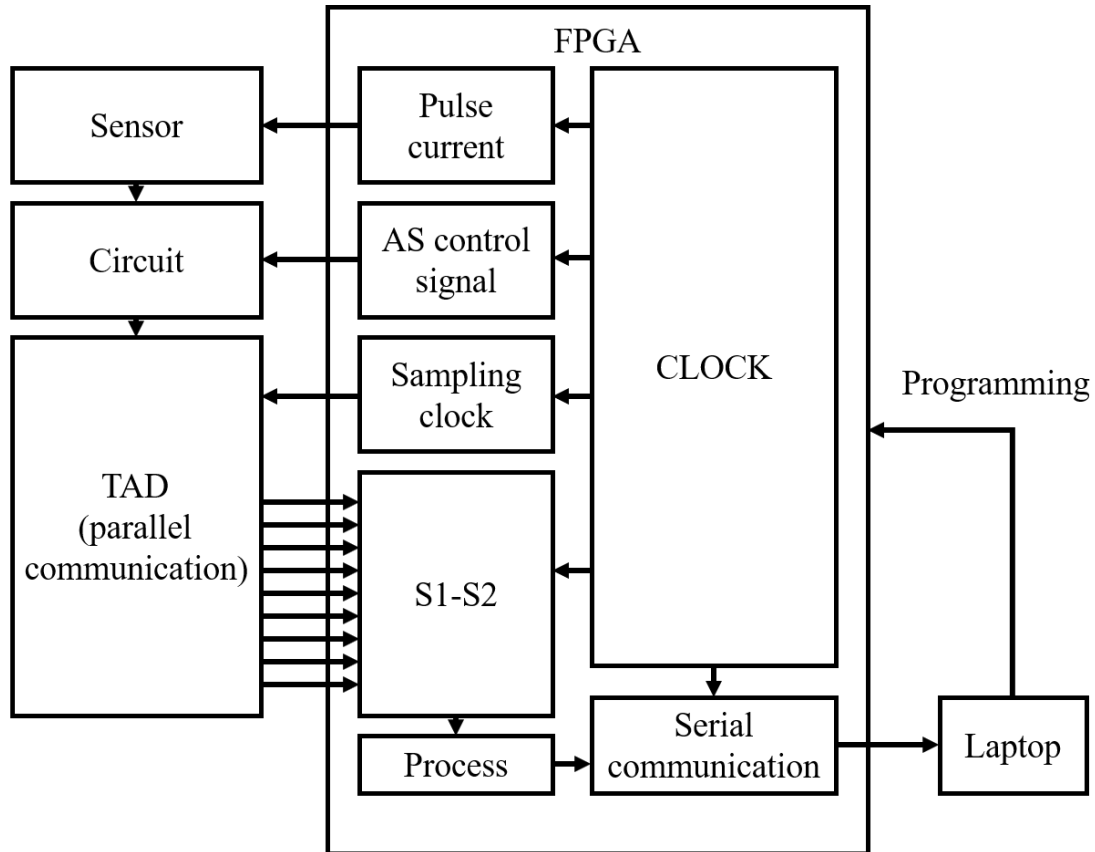


**Fig. 2.22 Illustration of the improved TAD type MI sensor system.**

Therefore, sampling frequency of TAD can be reduced to increase the resolution of TAD type MI sensor system. The output of TAD can be considered as an average result in several sensor periods as shown in Fig.2.23. For example, so as to maintain sampling frequency of entire system at 1K Hz, the sampling frequency of TAD is set to be 2K Hz, the frequency of the pulse current is set to 1M Hz.

The resolution of the TAD type MI sensor system improved through this method (by reducing the sampling frequency of TAD). But there is a limitation to reducing the sampling frequency because of the response speed of the system. Thus, so as to enhance

resolution of TAD type system, a high-resolution TAD with a better design rule is needed.

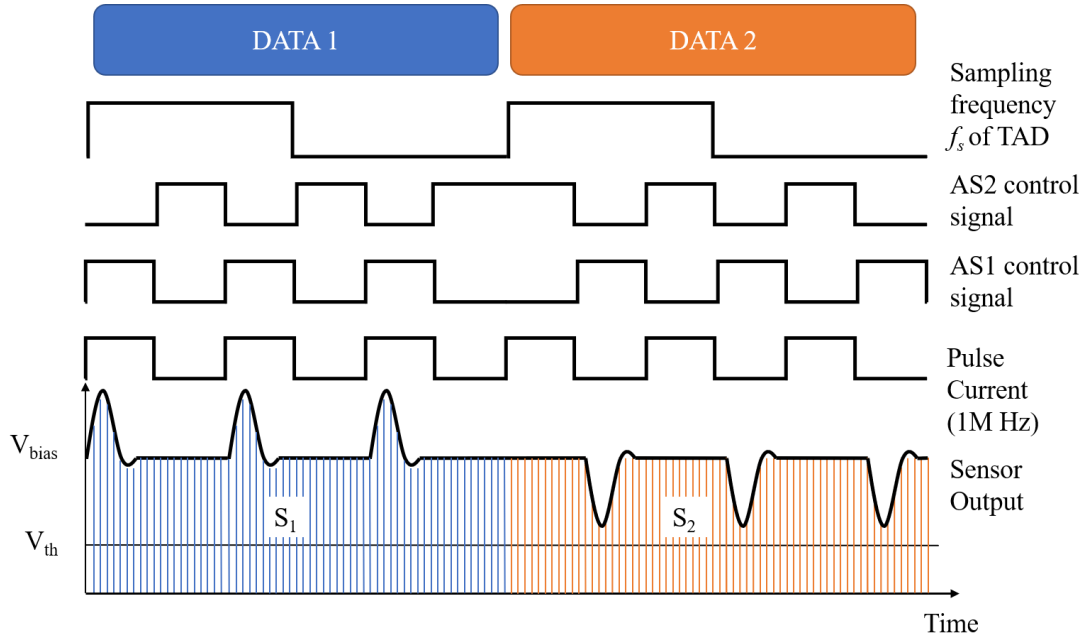


**Fig. 2.23 Operation of the improved TAD type MI sensor system.**

The delay timing of AS in S/H type system needs to be optimized. In TAD type MI sensor system, the output of the sensor is converted by TAD directly, thus, compatibility of system is improved. In other words, the waveform of the output of the sensor depending on the type of sensor. It is more convenient to use entire waveform of sensor output instead of the peak sampling.

## 2.5 Discussion

The frequency and duty ratio of the pulse current generated by the FPGA type MI sensor system can be easily adjusted via the program. The relation between the sensitivity of the sensor and the operation of the analog switch in the S/H circuit has been investigated, as shown in Fig.2.24. So as to maximize performance of the CMOS IC type system, delay time of analog switch needs to be optimized. On the other hand, the output of pick-up coil is saved by S/H circuit during peak value, the output of different types of MI sensors has a different waveform, as shown in Fig.2.25. Different types of MI sensors lead to a different delay time of the S/H circuit. A stable MI sensor

system is developed already, once the CMOS IC type sensor circuit is designed, it is hard to change the delay time of AS. Therefore, depending on the type of MI sensor we use, there is a requirement to redesign MI sensor circuit in mass production. This issue can be solved by using the FPGA type MI sensor system, even so, a standard magnetic field, and an oscilloscope needs to be used to optimize the delay time. In other words, the FPGA type MI sensor is more suitable for laboratory manipulation rather than for a real sensor prototype.

### Switch delay time

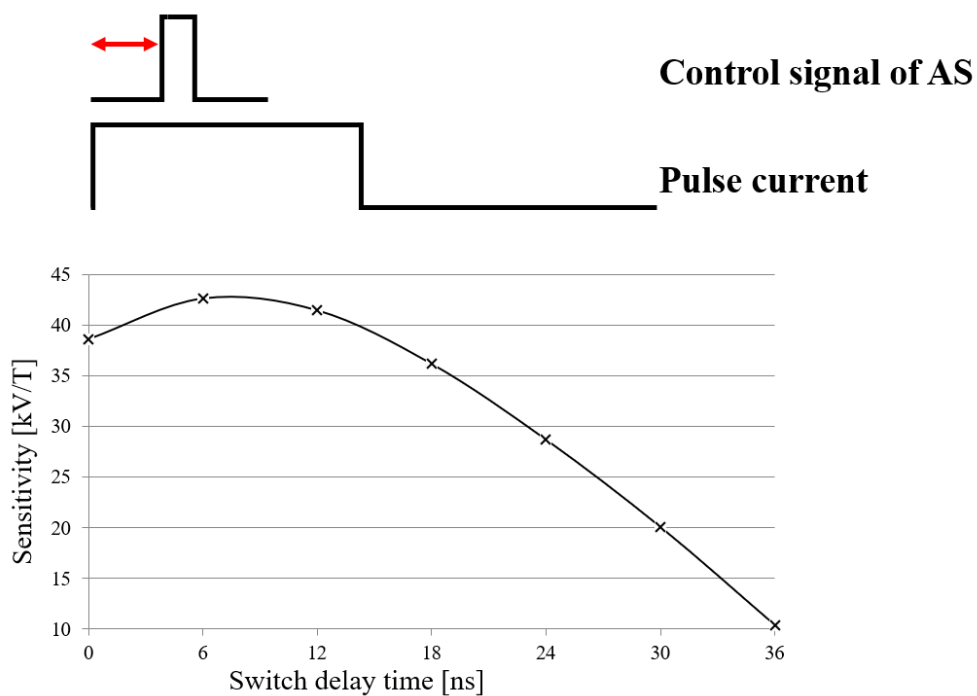


**Fig. 2.24. The influence of the switch delay time of the S/H circuit on the magnetic field to output voltage characteristic.**

The TAD type MI sensor system seems to be an appropriate option, but the operating range of TAD is limited due to its Delay Unit. On the other hand, it is hard to reduce the sampling frequency of TAD to improve the resolution of TAD type MI sensor system, therefore, the only way is improving the design rule of TAD, but the Research and Development (R&D) cost is too high.

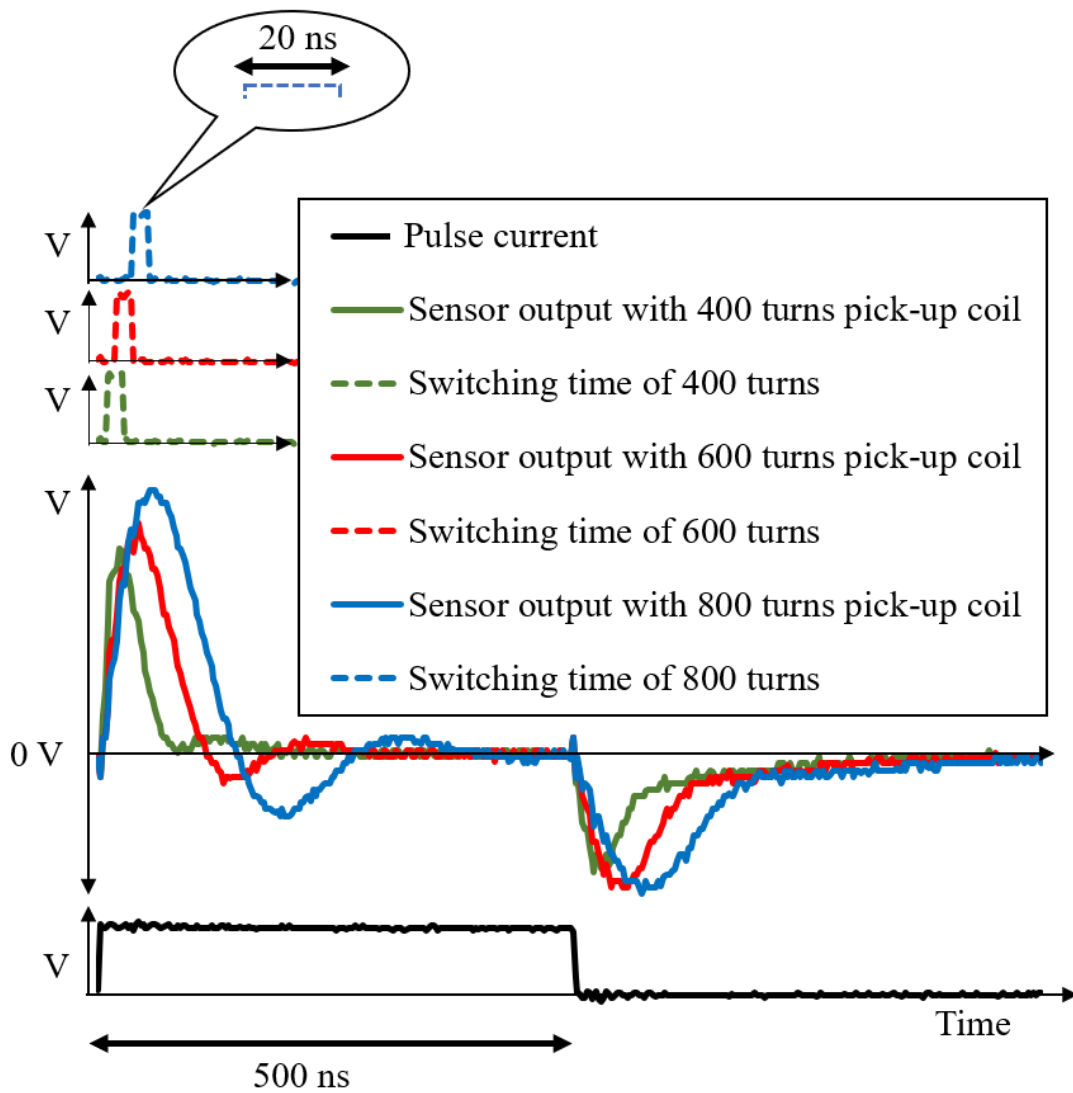


**Fig. 2.25** The influence of turns of pick-up coil on output waveform of MI sensor.

In development of sensor circuit for microsize MI sensor use, the amorphous wire driven by a GHz pulse current leads to a sharp pulse output in pick-up coil. [31] It is hard to detect peak value of this sharp pulse output. On the other hand, the operation of the capacitor in the S/H circuit can be expressed as:

$$V(t) = \frac{1}{C} \int_{t_0}^t I(t) dt + V(t_0) \quad (2.41)$$

The output of the S/H circuit is shown in Fig.2.26.

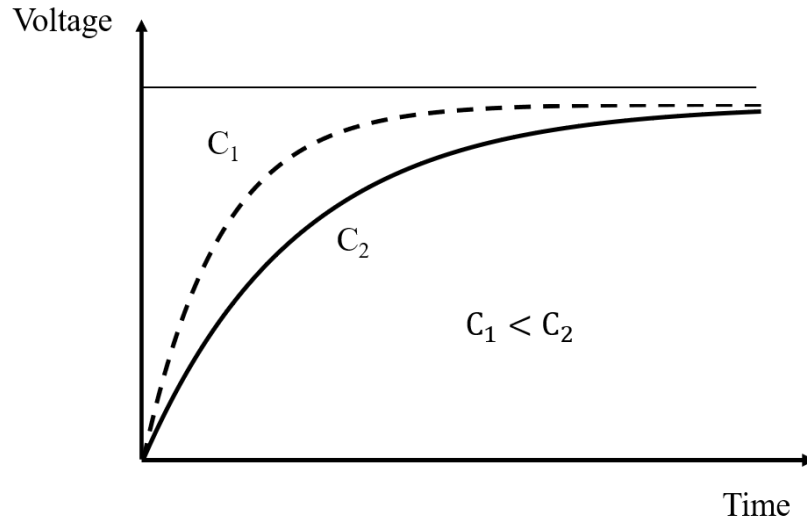


**Fig. 2.26 The influence of the capacitance of the capacitor on the charging rate.**

In order to sample the output of the sensor in a short time, capacitance  $C$  of the capacitor needs to be very small. The thermal noise of the capacitor can be expressed as:

$$V_n = \sqrt{\frac{k_B T}{C}} \quad (2.42)$$

Thus, the thermal noise of the capacitor increased in the microsize MI sensor system.

## 2.6 Summary

The CMOS IC type (S/H method) MI sensor system is an excellent design, high resolution, high response speed, low cost, but there are three limitations:

- 1) High thermal noise in the high-speed response system.
- 2) The sensitivity of the MI sensor is affected by the sampling timing of the S/H circuit.
- 3) Sampling timing of the S/H circuit of MI sensor depending on the type of MI sensor.

The FPGA type MI sensor system can be compatible with different types of sensors via the program. Even so, the FPGA type MI sensor is more suitable for laboratory manipulation rather than for a real sensor prototype.

The TAD type MI sensor system show high compatibility with the different type of sensor due to its sampling method, but it hard to achieve high resolution and high

response speed at the same time.

The Micro-Electro Mechanical System (MEMS) and the integrated circuit are widely used in sensor technology. In order to develop a high-performance microsensor system, the new MI sensor system should be easy to integrate. There are some limitations of the previous types of sensor systems for a real sensor prototype.

The purpose of this research is to develop high-compatibility and high-resolution MI sensor system which can be easily integrated, which means the advantage of the TAD type system and the advantage of the S/H type system need to be combined. A novel approach to sample the output of the MI sensor which has the same function as TAD is proposed in this research. The S/H circuit in the conventional system need to be replaced.

# Chapter 3 Design and method

## 3.1 Beginning

It is more convenient to study MI sensor system via FPGA depending on previous research, therefore, in this study, an FPGA is used in the development of the sensor prototype. Generally, a sensor system must be embedded with an ADC. Thus, there is a logical circuit in the sensor system. The FPGA used in this research can be considered as a logical circuit that the function of the logical circuit can be reconfigured via the program. The development of the digital part (FPGA) of this paper and experimental procedures will be discussed in this chapter.

A hybrid analog/digital circuit is used in this research. The FPGA type MI sensor system is depicted in Fig.3.1. The entire measurement system is shown in Fig.3.2. The function of FPGA is defined through programming language Verilog HDL (Verilog Hardware Description Language). Output of sensor system is transmitted to laptop. The entire system is set in a double layer Permalloy magnetic shielding box. A Helmholtz coil is used to generate applied magnetic field. The Helmholtz coil consists of two parallel circular magnetic coils with a common axis. The distance between two circular magnetic coils equal to the radius of the coil. A uniform magnetic field is generated between two circular magnetic coils. The sensor head is set in the Helmholtz coil as depicted in Fig.3.3.

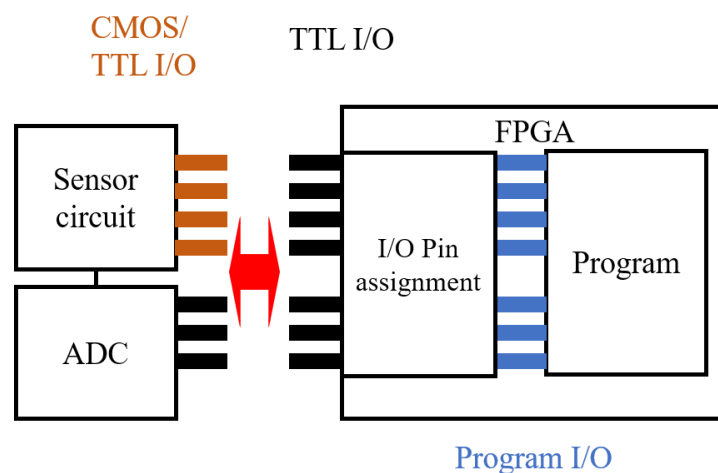


**Fig. 3.1 Illustration of FPGA type MI sensor system.**

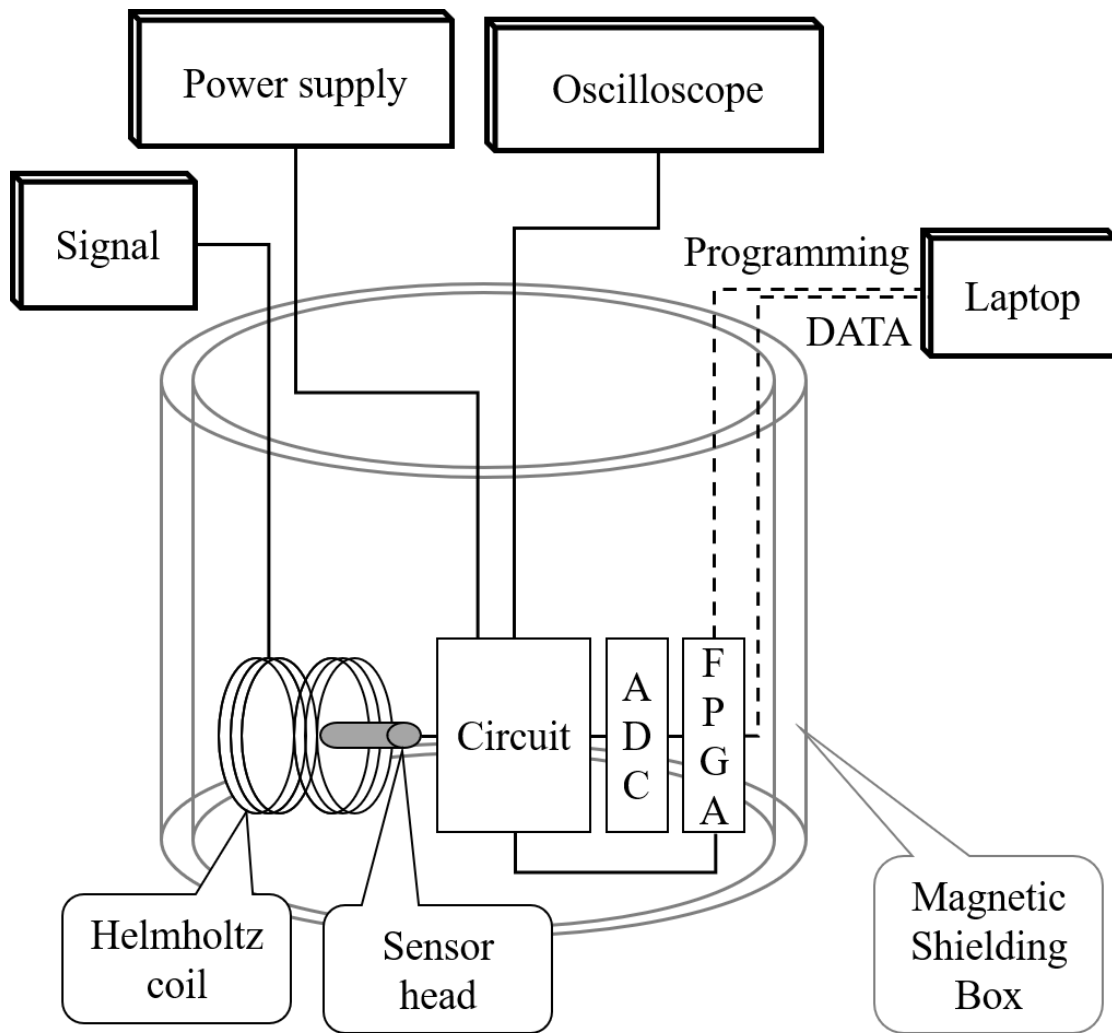


**Fig. 3.2 Schematic diagram of the experimental system.**

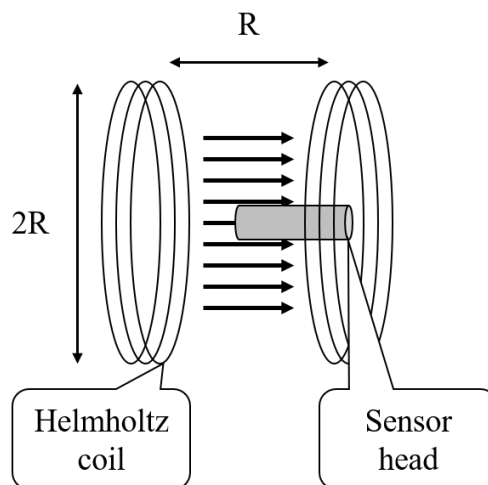


**Fig. 3.3 Structure of Helmholtz coil.**

### 3.2 Op-amp integrator

The integrator is an important electronic device that can be used in the integration of an electric current, it is widely used in engineering and scientific research. In the development of the circuit of the magnetic sensor, the integrator is already used in the hall effect sensor, the Fluxgate sensor, and the SQUID. [32] [33] [34] We consider applying this device in our research to replace the S/H circuit to acquire the entire output waveform of pick-up coil.

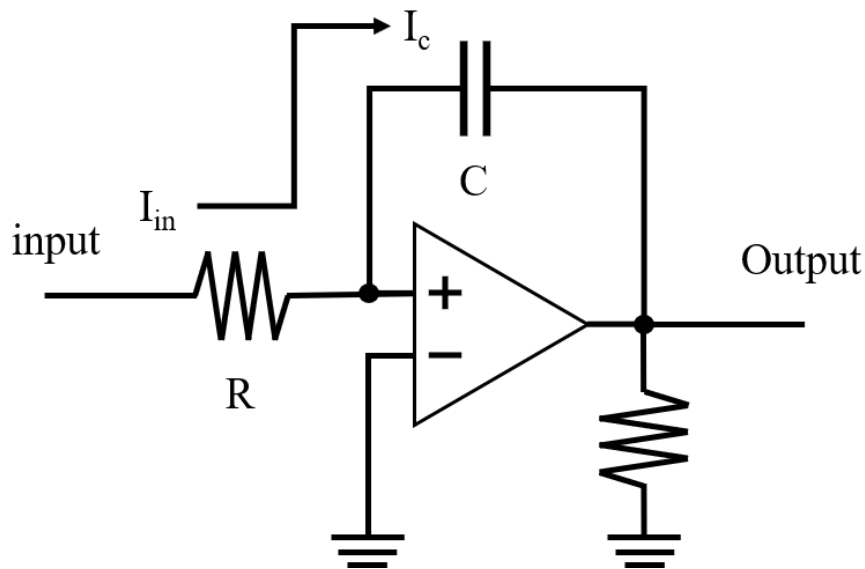


**Fig. 3.4 Op-amp integrator ideal model.**

Generally, integrator usually constructed using an Op-amp (operational amplifier) integrator and ideal circuit is shown in Fig.3.4. The voltage of nodes + and - are equal in the ideal model and node - is considered to be a virtual ground. The current flow through the resistor is expressed as:

$$I_{in} = \frac{V_{in}}{R} \quad (3.1)$$

Due to Kirchoff's current law, so:

$$I_{in} = I_c \quad (3.2)$$

The capacitor is charges or discharges by the current as:

$$\frac{I_c dt}{C} = dv_{out} \quad (3.3)$$

The mathematical operation of integration during the time t can be expressed as:

$$\int_0^t \frac{V_{in}}{R} dt = - \int_0^t C \frac{dv_{out}}{dt} dt \quad (3.4)$$

Thus, result of Op-amp integrator governed by equation:

$$V_{out} = - \frac{1}{RC} \int_0^t V_{in} dt \quad (3.5)$$

### 3.3 Analog-to-Digital Converter (ADC)

The output of the MI sensor is sampled by an integrator and processed in the signal processing section. A conventional 32 bit ADC (LTC2500-32) is used in this research to convert the output of MI sensor circuit, as depicted in Fig.3.5. ADC is governed by the input signal from FPGA. The sampling frequency, acquisition timing, downsampling factor, and the function of the digital filter can be controlled via FPGA, therefore, the ADC used in this research is programmable.

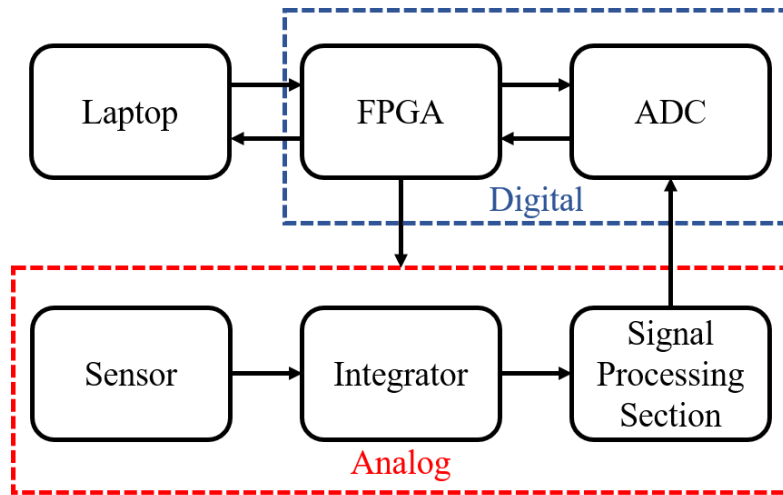


**Fig. 3.5 Structure of the proposed MI sensor system.**

A Successive Approximation Register (SAR) ADC used in this research as shown in Fig.3.6. The analog input is compared to the reference voltage step by step, start with  $V_{ref}/2$ , end with  $V_{ref}/2^n$ . The results of the comparator show 1 / 0 means higher or lower than the reference voltage. The binary weights are assigned to each bit from the MSB (Most Significant Bit =  $V_{ref}/2$ ) to LSB (Least Significant Bit =  $V_{ref}/2^n$ ). After all the reference voltage has been compared to the input, the result of a binary number

representing the analog input. The conversion finished at the end of the comparison as shown in Fig.3.7. It can be controlled via FPGA that the output voltage of the sensor is locked at a constant level during the acquisition time of ADC.

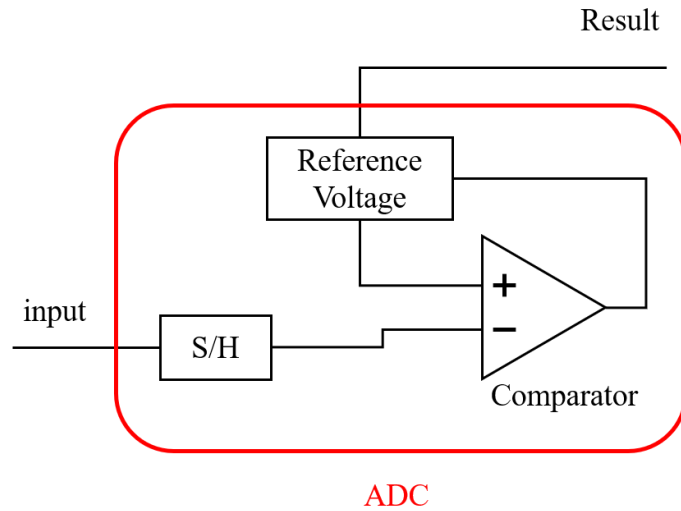


**Fig. 3.6 Schematic diagram of the SAR ADC.**

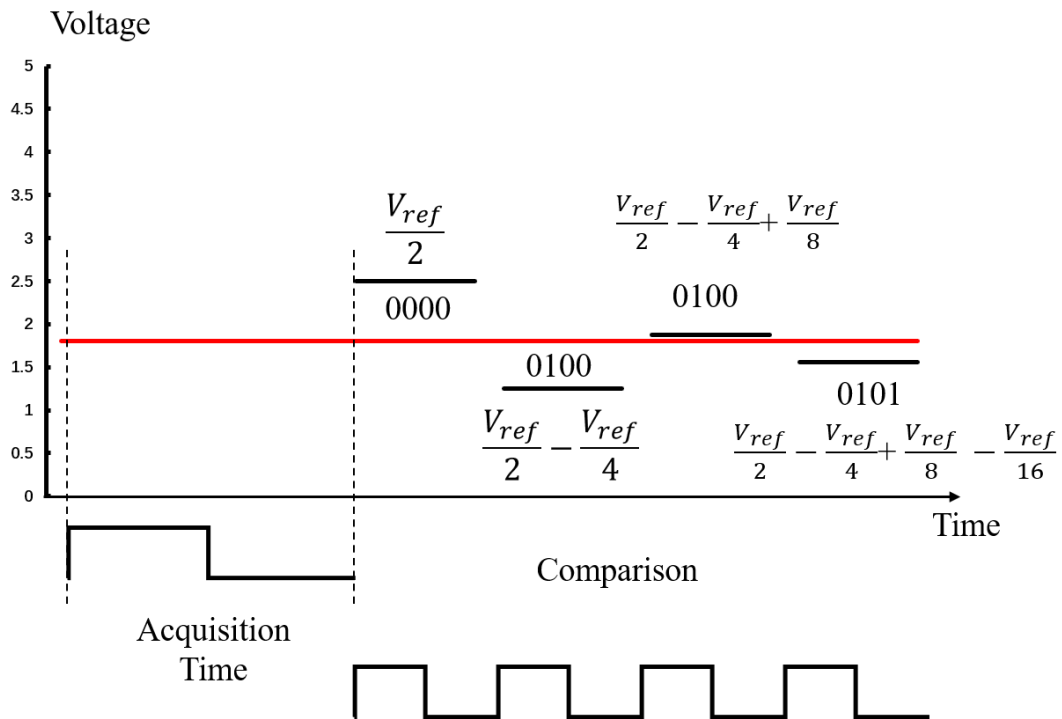


**Fig. 3.7 Schematic of the AD conversion of SAR ADC.**

### 3.4 System architecture

The capacitor in the Op-amp integrator must be reset after every sample period,

before the capacitor is reset, the result of the Op-amp integrator can be saved in an S/H circuit of the signal processing section or sampled by the ADC directly. On the other hand, the output voltage from the MI sensor circuit must be sampled by ADC during the acquisition time, therefore, the entire system must be driven with an accurate time source. The block diagram of proposed system is schematically depicted in Fig.3.8.

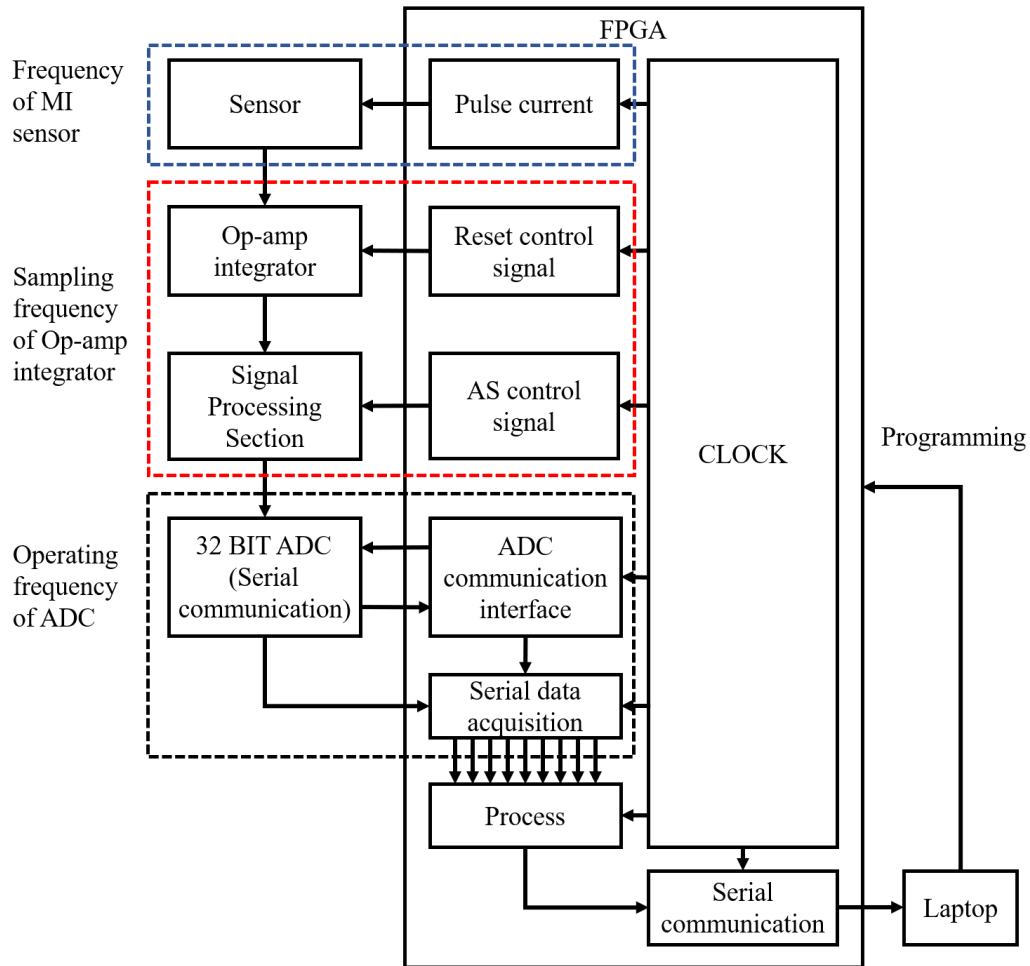


**Fig. 3.8 Block diagram of proposed system.**

The ADC used in the proposed system communicates with FPGA via serial communication as shown in Fig.3.9. The data transmitted step by step in the serial communication, and at the same time in parallel communication. Thus, the data from ADC must be converted first. In the conventional MI sensor system, the signal processing section consists of an amplifying section and a bandpass filter. In the proposed system, the function of the bandpass filter can be achieved by using a digital

filter. Output of proposed system transmitted to laptop via serial communication.

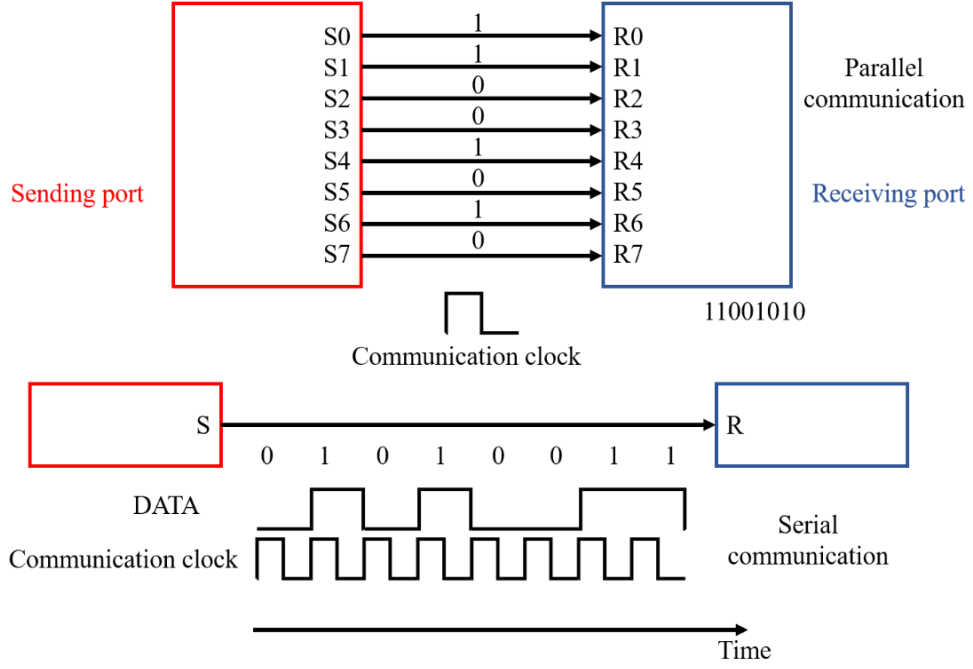


**Fig. 3.9 The communication interface of the proposed system.**

### 3.5 Data analysis

The data received by the laptop is analyzed through Fourier analysis.

The Orthogonal transformation in the inner-product space can be expressed as:

$$\int_T 2 \cos(2\pi mt) \cos(2\pi nt) dt = 0 \quad (3.6)$$

$$\int_T 2 \sin(2\pi mt) \sin(2\pi nt) dt = 0 \quad (3.7)$$

$$\int_T 2 \sin(2\pi mt) \cos(2\pi nt) dt = 0 \quad (3.8)$$

$$\int_T 2 \cos(2\pi mt) \sin(2\pi nt) dt = 0 \quad (3.9)$$

$$\int_T 2 \cos(2\pi nt) \cos(2\pi nt) dt = 1 \quad (3.10)$$

$$\int_T 2 \sin(2\pi nt) \sin(2\pi nt) dt = 1 \quad (3.11)$$

Depending on Euler's formula,  $\sin(2\pi ft)$  and  $\cos(2\pi ft)$  can be expressed as:

$$\sin(2\pi ft) = \frac{e^{i2\pi ft} - e^{-i2\pi ft}}{2i} \quad (3.12)$$

$$\cos(2\pi ft) = \frac{e^{i2\pi ft} + e^{-i2\pi ft}}{2} \quad (3.13)$$

The data from the sensor system is a time-based function  $x(t)$  that can be expressed as a sum of trigonometric functions. Each of trigonometric functions represents a frequency component of  $x(t)$ . Therefore, Fourier transform is given by:

$$F(f) = \int_{-\infty}^{+\infty} x(t) \cdot e^{-i2\pi ft} dt \quad (3.14)$$

$F(f)$  is a frequency-based function that greatly simplifies the analysis of data from the sensor system.

### 3.6 System test

The almost experiment in this research is based on the pico tesla type MI sensor head with a length of 1 cm and a diameter of 30  $\mu m$  provided by UNITIKA LTD. The resolution of the MI sensor system depends on several conditions. The parameters and materials of the sensor head, turns of the pick-up coil, detection method (impedance or off-diagonal), sensor circuit, ADC. The improvement in this research is concentrated on the sensor circuit. So as to determine improvement of proposed system, the characteristic of the proposed system and the conventional system has been tested in the same conditions with the same sensor head, as shown in Fig.3.10.

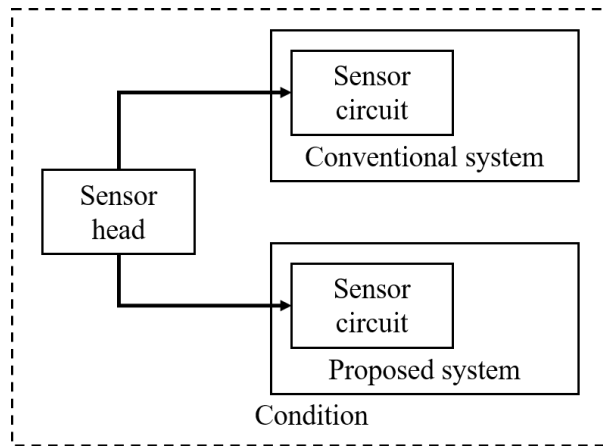


**Fig. 3.10 Experimental setup.**

The resolution can be evaluated via the signal to noise ratio (SNR). For example, 20 dB gain change gives the ratio of 10 for the calculated reference signal and noise floor,

the same relation in the ADC as shown in Appendix II. A higher SNR of the system represents high resolution. In other words, a minimum input magnetic field change produces a standardized output voltage easily.

In the FPGA type MI sensor system with an FPGA controlled ADC, the output of the sensor circuit is refreshed after every operation of the S/H circuit and converted by ADC. Thus, there is a metastable region during every operation of the S/H circuit, as shown in Fig.3.11. In addition to this, the charger saved in the capacitor leaks over time. In order to convert the output of sensor circuit accurately, output of sensor circuit is converted by ADC after every operation of the S/H circuit. The conversion during the metastable region is also investigated, as shown in Fig.3.12. The MI sensor head in the FPGA type conventional system is set in a Helmholtz coil with an applied sinusoidal magnetic field with a frequency of 10 Hz and an amplitude of 300 pT. Both outputs of MI sensor system with the different operations are recorded for 10s to obtain the frequency response from 0.1 to 100 Hz. Operation of the sensor circuit and the ADC is synchronized via FPGA. Compare to the sensor system with random acquisition time, the noise level of the sensor system with a fixed acquisition time improved at the low-frequency (0.1~1 Hz) region.

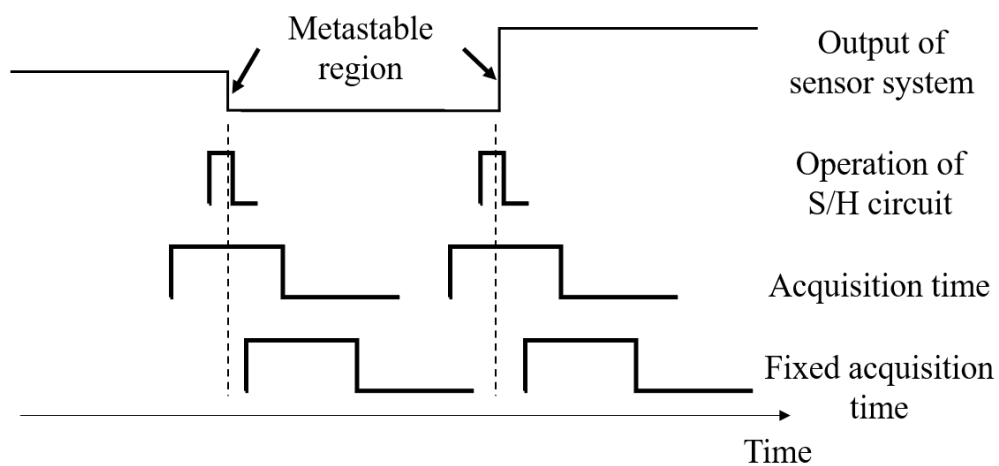


**Fig. 3.11 Operation of the FPGA type MI sensor system with Synchronized AD conversion.**

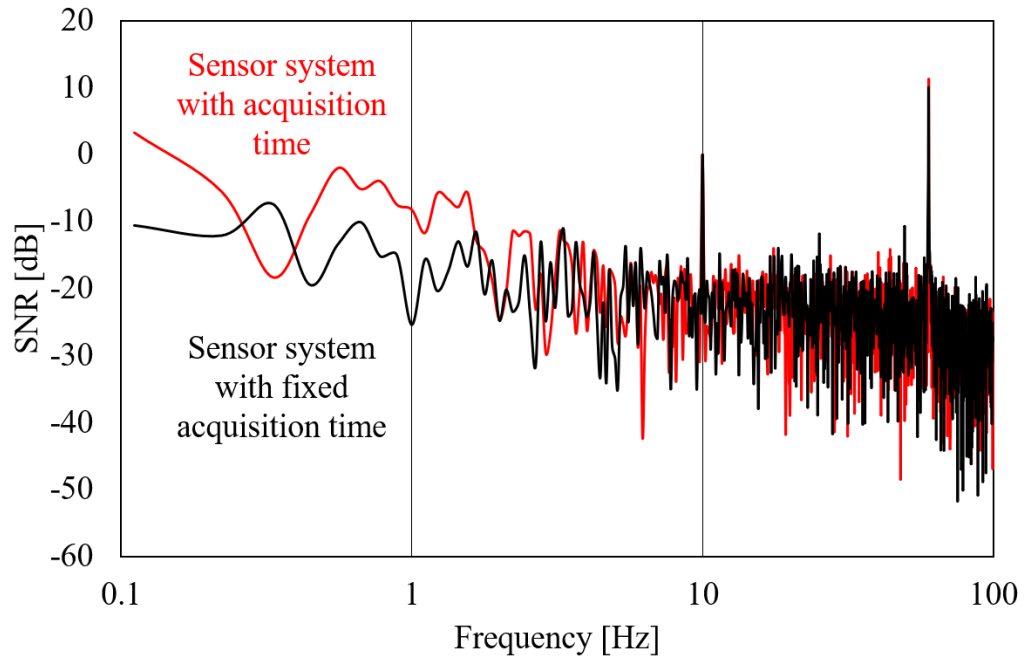


**Fig. 3.12** The SNR of the FPGA type MI sensor system with synchronized AD conversion (black) and asynchronous AD conversion (red).

### 3.7 Summary

MATLAB and Excel are used in this research to analyze the data from the MI sensor system. The program (Verilog HDL) of FPGA in the proposed MI sensor system is completed and tested before the beginning of experiment. In order to test the output of the analog circuit in real-time, an oscilloscope is used to check the waveform of the sensor circuit.

The design and the experimental method of proposed system discussed, influence of the conversion time of ADC has been investigated, and a novel approach to acquire output waveform of MI sensor proposed in this chapter.

# Chapter 4 MI gradiometer

## 4.1 Introduction

The magnetic noise around us is discussed in chapter 1. In order to detect the weak magnetic signal  $B_s$ , the influence of magnetic noise  $B_n$  needs to be reduced. Generally, the magnetic noise can be removed by putting the entire measurement system into a magnetic shielding room. A magnetic gradiometer is a measurement system with a high degree of immunity from the magnetic noise and the spatial resolution improved through this measurement system. Thus, a MI gradiometer is developed in this research.

MI gradiometer is a device to measures the gradient of the magnetic field which can be used in a weak magnetic field detection. The MI gradiometer constructed by a pair of MI sensor heads (Sensing head with sensitivity  $A_1$  and Reference head with sensitivity  $A_2$ ) with a common axis, the distance between two MI sensor heads in this research is 3 cm. The sensitivity of MI sensor head used in the MI gradiometer are equal ( $A_1=A_2$ ) in the ideal model, therefore, the magnetic noise applied to both MI sensor head can be canceled out, the output of the MI gradiometer can be expressed as:

$$B_{out} = B_{sen} - B_{ref} = (B_s + B_n) - B_n = B_s \quad (4.1)$$

Due to the difference in sensitivity and the axis misalignment of two MI sensor head, the magnetic noise cannot be canceled out completely. The effect of the noise suppression of the MI gradiometer is related to the mismatch in sensitivity between  $A_1$  and  $A_2$  as:

$$A_1(B_s + B_n) - A_2B_n = A_1B_s + (A_1 - A_2)B_n \quad (4.2)$$

## 4.2 Development

The development of the proposed MI gradiometer is based on the Op-amp integrator. The output of pick-up coil buffered by an Op-amp and transmitted to signal rectifier section, the output of the sensor corresponds to rising and falling edge of the pulse current is separated into two signals by an AS controlled by FPGA. In order to sample two signals from the signal rectifier section, the bias voltage of the output of the sensor

in the conventional system must be removed. The two signals acquired by Op-amp integrator separately, operation mode of Op-amp integrator is shown in Fig.4.1.

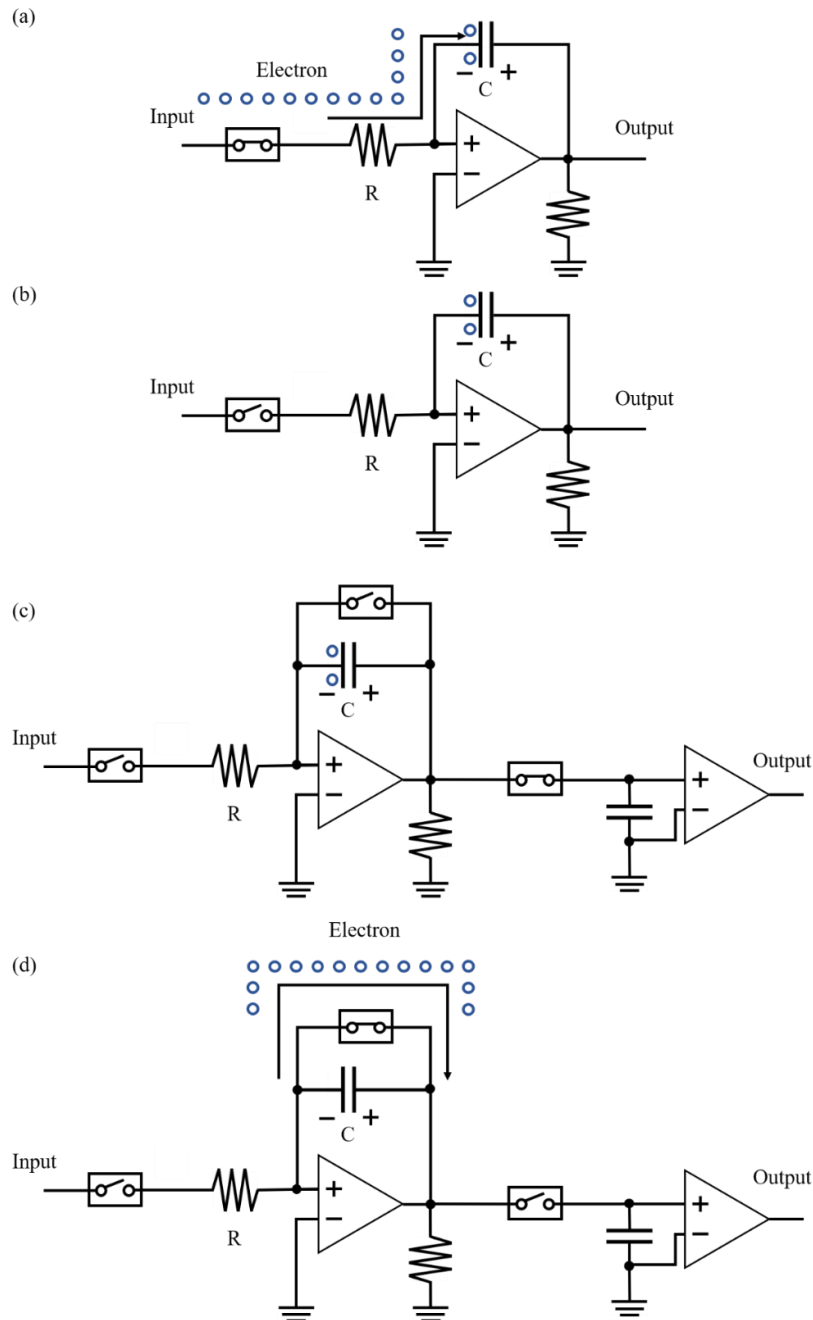


**Fig. 4.1 Operation mode of integrator in proposed system. (a) Sampling. (b) Holding. (c) Output. (d) Op-amp integrator reset.**

The electron saved in one side of the capacitor while the analog switch turns on, an opposite voltage appears on the other side of the capacitor. If the input node of integrator switch to the bias node (Ground) for half of the sensor period, the capacitor discharged

through the ground. Therefore, input node of integrator isolated by an analog switch to maintain the electron in the capacitor as depicted in Fig.4.1(b).

So as to refresh capacitor to load output of sensor during the next period of the sensor, the voltage saved in the capacitor must be reset, as depicted in Fig.4.1(d). Output of integrator changes while the analog switch turns on, and locked at a constant level while the analog switch turns off. Before the capacitor reset, the result of integrator loaded by the S/H circuit in ADC or the signal processing section while it's locked up, as shown in Fig.4.1(c).

In the conventional MI gradiometer system, the output saved in the S/H circuit. Output of the MI gradiometer is obtained by taking the difference between the output of two MI sensor. Both outputs of the MI sensor correspond to the rising and falling edge are sampled in the proposed system, therefore, there is four output of the sensor obtained in the proposed system. The output of the MI sensor corresponds to falling edge can be considered as a shifted signal of rising edge, depending on the previous research, [24] the output signal  $V_r$  and  $V_f$  is proportional to applied field but inverted to each other as:

$$V_r = A_r \times B \quad (4.3)$$

$$V_f = A_f \times B \quad (4.4)$$

The phase difference between  $V_r$  and  $V_f$  is equal to half of the sensor period. The proposed MI gradiometer is obtained by taking the difference between the output of two MI sensors both the rising and falling edge separately. Thus, a differential pair of signals obtained as:

$$V_1 = A_{r1}(B_s + B_n) - A_{r2}B_n = A_{r1}B_s + (A_{r1} - A_{r2})B_n \quad (4.5)$$

$$V_2 = A_{f1}(B_s + B_n) - A_{f2}B_n = A_{f1}B_s + (A_{f1} - A_{f2})B_n \quad (4.6)$$

### 4.3 Sensor circuit

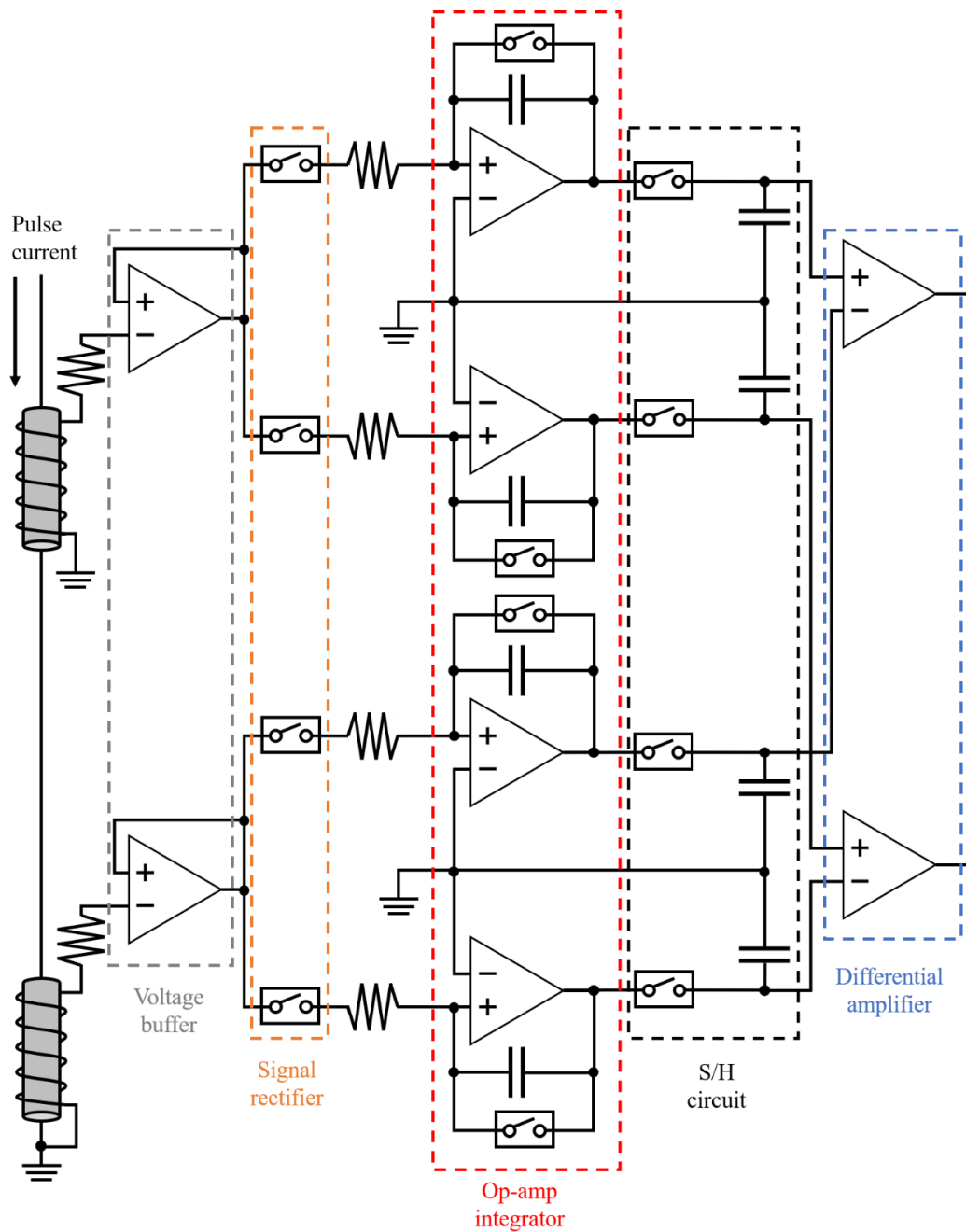


**Fig. 4.2 Basic sensor circuit of the proposed gradiometer.**

Output of MI sensor biased by a positive voltage in the conventional system, thus, the signals sampling section is powered by a single power (5V). Output of MI sensor and output voltage of integrator in the proposed system swing around the ground (0V), thus, the analog switch (ADG413) and the Op-amp (ADA4627) used in the signals sampling section is powered by a dual power supply. The analog switch used in this research controlled by FPGA via Transistor-Transistor Logic (TTL)/CMOS interface.

The output of the MI gradiometer amplified via a differential amplifier. The signal processing section is powered by a dual power supply (+15V and -15V). The proposed MI gradiometer is schematically depicted in Fig.4.2.

The entire analog circuit governed by the FPGA, thus, the operation of the sensor circuit can be controlled via the program, it is easier to synchronize the sensor circuit with an FPGA controlled ADC.

### 4.4 Timing chart

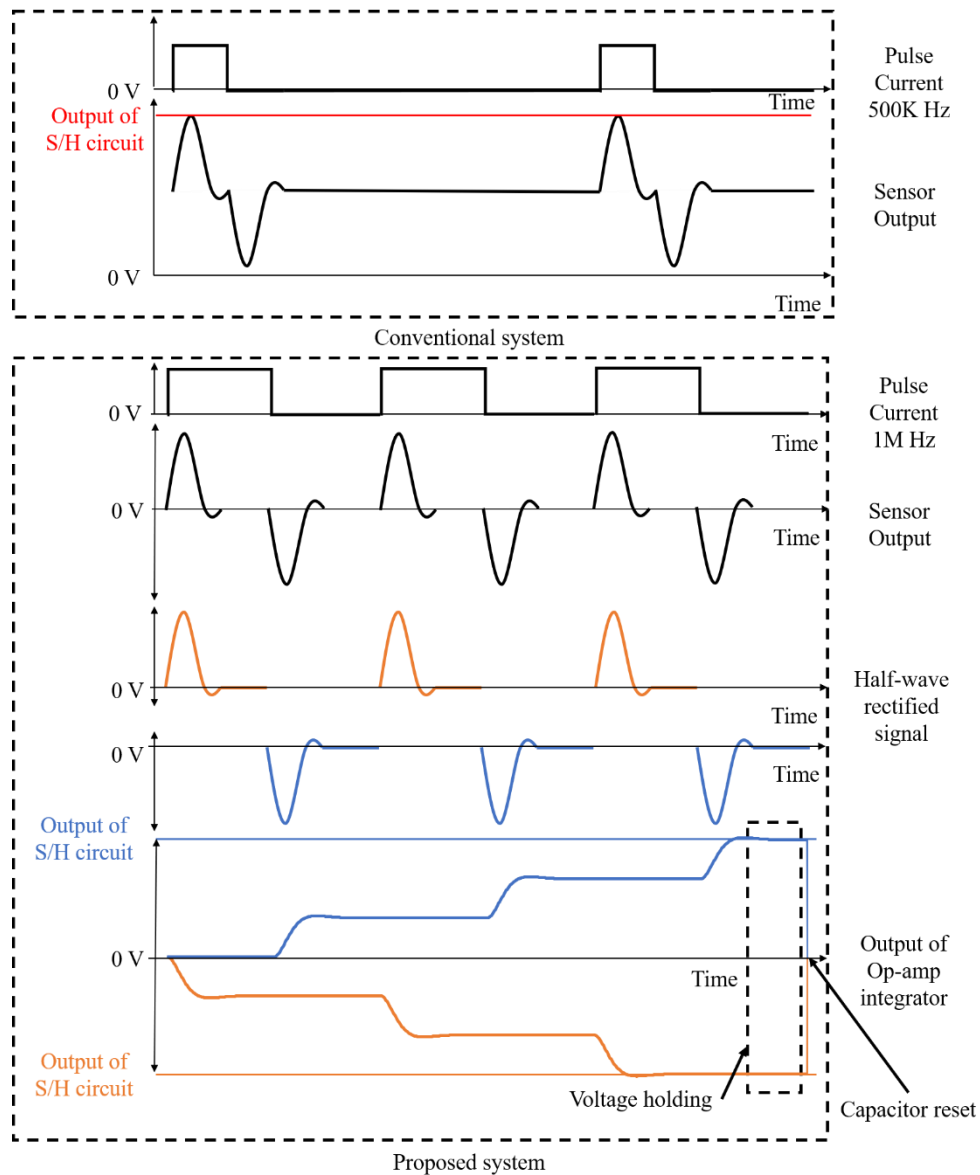


**Fig. 4.3 The timing chart of the proposed system we designed.**

The MI sensor is driven by a pulse current with a frequency of 500K Hz and a pulse

width of 120 ns in the conventional MI gradiometer. In the proposed system, the MI sensor is driven by the pulse current with a frequency of 1M Hz and a pulse width of 500 ns (duty cycle = 50%). The FPGA is driven by a clock with a frequency of 50M Hz and a pulse width of 10 ns (duty cycle=50%), thus, the pulse width of the pulse current generated by FPGA can be adjusted per 20 ns. By the way, the clock of FPGA can be boosted through a phase-locked loop (PLL). All of the analog switches in the proposed sensor circuit and the pulse current flow through the MI sensor is generated by FPGA, therefore, the operating mode of the entire system we expected is schematically depicted in Fig.4.3.

The sensor circuit and the function of FPGA optimized together depending on the electronic component we used in our circuit. The operation of the proposed system is observed step by step through oscilloscope as shown in Fig.4.4. The entire system works as we expect. The sharp pulse corresponds to the rising and falling edge can be considered as the ringing signal.

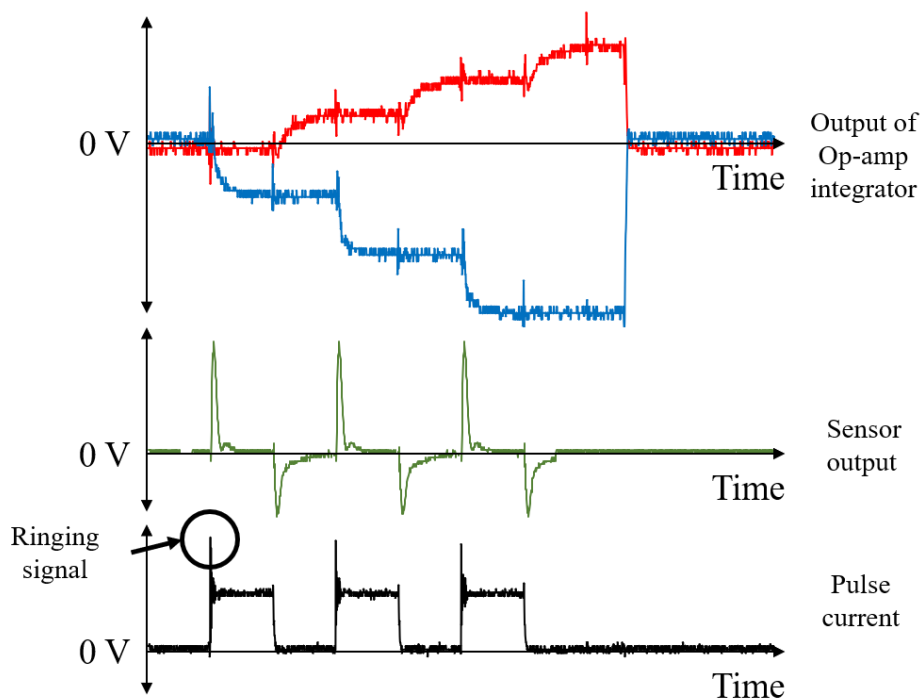


**Fig. 4.4 The actual timing chart of the proposed system.**

## 4.5 Magnetic field to output voltage characteristic

The performance of the MI gradiometer depending on the similarity in the sensitivity of the two MI sensors. Thus, in order to determine the sensitivity of two MI sensors, both the sensitivity of the measuring head and the reference head is obtained by taking the difference (Gain=1) between rising and falling edge, as shown in Fig.4.5. The difference in sensitivity of the two sensors is lower than 1%.

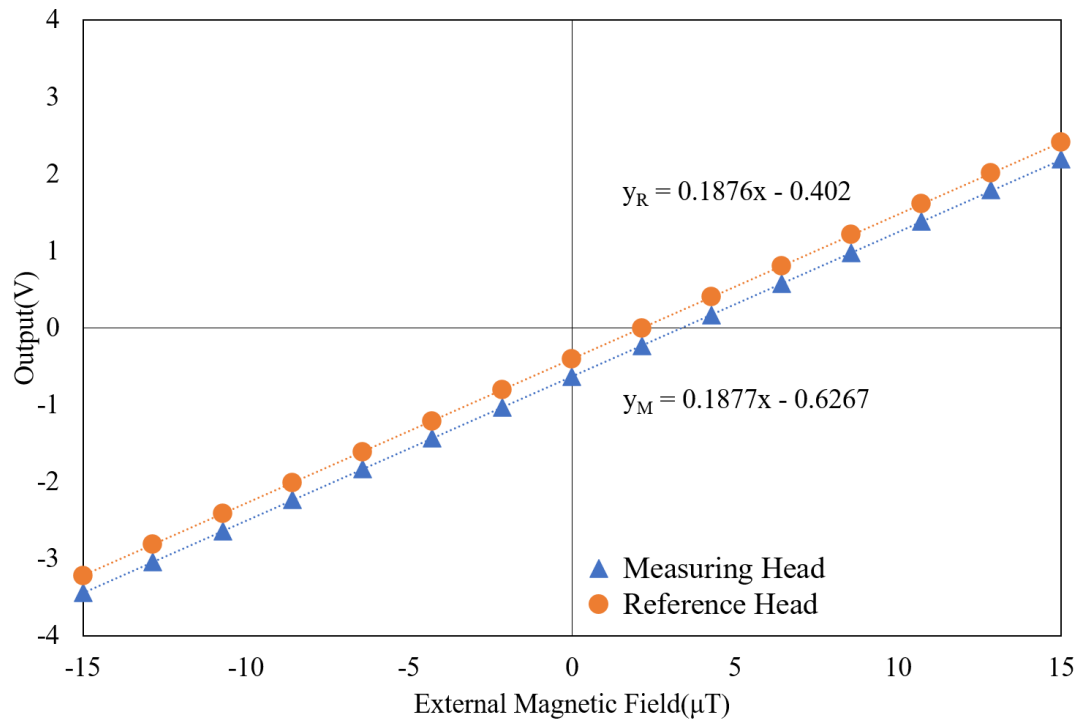


**Fig. 4.5 The magnetic field to output voltage characteristic of the proposed MI sensor.**

The proposed system in Fig.4.2 can be considered as a pair of MI gradiometers, one corresponds to the rising edge and another is falling edge. The measuring head in the MI gradiometer is set in a Helmholtz coil with an applied sinusoidal magnetic field with a frequency of 10 Hz and an amplitude of 3 μT. The output of two MI gradiometers equal in amplitude but inverted to each other as shown in Fig.4.6. It can be converted by ADC separately or used as a pair of differential signals. The output of the proposed system is obtained by taking the difference (Gain=100) between  $V_1$  and  $V_2$ .

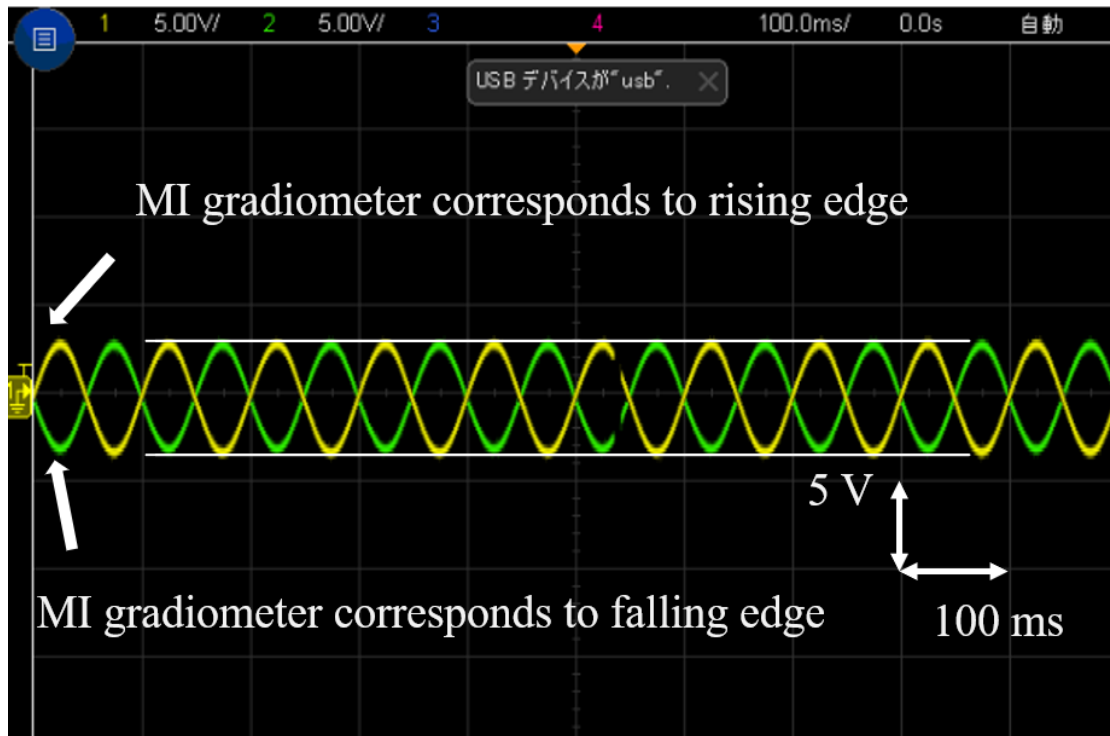


**Fig. 4.6** The response to AC magnetic signal of proposed MI gradiometer.

## 4.6 Weak magnetic detection

So as to study performance of weak magnetic signal detection of our system. The measuring head in the MI gradiometer is set in a Helmholtz coil with an applied sinusoidal magnetic field with a frequency of 10 Hz and an amplitude of 300 pT. Performance of weak magnetic field detection of the conventional system is investigated too for comparison as shown in Fig.4.7. Both outputs of the MI sensor system are recorded for 10s to obtain the response from 0.1 to 100 Hz. Signal-to-Noise Ratio (SNR) is defined as the ratio of signal power to noise power. The SNR of the conventional is approximate -20 dB, thus, the noise floor of the conventional system is 30 pT. As for the proposed system, the SNR is approximate -30 dB, which is approximate 10 pT. Output of proposed system is processed by a LPF (low pass filter), as depicted in Fig.4.8. The applied weak magnetic field is detected by the proposed system successfully.

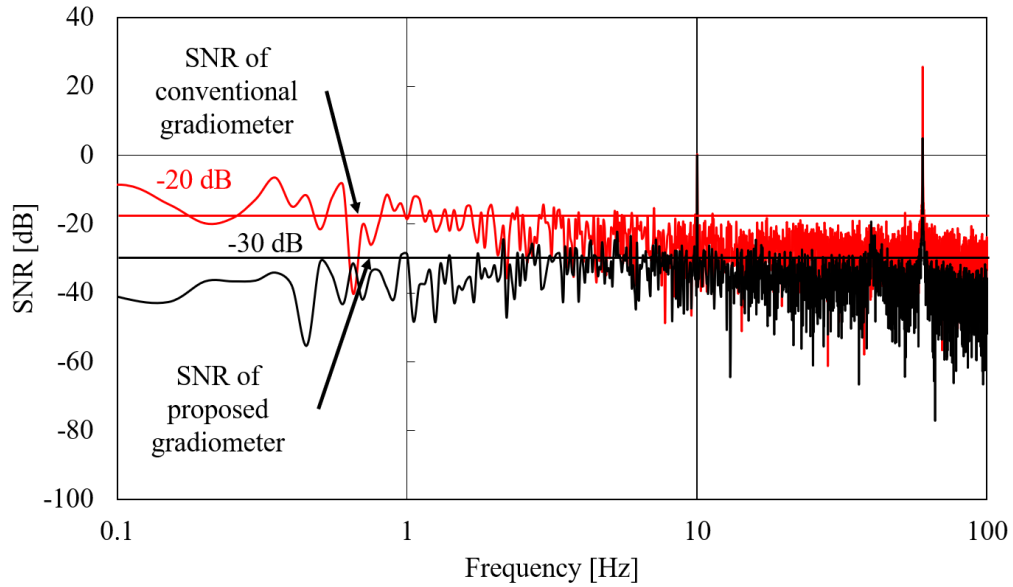


**Fig. 4.7 Comparison of the SNR between the proposed MI gradiometer (black) and the conventional MI gradiometer (red).**

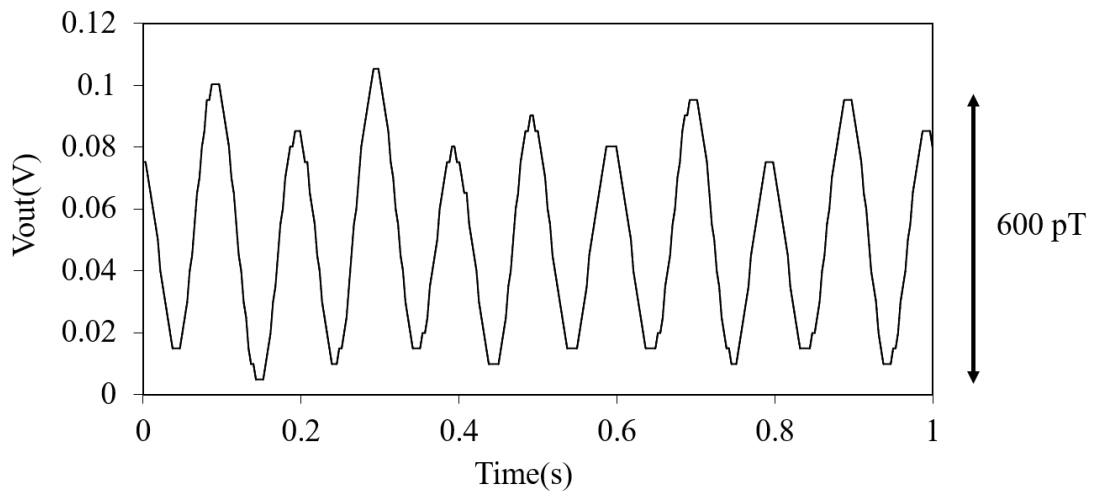


**Fig. 4.8 The weak magnetic signal detection of proposed gradiometer.**

## 4.7 Differential signaling

The common-mode noise carried by the differential signals in the proposed MI gradiometer can be suppressed by taking the difference between two MI gradiometers (Fig. 4.6), as shown in Fig.4.9. Thus, the resolution of the proposed MI gradiometer is better than the conventional MI gradiometer.

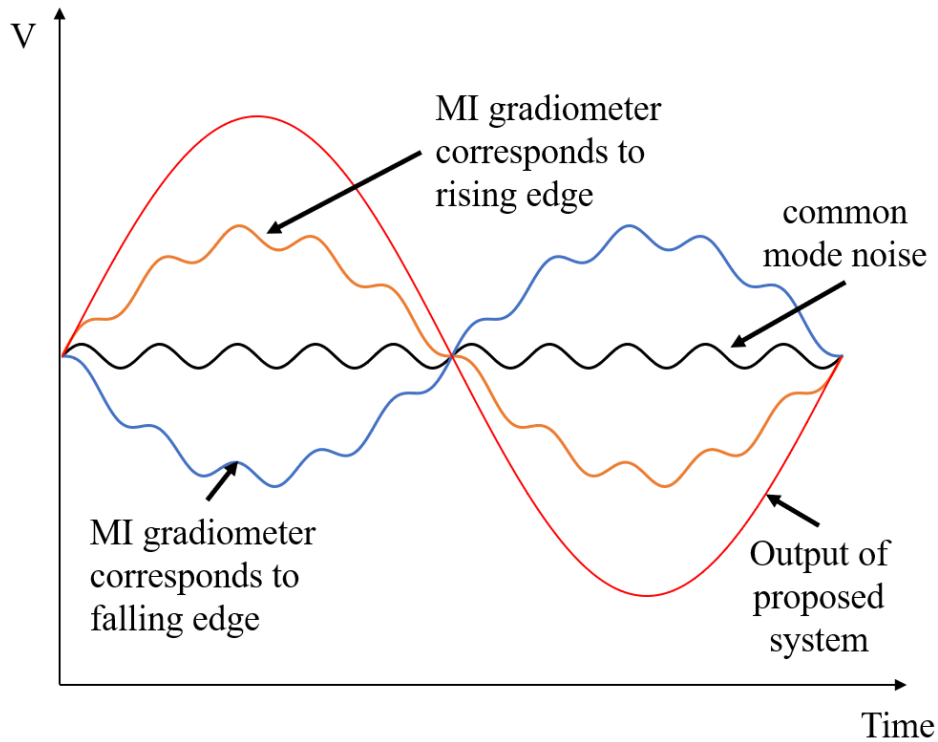


**Fig. 4.9 Elimination of noise by using differential signaling.**

## 4.8 System simplification

In order to sample the output of the sensor corresponds to the rising and falling edge, sensor circuit is more complex than the conventional sensor circuit, especially the proposed MI gradiometer. The ADC used in this research embedded with a digital filter, the output of the ADC transmitted to the FPGA after processed by the digital filter. The function of the digital filter is governed by the control signal from FPGA. The function of the digital filter is set to Averaging (as shown in appendix II) in this research, the operating frequency of ADC depends on the operating frequency of integrator.

In the future, ADC without latency output can be applied to simplify structure of our system, as depicted in Fig.4.10. Operation of simplified system is shown in Fig.4.11. The part function of the MI gradiometer achieved in the FPGA by taking the difference between *DATA1* and *DATA2*.

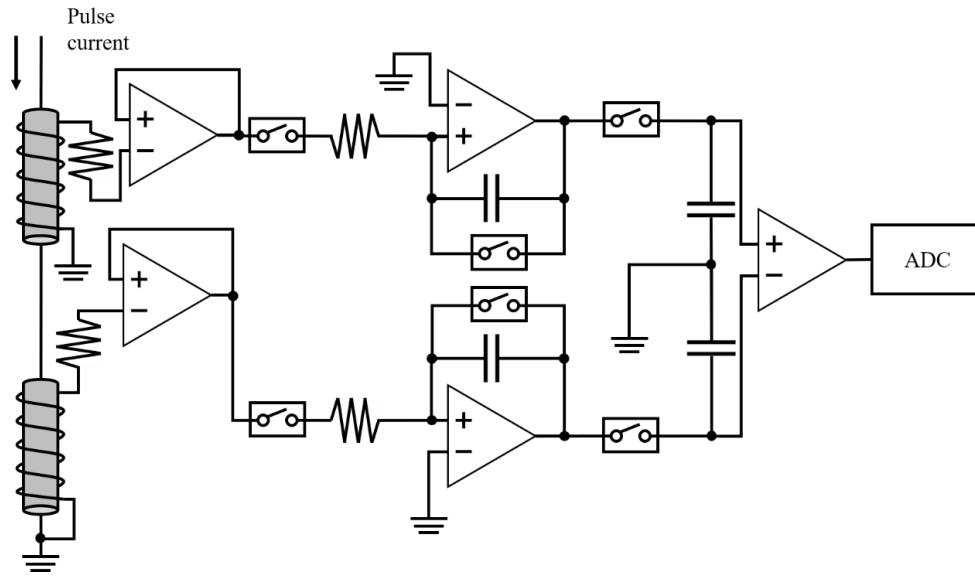


**Fig. 4.10 Structure of the simplified MI gradiometer.**

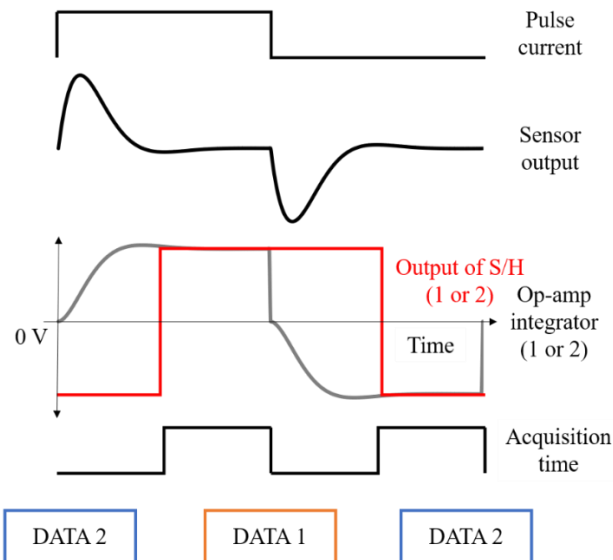


**Fig. 4.11 The timing chart of the simplified MI gradiometer.**

## 4.9 Summary

A novel approach to sample the MI sensor is developed in this chapter, the proposed MI gradiometer shows higher performance in resolution than the conventional MI gradiometer. On the other hand, the output of coil sampled by integrator without changing delay time of AS. Therefore, sensor system is easier to compatible with different types of MI sensors. The other characteristics of the proposed system will be discussed in the next chapter.



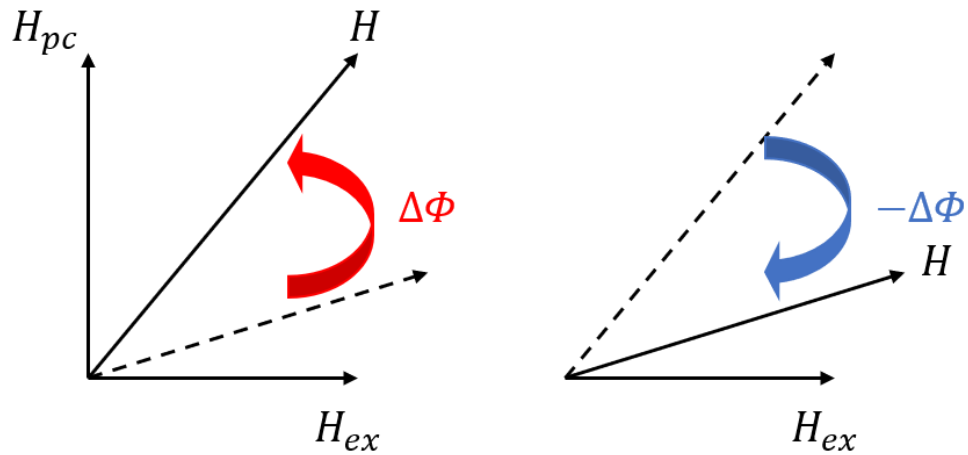


**Fig. 5.2 Magnetization rotation model of the surface layer of the amorphous wire.**

The pick-up coil consists of resistance, inductance, and parasitic capacitance between the coil, as shown in Fig.5.3(a). The magnetization in the pick-up coil only changes at the rising and falling edge, thus, owing to Faraday's law, the detection of the pick-up coil can be considered as a transient response with an induced voltage, the equivalent electrical model of the pick-up coil is depicted in Fig.5.3(b). [35] [36] [37]

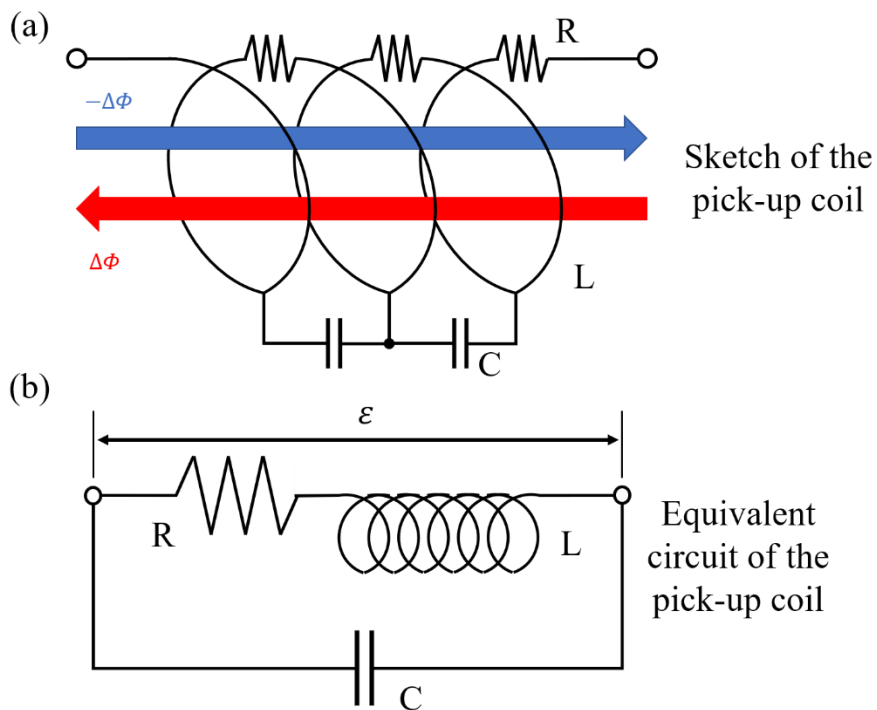


**Fig. 5.3 Equivalent circuit of the pick-up coil.**

Current-voltage relation of three components can be expressed as:

$$U_L = L \frac{di}{dt} = -\varepsilon \quad (5.1)$$

$$U_R = Ri \quad (5.2)$$

$$U_C = \frac{Q}{C} \quad (5.3)$$

$$i = \frac{dQ}{dt} = C \frac{dV}{dt} \quad (5.4)$$

The induced current  $i(t)$  through the capacitor is defined as:

$$V(t) = \frac{Q(t)}{C} = \frac{1}{C} \int_{t_0}^t i(t) dt + V(t_0) \quad (5.5)$$

The induced voltage in the inductance at rising and falling edge is defined as:

$$\varepsilon = -N\Delta\Phi \quad (5.6)$$

Thus, the current  $i(t)$  can be expressed as:

$$i = \frac{\frac{-L di}{dt} - \frac{Q}{C}}{R} \quad (5.7)$$

The governing differential equation can be obtained by using Kirchhoff's voltage law as:

$$U_L + U_R + U_C = 0 \quad (5.8)$$

$$L \frac{di}{dt} + Ri + \frac{Q}{C} = 0 \quad (5.9)$$

Taking the derivative of this equation, we obtain:

$$L \frac{d^2i}{dt^2} + R \frac{di}{dt} + \frac{1}{C} \frac{dQ}{dt} = 0 \quad (5.10)$$

$$L \frac{d^2i}{dt^2} + R \frac{di}{dt} + \frac{1}{C} i = 0 \quad (5.11)$$

We assume a solution of current with this form:

$$i(t) = e^{rt} \quad (5.12)$$

Substituting into the differential equation:

$$LC \frac{d^2i}{dt^2} + RC \frac{di}{dt} + \frac{dQ}{dt} = e^{rt}(LCr^2 + RCr + 1) \quad (5.13)$$

Therefore, the  $r$  in the equation of current  $i(t)$  can be express as:

$$r = \frac{-RC \pm \sqrt{R^2C^2 - 4LC}}{2LC} = -\frac{R}{2L} \pm \sqrt{\frac{R^2}{4L^2} - \frac{1}{LC}} \quad (5.14)$$

We set:

$$\delta = \frac{R}{2L} \quad (5.15)$$

$$\omega = \frac{1}{\sqrt{LC}} \quad (5.16)$$

The  $r$  can be expressed as:

$$r = -\delta \pm \sqrt{\delta^2 - \omega^2} \text{ or}$$

$$r = -\delta \pm j\sqrt{\omega^2 - \delta^2} \quad (5.17)$$

Here, we set:

$$\omega_0 = \sqrt{\omega^2 - \delta^2} \quad (5.18)$$

The initial conditions of the transient response at the start of the rising and falling edge can be express as:

$$i(0) = 0 \quad (5.19)$$

$$i'(0) = \frac{-\varepsilon}{L} \quad (5.20)$$

(1) If  $R < 2\sqrt{\frac{L}{C}}$ , ( $\omega > \delta$ ).

$r$  can be expressed as:

$$r = -\delta \pm j\omega_0 \left( \omega_0 = \sqrt{\omega^2 - \delta^2} \right) \quad (5.21)$$

Thus, the current is found by:

$$i(t) = e^{-\delta t} (A_1 \cos \omega_0 t + A_2 \sin \omega_0 t) \quad (5.22)$$

$$i(t) = e^{-\delta t} \sqrt{A_1^2 + A_2^2} \left( \frac{A_1}{\sqrt{A_1^2 + A_2^2}} \cos \omega_0 t + \frac{A_2}{\sqrt{A_1^2 + A_2^2}} \sin \omega_0 t \right) \quad (5.23)$$

Thus, we revised our proposed solution to have this form:

$$i(t) = k e^{-\delta t} \sin(\omega_0 t + \phi) \quad (5.24)$$

Here:

$$k = \sqrt{A_1^2 + A_2^2} \quad (5.25)$$

$$\tan \phi = \frac{A_1}{A_2} \quad (5.26)$$

Depending on the initial conditions, we obtain:

$$\phi = 0 \quad (5.27)$$

$$k = -\frac{\varepsilon}{L\omega_0} \quad (5.28)$$

The current can be defined as:

$$i(t) = -\frac{\varepsilon}{L\omega_0} e^{-\delta t} \sin(\omega_0 t) \quad (5.29)$$

Integral of the equation without constant can be calculated by using partial integration:

$$\int e^{-\delta t} \sin(\omega_0 t) dt = \int \sin(\omega_0 t) d \frac{e^{-\delta t}}{-\delta} \quad (5.30)$$

$$\int e^{-\delta t} \sin(\omega_0 t) dt = \frac{e^{-\delta t}}{-\delta} \sin(\omega_0 t) - \int \frac{e^{-\delta t}}{-\delta} \omega_0 \cos(\omega_0 t) dt \quad (5.31)$$

$$\int e^{-\delta t} \sin(\omega_0 t) dt = \frac{e^{-\delta t}}{-\delta} \sin(\omega_0 t) + \frac{\omega_0}{\delta} \int e^{-\delta t} \cos(\omega_0 t) dt \quad (5.32)$$

The second part of the right equation can be calculated by using partial integration again:

$$\begin{aligned} \int e^{-\delta t} \sin(\omega_0 t) dt = \\ \frac{e^{-\delta t}}{-\delta} \sin(\omega_0 t) + \frac{\omega_0}{\delta} \left( \frac{e^{-\delta t}}{-\delta} \cos(\omega_0 t) - \int \frac{e^{-\delta t}}{\delta} \omega_0 \sin(\omega_0 t) dt \right) \end{aligned} \quad (5.33)$$

Therefore:

$$\left( \frac{\delta^2 + \omega_0^2}{\delta^2} \right) \int e^{-\delta t} \sin(\omega_0 t) dt = \frac{e^{-\delta t}}{-\delta} \sin(\omega_0 t) - \frac{\omega_0}{\delta^2} e^{-\delta t} \cos(\omega_0 t) \quad (5.34)$$

$$\int e^{-\delta t} \sin(\omega_0 t) dt = -\frac{1}{\delta^2 + \omega_0^2} e^{-\delta t} (\delta \sin(\omega_0 t) + \omega_0 \cos(\omega_0 t)) \quad (5.35)$$

We revised the integral to have this form:

$$\int e^{-\delta t} \sin(\omega_0 t) dt = -\frac{1}{\sqrt{\delta^2 + \omega_0^2}} e^{-\delta t} \sin(\omega_0 t + \varphi) + c \quad (5.36)$$

Therefore, the voltage of the capacitor can be expressed as:

$$V(t) = \frac{\varepsilon}{LC\omega_0 \sqrt{\delta^2 + \omega_0^2}} e^{-\delta t} \sin(\omega_0 t + \varphi) + c \quad (5.37)$$

(2) If  $R > 2\sqrt{\frac{L}{C}}$ , ( $\omega < \delta$ ).

$r$  can be expressed as:

$$r_1 = -\delta + \sqrt{\delta^2 - \omega^2} \quad (5.38)$$

$$r_1 = -\delta - \sqrt{\delta^2 - \omega^2} \quad (5.39)$$

Thus, the current is found by:

$$i(t) = C_1 e^{r_1 t} + C_2 e^{r_2 t} \quad (5.40)$$

Depending on the initial conditions, we obtain:

$$C_1 = -C_2 = -\frac{\varepsilon}{L(r_1 - r_2)} \quad (5.41)$$

Therefore, the voltage of the capacitor can be expressed as:

$$V(t) = \frac{1}{C} \int i(t) dt = \int C_1 e^{r_1 t} - C_1 e^{r_2 t} dt = \frac{C_1}{C} \left( \frac{e^{r_1 t}}{r_1} - \frac{e^{r_2 t}}{r_2} \right) + c \quad (5.42)$$

(3) If  $R = 2\sqrt{\frac{L}{C}}$ , ( $\omega = \delta$ ).

$r$  can be expressed as:

$$r_1 = r_2 = -\delta \quad (5.43)$$

Thus, the current is found by:

$$i(t) = e^{rt}(C_1 + C_2 t) \quad (5.44)$$

Depending on the initial conditions, we obtain:

$$C_1 = 0 \quad (5.45)$$

$$C_2 = -\frac{\varepsilon}{L} \quad (5.46)$$

The current can be defined as:

$$i(t) = -\frac{\varepsilon}{L} t e^{rt} \quad (5.47)$$

Integral of the equation without constant can be calculated by using partial integration:

$$\int t e^{rt} dt = \frac{1}{r} t e^{rt} - \frac{1}{r^2} e^{rt} + c \quad (5.48)$$

Therefore, the voltage of the capacitor can be expressed as:

$$V(t) = \frac{1}{C} \int i(t) dt = -\frac{\varepsilon}{LC} \left( \frac{1}{r} t e^{rt} - \frac{1}{r^2} e^{rt} \right) + c \quad (5.49)$$

The operating of integrator is integral of entire output of pick-up coil, the result of integrator is calculated by:

$$V_{out} = -\frac{1}{R_i C_i} \int_0^{\infty} V(t) dt \quad (5.50)$$

The output voltage  $V(t)$  of the pick-up coil is the same form as the current  $i(t)$ . Thus, the integral of  $V_{out}$  of integrator is obtained easily. The result of integrator is related to parameters  $R$ ,  $L$ ,  $C$ ,  $R_i$ ,  $C_i$ , and turns of the pick-up coil. Depending on result acquire by impedance analyzer (ZA5405), the  $R$ ,  $L$ , and  $C$  dependence formulas maintain the same level from 400 turns to 800 turns. Therefore, the result of integrator is proportional to number of turns of pick-up coil. In addition to this, the sensitivity of

the rising and falling edge is equal to each other with reversed direction in the ideal model.

### 5.3 Magnetic field to voltage characteristic

Sensitivity of MI sensor with the different turns of the pick-up coil has been investigated in the proposed system, the pulse current is set to the frequency of 1M Hz with a duty cycle of 50%. The operating frequency of integrator set to 1M Hz as shown in Fig.5.4. Both the sensitivity corresponds to rising and falling edge is proportional to the turns of the pick-up coil. Integral of equation with an infinite time, but the operation time in integrator is only for several hundred nano sec. Thus, the sensitivity corresponds to rising and falling edge is close to each other.

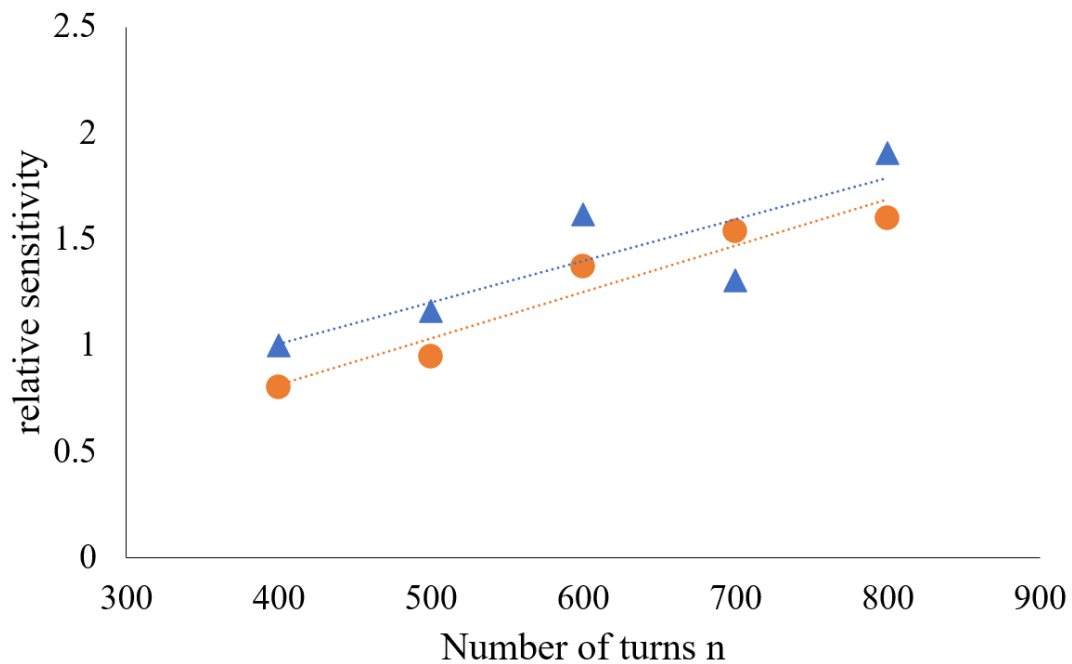


**Fig. 5.4 The influence of the turns of the pick-up coil on relative sensitivity. Relative sensitivity corresponds to the rising edge (Triangle) and the relative sensitivity corresponds to the falling edge (Circle).**

The sensitivity of the sensor that corresponds to the rising and falling edge has been investigated separately. The magnetometer is set in the Helmholtz coil, the applied DC magnetic field varies from  $-15 \mu\text{T}$  to  $15 \mu\text{T}$ . The pulse current is set to the frequency of 1M Hz with a duty cycle of 50%. The operating frequency of integrator set to 1M Hz, 500K Hz, and 333.3K Hz, as shown in Fig.5.5.

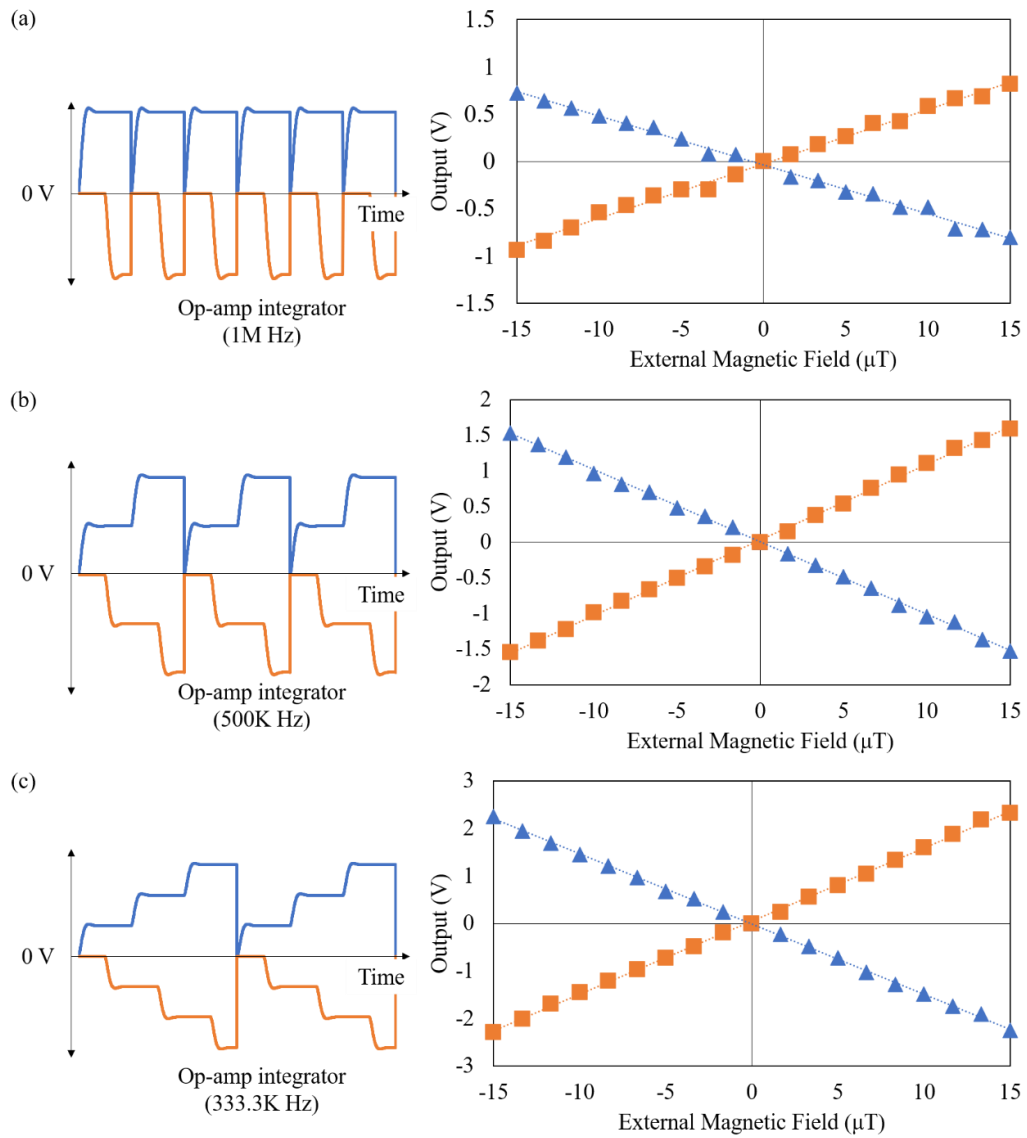


**Fig. 5.5** The magnetic field to output voltage characteristic of the proposed MI magnetometer. The output corresponds to rising (Triangle) and falling edge (Square). Operating frequency of the Op-amp integrator is (a) 1M Hz (b) 500K Hz (c) 333.3K Hz.

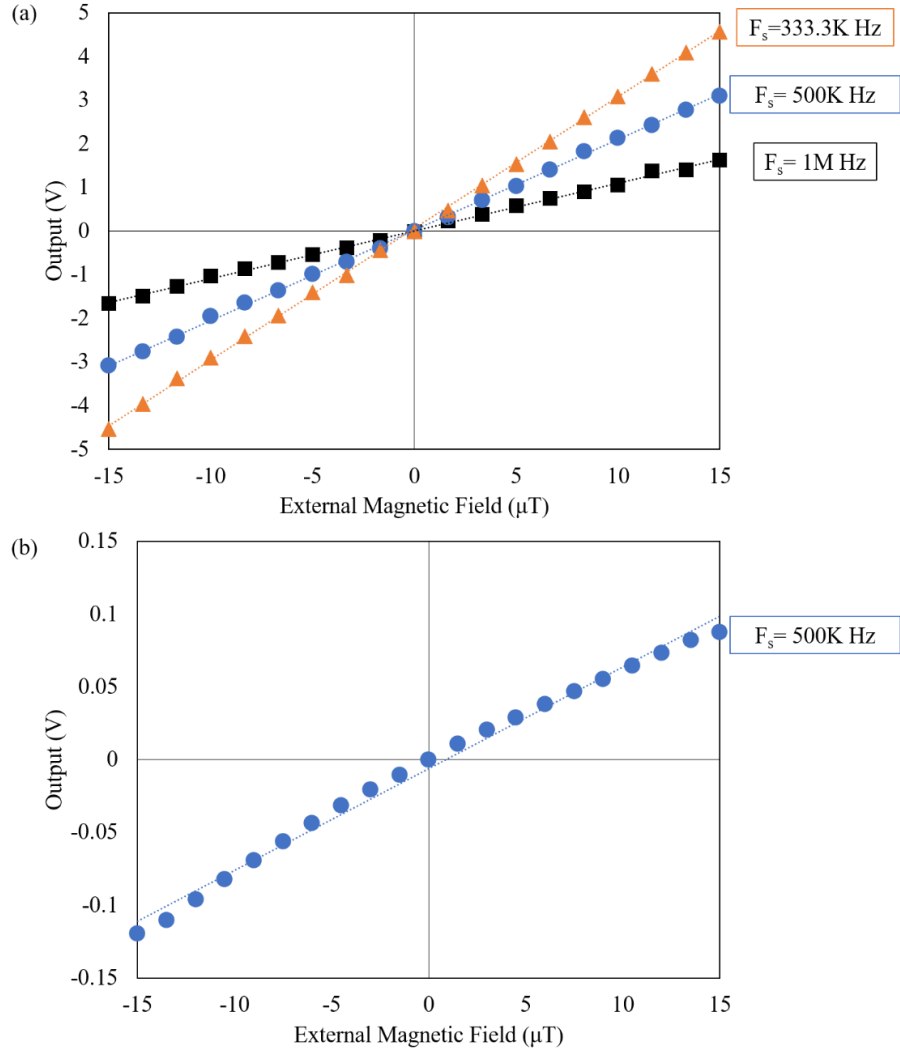


**Fig. 5.6 Comparison of the magnetic field to output voltage characteristic between the proposed (a) and conventional system (b).**

Result of integrator is:

$$V_{out} = -\frac{n}{RC} \int_0^t V_{in} dt \quad (5.51)$$

Thus, the sensitivity is proportional to the ratio  $n$  of the frequency of integrator to frequency of pulse current in the ideal model. On the other hand, the sensitivity is also governed by  $R$  and  $C$ , therefore, the output of the MI sensor is sampled and amplified through the Op-amp integrator at the same time. So as to maximize performance of proposed magnetometer, output of the proposed magnetometer with different sampling frequencies (Fig.5.5) of integrator obtained by taking difference (Gain=1) between the

output corresponds to rising and falling edge, as shown in Fig.5.6 (a). The sensitivity of the conventional S/H type magnetometer with the same MI sensor head has been investigated, as depicted in Fig.5.6 (b).

Sensitivity of sensor corresponds to rising and falling edge maintain the same level but inverted to each other. Both outputs of the sensor vary linearly with the applied magnetic field. Compare to the conventional S/H type magnetometer, the sensitivity corresponds to the falling edge of the proposed magnetometer improved significantly. [38] [31] On the other hand, the magnitude of output from integrator adjusted by changing sampling frequency of it. Generally, ADC exhibit a higher resolution with a lower sampling frequency, and a lower resolution with a higher sampling frequency, as shown in Tab.1 in chapter 2 and Appendix II. The full scale and the operating frequency of integrator in proposed system can be adjusted via the program. Thus, the sensor circuit and the ADC can be optimized together through the program.

The conventional system exhibits almost linear around zero magnetic field. [37] [39] [40] The linearity improved in the proposed system as shown in Fig.5.6.

## **5.4 Full scale and linearity**

In order to suit the different types of MI sensor, the frequency of pulse current set to 500K Hz with pulse width of 1000ns. The output corresponding to the rising edge and the falling edge can be separated. Both the Op-amp integrator is set to 500K Hz to survey the full scale and the linearity of sensor.

Full scale of MI sensor head with pT resolution (UNITIKA LTD. CoFeSiB, 1cm) has been investigated by using the proposed magnetometer. The output of the sensor that corresponds to rising and falling edge is recorded at the same time, as depicted in Fig.5.7. Applied magnetic field set from -135  $\mu$ T to 135  $\mu$ T. The linear dynamic range of both of the outputs of the MI sensor is approximately from -50  $\mu$ T to 50  $\mu$ T. Therefore, the linear dynamic range of the proposed magnetometer is also from -50  $\mu$ T to 50  $\mu$ T, as shown in Fig.5.8.

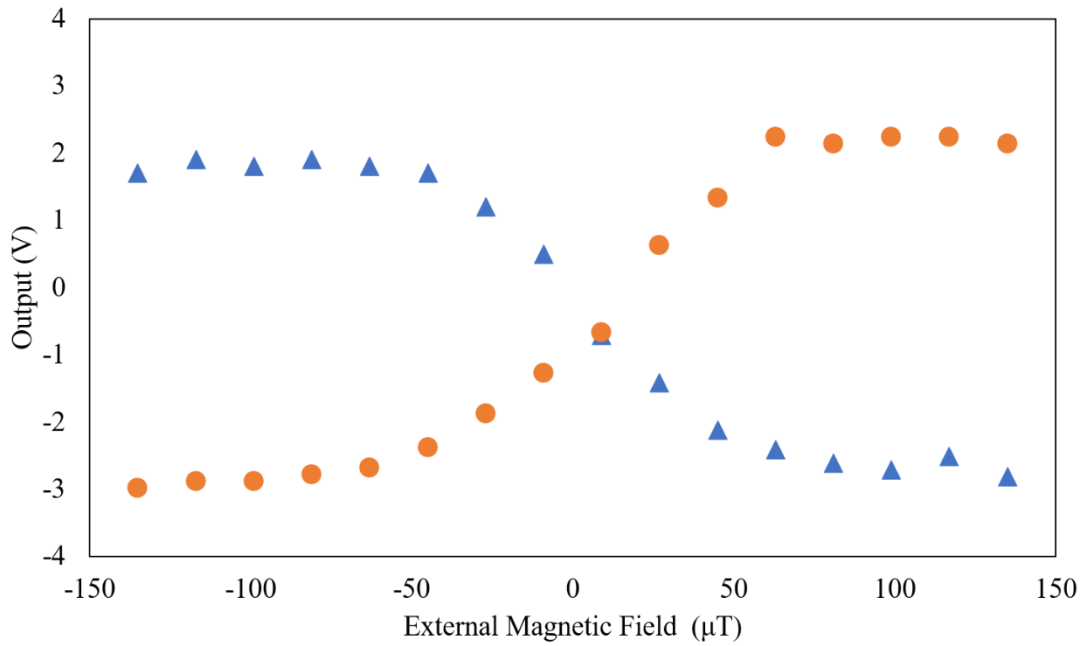


**Fig. 5.7** The magnetic field to output voltage characteristic of pT resolution MI sensor head. The output corresponds to the rising edge (Triangle) and falling edge (Circle).

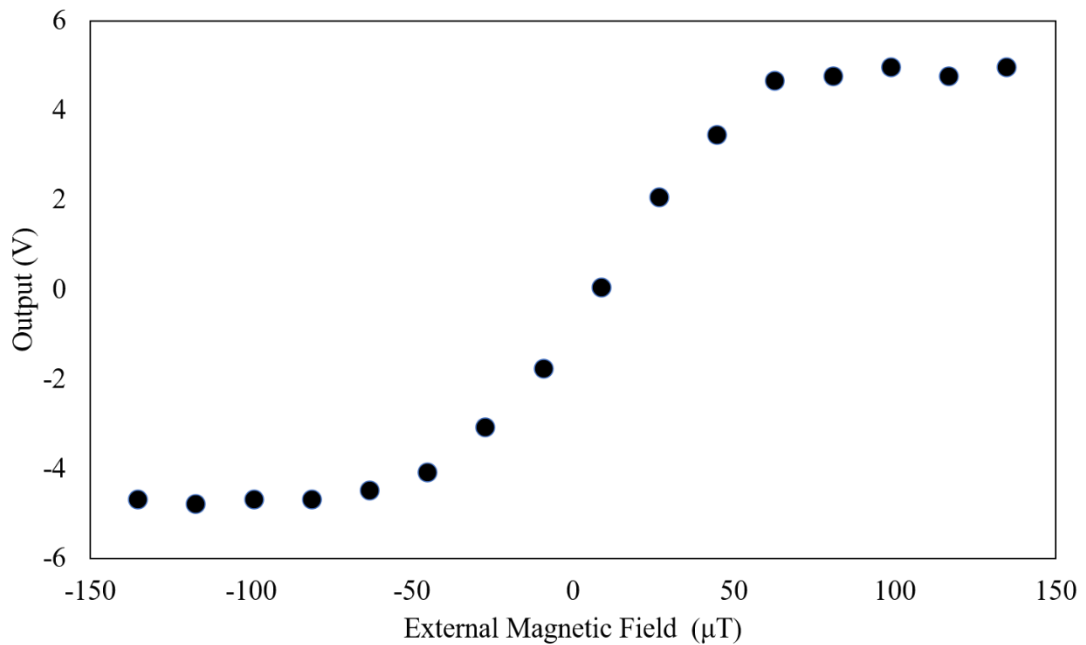


**Fig. 5.8** The magnetic field to output voltage characteristic of proposed MI magnetometer with pT resolution MI sensor head.

The MI sensor head with high linearity (NiFe, 1cm) is tested in the proposed sensor circuit to determine the capability of it. The operation of the entire system in this test is

the same as the test of the pT resolution MI sensor head. The maximum applied magnetic field generated by the Helmholtz coil used in this research is from  $-1500 \mu\text{T}$  to  $1500 \mu\text{T}$ . Thus, the scale from  $-1500 \mu\text{T}$  to  $1500 \mu\text{T}$  has been tested by using the high linearity MI sensor head. Both the outputs of the MI sensor shown linearity from  $-1500 \mu\text{T}$  to  $1500 \mu\text{T}$ , as shown in Fig.5.9.

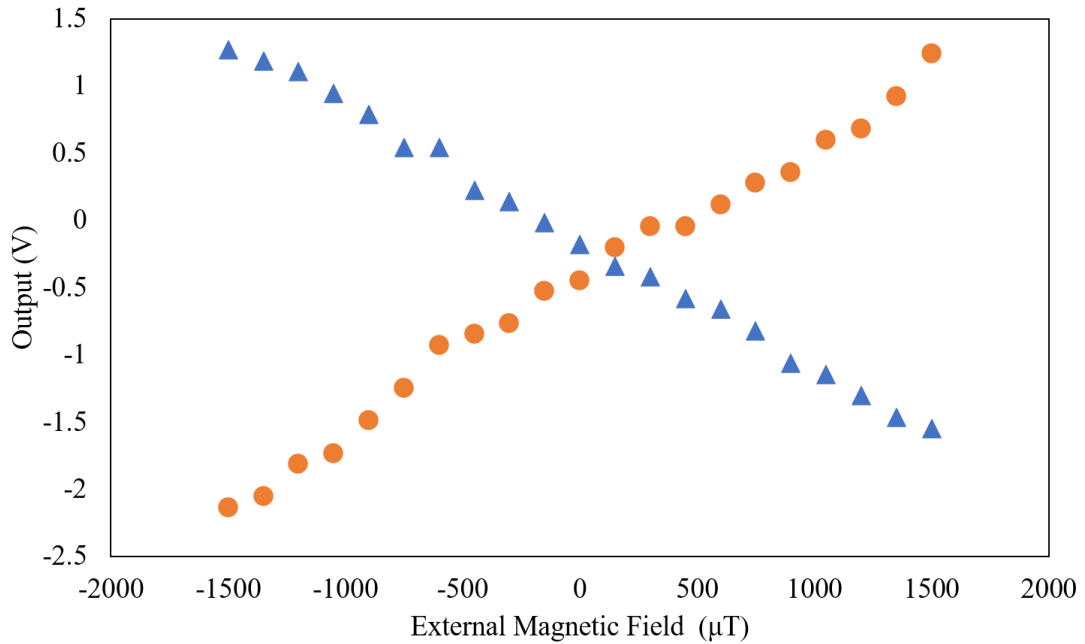


**Fig. 5.9 The magnetic field to output voltage characteristic of high linearity MI sensor head. The output corresponds to the rising edge (Triangle) and falling edge (Circle).**

Thus, the proposed sensor circuit with the high linearity MI sensor head exhibit linearity to the external magnetic field, as shown in Fig.5.10.

The linear dynamic range of the proposed MI magnetometer is depending on the type of MI sensor head (magnetic anisotropy, etc). The full scale of the proposed MI magnetometer is depending on power supply voltages, operating frequency of integrator, and capacitor  $C$  and resistance  $R$  of integrator.

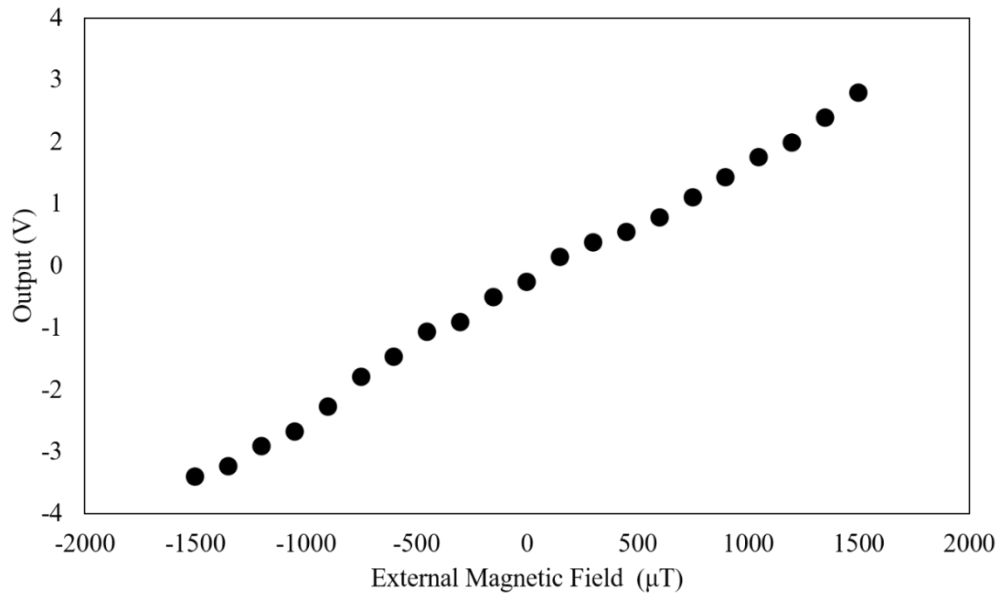


**Fig. 5.10 The magnetic field to output voltage characteristic of proposed MI magnetometer with high linearity MI sensor head.**

## 5.5 Noise spectral density

Noise of proposed circuit with three operating frequencies (as shown in Fig.5.5) of integrator has been investigated, as shown in Fig.5.11. Fig.5.12. Fig.5.13. The applied sinusoidal magnetic field is set to a frequency of 10 Hz and an amplitude of 300 pT. Both outputs of MI sensor system are recorded for 10s to obtain the frequency response from 0.1 to 100 Hz. Noise spectral density of proposed system with the operating frequency of integrator at 1M Hz is about 30 pT around 10 Hz, 500K Hz is about 15 pT, and 333.3K Hz is about 20 pT. According to experimental results, the noise level maintains the same level by adjusting the operation frequency of integrator. In other words, it is hard to suppress the noise of the proposed system by changing the operating frequency at the same time.

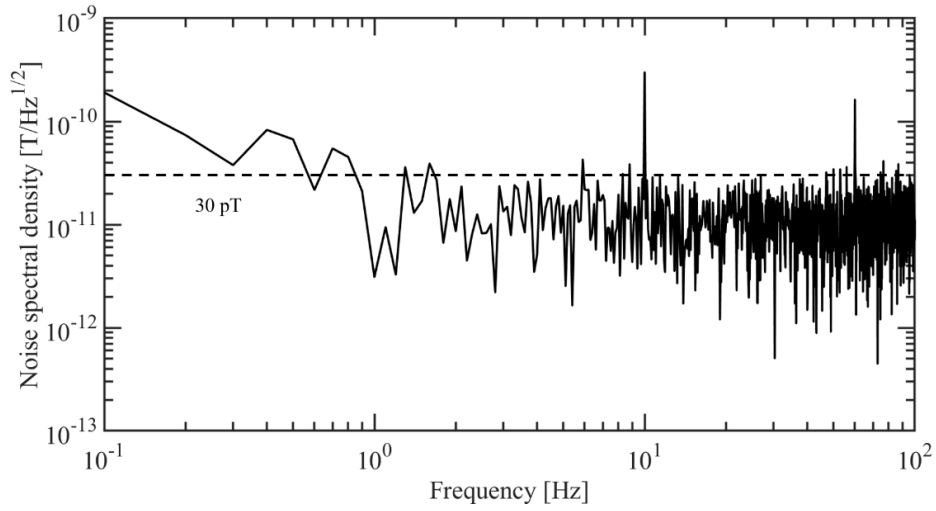


**Fig. 5.11** The noise spectral density of the proposed MI gradiometer (1M Hz).

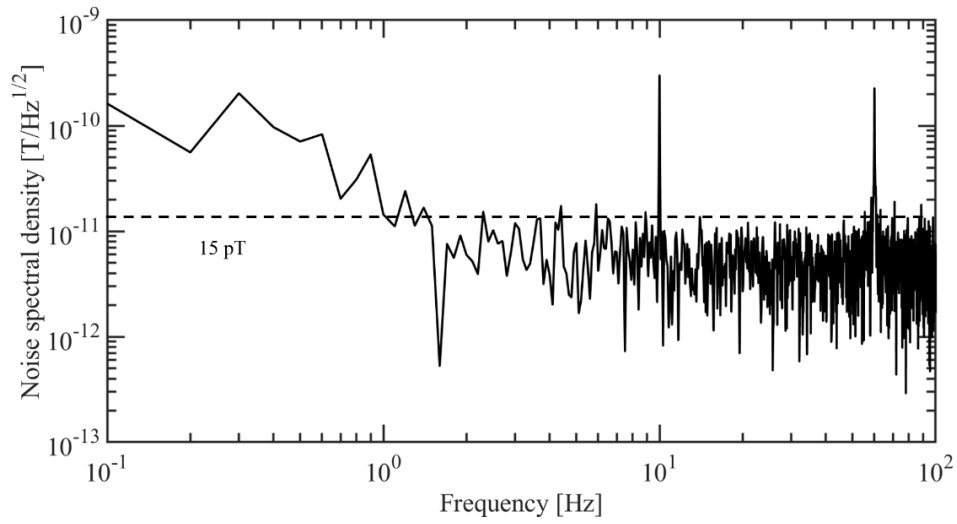


**Fig. 5.12** The noise spectral density of the proposed MI gradiometer (500K Hz).

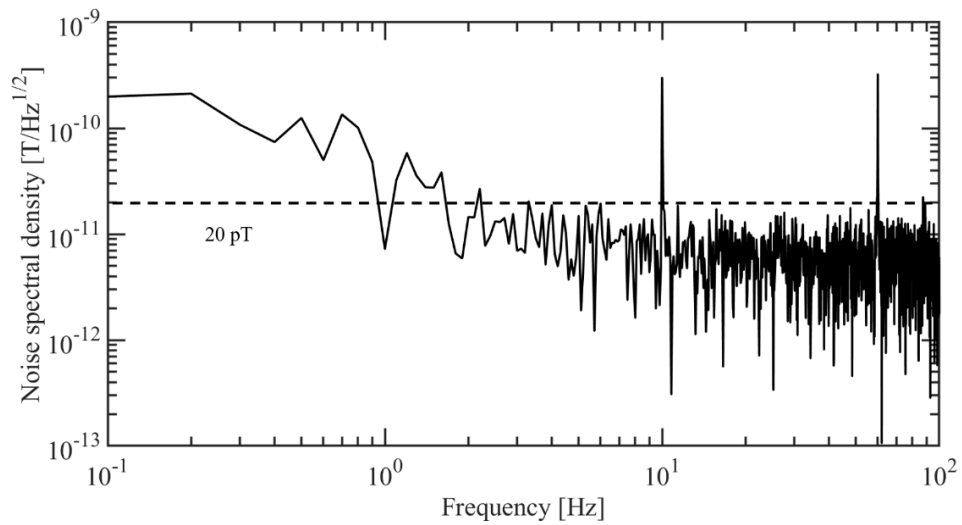


**Fig. 5.13** The noise spectral density of the proposed MI gradiometer (333.3K Hz).

## 5.6 Improvement of the proposed MI magnetometer

So as to obtain higher CMMR (common mode rejection ratio), the noise of corresponds to rising and falling edge has been investigated. The operating frequency of the pulse current and the operating frequency of integrator is set to 1M Hz. The applied sinusoidal magnetic field is set to a frequency of 10 Hz and an amplitude of 300 pT. Both outputs of MI sensor are recorded for 10s to obtain the response from 0.1 to 100 Hz. Depending on the result of frequency analysis, the noise level corresponds to rising edge approximately 20 pt/Hz at 10 Hz, the noise level corresponds to falling edge approximately 45 pt/Hz at 10 Hz, as shown in Fig.5.14.

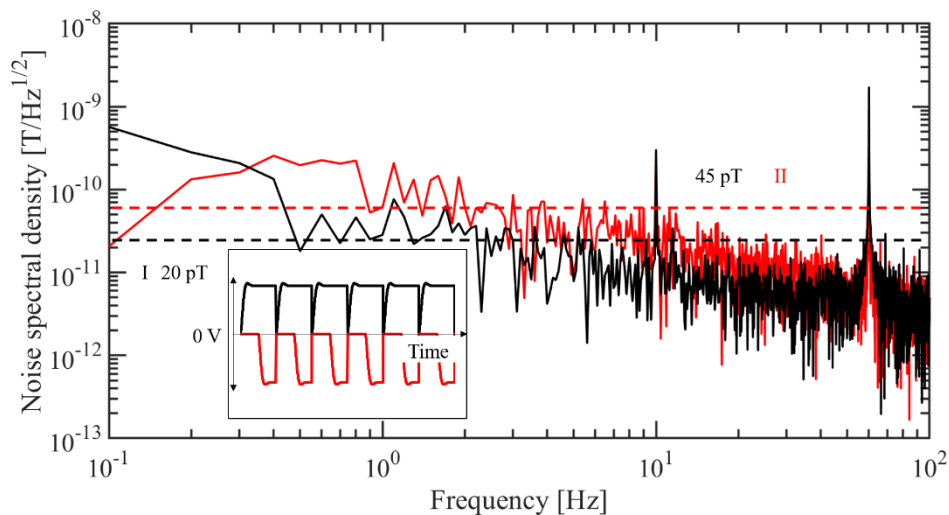


**Fig. 5.14 Noise spectral density of output corresponds to the rising edge (I) and falling edge (II).**

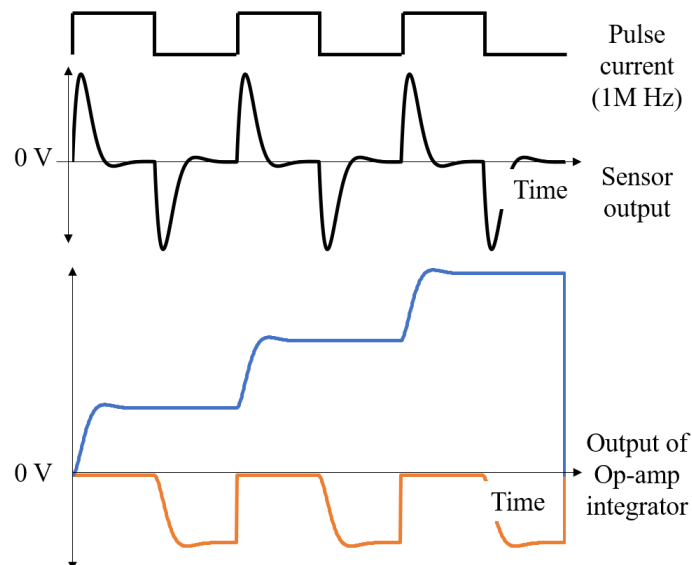


**Fig. 5.15 The improved timing chart of the proposed system.**

The magnetometer with the Op-amp integrator driven by a synchronized control signal maintains the same level of the noise level. So as to enhance the resolution of proposed magnetometer, the integrator is driven by an asynchronous frequency to increase CMMR, the operating frequency of integrator corresponds to rising edge is set to 333.3K Hz and falling edge is 1M Hz, as shown in Fig.5.15.

So as to compare conventional type and proposed type, the noise level of the same MI sensor head has been investigated in both measurement systems. According to the experimental results, the noise level can be suppressed by the proposed system with a different operating frequency of integrator. Noise spectral density of optimized system is 8 pT at 10 Hz, and 20 pT at 10 Hz in conventional system, as shown in Fig.5.16. Therefore, in the proposed magnetometer, both high resolution and high compatibility has been achieved.

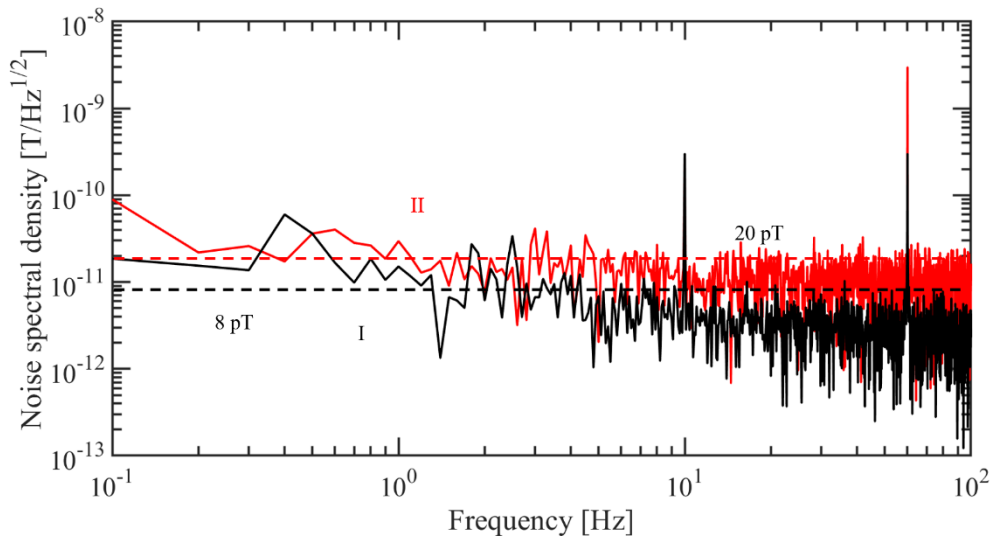


**Fig. 5.16 Noise spectral density of proposed MI magnetometer (I) and conventional MI magnetometer (II).**

## 5.7 System simplification

In order to simplify the sensor circuit of the proposed system, a simplified MI sensor

system has been developed as shown in Fig.5.17. The operation of the simplified system is depicted in Fig.5.18. OP-amp integrator used as a shared medium. Noise level of simplified MI sensor system is higher than the proposed system as shown in Fig.5.19, but the sensor circuit is more uncomplicated.

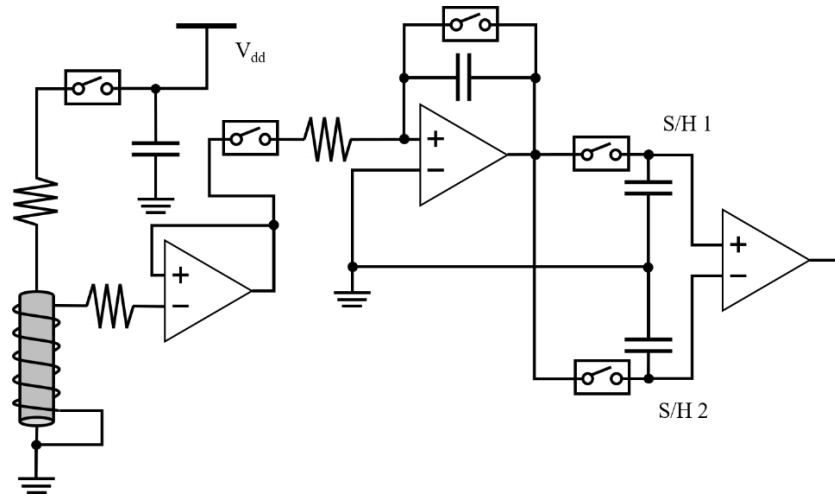


**Fig. 5.17 Structure of the simplified MI magnetometer.**

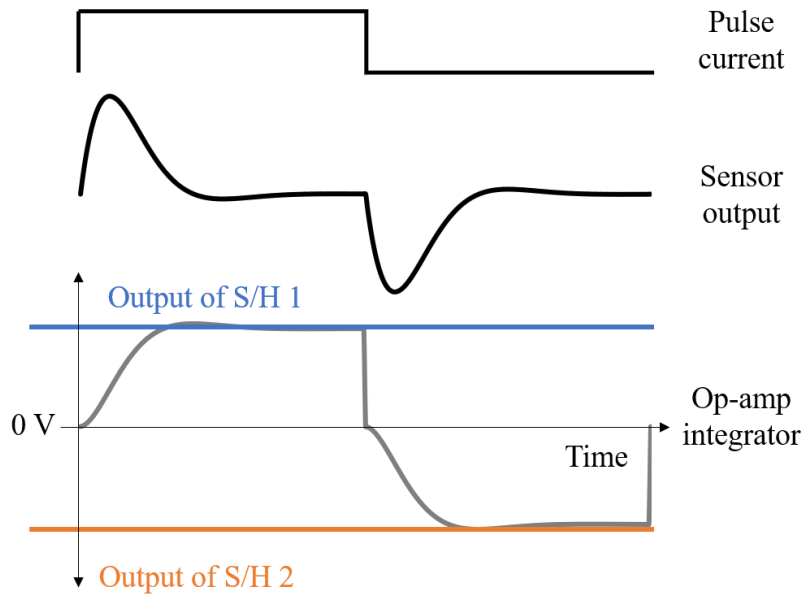


**Fig. 5.18 The timing chart of the simplified MI magnetometer.**

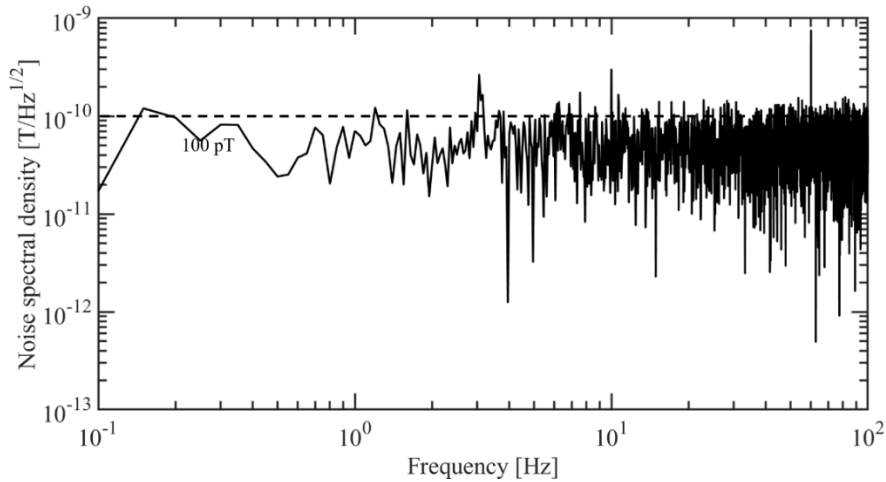


**Fig. 5.19** The noise spectral density of the simplified MI magnetometer.

## 5.8 Summary

A novel MI sensor system is discussed in this chapter. The operation of the proposed system can be governed by FPGA via CMOS/TTL IO Pin. Thus, the sensor circuit can be considered as a programmable circuit, in addition to this, the FPGA in the proposed system can be replaced by a CMOS IC circuit or ASIC. On the other hand, due to the capability of the programmable circuit, the sensitivity of the proposed system is governed by the FPGA, therefore, the common-mode noise suppressed by changing operation of AS in sensor circuit.

Depending on our calculation and experimental results, the output of the sensor corresponds to the rising and falling edge maintain same level of sensitivity in author proposed system, moreover, the sensitivity of the proposed system is proportional to the turns of pick-up coil, which different from conventional S/H system.

## Chapter 6 Conclusions and future outlook

### 6.1 Discussion

In the conventional sensor system, output of MI sensor sampled and processed (differential amplifier and analog bandpass filter) through the sensor circuit, output voltage of sensor system converted by an ADC. A programmable MI sensor system has been developed in this research. Both the sensor circuit (homemade) and ADC is controlled by an FPGA. Thus, the operation of the entire system can be synchronized via FPGA. DE10-Standard Development Kit (Terasic) with CYCLONE® V (Intel) used in this research. The ADC used in this research is a 32-Bit Over-Sampling ADC Multi-Application Demo board DC2390A-A (Analog Devices), as shown in Fig.6.1.



**Fig. 6.1 New experimental system.**

In recent years, numerous types of magnetic sensors invented based on different principles, SQUID and Optically pumped magnetometers (OPMs) [41] exhibit high performance but a bulky measurement system size and large power consumption.

Several kinds of small size magnetic sensors with high resolution (nT) has been developed due to the requirement of the information society, such as magnetoresistance sensor series (MR, AMR, GMR, TMR), Hall effect sensor, Fluxgate sensor, GMI sensor, as shown in Tab.2. [42]

Technology	Resolution [T]	Full scale [T]	Response speed	Power consumption	Length [m]
Hall effect	10 $\mu$	$\pm 1$	kHz	10mW	1~100 $\mu$
MR	10 $\mu$	$\pm 500$ m	MHz	10mW	1~100 $\mu$
GMR	1 $\mu$	$\pm 500$ m	MHz	10mW	1~100 $\mu$
Fluxgate	100 p	$\pm 20$ m	kHz	15VA	20~30m
MI	100 p	$\pm 20$ m	MHz	10mW	30 $\mu$ ~1m

**Tab. 2 Types of magnetic sensors and basic performance.**

In order to suit the requirement of the IoT in the future, there is a strong demand to develop a high-performance (pT) microsize magnetic sensor. Depending on the recent report, the elliptical planar type Hall effect (PHE) sensor with a size of 6mm x 1mm and exciting current with a frequency of 1.2K Hz exhibit an equivalent magnetic noise of 5pT at 10 Hz. [43] The TMR sensor also achieves pT resolution but with a size of 9mm x 9mm. [7] The Fluxgate sensor shows high resolution but with a big size (20mm~30mm), the size of the Fluxgate sensor can be reduced under 10mm due to MEMS technology. [44] [45] As for the MI sensor, the pT resolution sensor head is a wire with a length of 10mm and a diameter of dozens of  $\mu$ m. [46] The high response speed (GHz) MI sensor with a microsize (under 1mm x 1mm) and nT resolution was reported recently. [31] In order to achieve pT resolution, several types of magnetic sensors with a size of around 10 mm. The purpose of our research is to improve the sensor circuit with high resolution to suit different types of MI sensors.

## 6.2 Future work

In the future, the power consumption and the temperature stability of the proposed need to be investigated. The signal processing circuit such as the differential circuit needs to be improved. The proposed system is a programmable circuit, the entire system can be synchronized with ADC, therefore, the output of the multichannel MI sensor system can be converted by a single ADC through a signal channel selector controlled by analog switch.

### **6.3 Conclusion**

The MI sensor system is studied in this research. Since the MI sensor was invented, there are several kinds of MI sensor circuits based on different principles to achieve detection has been developed, such as diodes based peak detector, [47] analog switches based synchronous peak detection (S/H), [48] Root-Mean-Square (RMS)-to-DC converters, [49] the digital quadrature demodulators using a Software Defined Radio (SDR), [50] and high-frequency amplitude detector. [39] Each of these detection circuits has advantages and limitations. [39]

A stable MI sensor system based on the synchronous peak detection has been developed already and mass-produced for various applications, [51] in order to develop a practical MI sensor prototype, this research focuses on improving the synchronous peak detection circuit.

The synchronous peak detection circuit is an excellent design, but there are some limitations. In order to sample the output of high-speed response microsize MI sensor, capacitance  $C$  of the capacitor and the sampling timing of the S/H circuit need to be reduced. Therefore, the thermal noise of capacitor increased and resolution of MI sensor is limited. On the other hand, the sensitivity of the S/H type system depending on the sampling timing of the S/H circuit, in order to compatible with different types of MI sensors, the sampling timing of the S/H circuit needs to be optimized.

A novel MI sensor system has been developed in this research by replacing the synchronous peak detection with the full sampling method. Therefore, the entire output of the MI sensor acquired by the Op-amp integrator, there is no necessary to optimize

the delay time of AS to achieve synchronous peak detection, in other words, the proposed system can be applied to a different type of sensor easily. Depending on the result of frequency analysis, the resolution ( $\sim$  pT) of the proposed system is higher than the conventional system by using the same MI sensor head.

System	Proposed	Conventional	
Type	FPGA type	FPGA type	CMOS IC type
Signal Sampling	Full sampling	Peak sampling	
Sampling Timing	Pulse current	Output of sensor	
Programmable	○	△	×
Synchronize with ADC	Yes	Yes	No
Gain	$n/RC$	1	1
Approximation	$V = -\frac{n}{RC} \int_0^t V_{in}(t) dt$	$V(t) = V_p \left(1 - e^{-\frac{t}{\tau_0}}\right)$	
Resolution	Pico Tesla	Pico Tesla	
Compatibility	High	Limited	Low
Circuit	Complex	Simple	

**Tab. 3 Comparison between the proposed system and the conventional system.**

The sampling operation of the proposed system works for the entire sensor period. As for the conventional system, the sampling operation only works for the peak of waveform of MI sensor. Depending on the approximation of peak sampling, as shown in Tab.3, It is hard to sample the peak value in the high-speed mode. In other words, compared to the synchronous peak detection, the sampling window of the sampling circuit is extended in the proposed system, it is easier to acquire output of sensor in high-speed mode. The sampling timing of S/H circuit depending on output waveform of the MI sensor, sampling timing of the author proposed system depending on the operation of the pulse current of the sensor. Thus, there is no necessary to optimize the delay time for every types of sensors. In addition to this, the sensitivity of the proposed system Irrelevant to the sampling timing but only related to the MI sensor.

In the MI sensor prototype, the control signal of the proposed system generated by FPGA via CMOS/TTL interface, the FPGA can be replaced by CMOS IC circuit, ASIC, or smart systems to suit the smart sensor system in the future. The analog circuit of the

proposed system can be simplified by multiplexing the circuit. Due to the capability of the programmable sensor circuit, the sensitivity of the proposed system can be changed, and the common-mode noise can be further suppressed through the program. Compared with synchronous peak detection type MI sensor system, there are some decisive advantages due to the digital part structure, such as the flexibility of reconfiguration without any hardware modifications, system optimization with control signals only, and potential for integration.

## **Acknowledgements**

It is a great honor to study at the Nagoya University, Graduate School of Engineering. I would sincerely thank my honorific supervisor, Associate Professor, Dr. Tsuyoshi Uchiyama, offer me a great chance to be a part of his team and study in the MI sensor project, and his support of my Ph.D. research.

I would sincerely thank the professors and lab mates who helped me during the seven years of my life in Japan.

I would sincerely thank the professors for your guidance on my paper.

Thanks to my family for their understanding and financial support for my study abroad career.

Part of research was supported by the A-STEP of Japan Science and Technology Agency (Grant Reference Number: AS2915024R).

# Appendix

## I. Program of FPGA

```
module SK ( CLK,  
            reset,  
            LED,  
            SW,  
            SDI1,  
            MCLK1,  
            SDOA1,  
            SDOB1,  
            SCKA1,  
            SCKB1,  
            RDLA1,  
            RDLB1,  
            BUSY1,  
            DRL1,  
            SYNC1,  
            SDI2,  
            MCLK2,  
            SDOA2,  
            SDOB2,  
            SCKA2,  
            SCKB2,  
            RDLA2,  
            RDLB2,  
            BUSY2,  
            DRL2,  
            SYNC2,  
            CS,  
            sdik,  
            sdi,  
            DAC1,  
            DAC2,  
            SDO,  
            SYNC,  
            UART_TX,  
            PULSE,  
            S1,  
            S2,  
            INT_R,  
            );
```

```

input  CLK;
input  reset;
input  [9:0]SW;
input  SDO;
input  SDOA1;
input  SDOB1;
input  BUSY1;
input  DRL1;
input  SDOA2;
input  SDOB2;
input  BUSY2;
input  DRL2;
output SDI1;
output SCKA1;
output SCKB1;
output RDLA1;
output RDLB1;
output MCLK1;
output SYNC1;
output SDI2;
output SCKA2;
output SCKB2;
output RDLA2;
output RDLB2;
output MCLK2;
output SYNC2;
output [9:0]LED;
output CS;
output sdik;
output sdi;
output SYNC;
output UART_TX;
output [15:0]DAC1;
output [15:0]DAC2;
output PULSE;
output S1;
output S2;
output INT_R;
reg [31:0]DATA;
reg [3:0]data_in_1;
reg [3:0]data_in_2;
reg [3:0]data_in_3;
reg [3:0]data_in_4;
reg [3:0]data_in_5;

```

```

reg [3:0]data_in_6;
reg [3:0]data_in_7;
reg [3:0]data_in_8;
reg [3:0]data_in_9;
reg [3:0]data_in_10;
reg [3:0]data_in_11;
reg [3:0]data_in_12;
reg [0:0]drl;
reg [0:0]bus;
wire [31:0]DATA1;
wire [31:0]DATA3;
wire [31:0]DATA2;
wire [31:0]DATA4;
wire [6:0]data_UART_transfer_1;
wire [6:0]data_UART_transfer_2;
wire [6:0]data_UART_transfer_3;
wire [6:0]data_UART_transfer_4;
wire [6:0]data_UART_transfer_5;
wire [6:0]data_UART_transfer_6;
wire [6:0]data_UART_transfer_7;
wire [6:0]data_UART_transfer_8;
wire [6:0]data_UART_transfer_9;
wire [6:0]data_UART_transfer_10;
wire [6:0]data_UART_transfer_11;
wire [6:0]data_UART_transfer_12;
wire [0:0]bin2hex_clk;
wire [0:0]bin2hex_stop;
wire [15:0]P_c;
wire [15:0]int;
wire [0:0]M;
assign PULSE=(int<=49)?1'b1:1'b0;
assign S1=(int<=49)&(M<=1'b0)|(int>=49)&(int<=99)&(M>=1'b1)?1'b1:1'b0;
assign S2=(int<=49)&(M<=1'b0)|(int>=49)&(int<=99)&(M>=1'b1)?1'b1:1'b0;
assign INT_R=(P_c>=549)?1'b0:1'b1;

always @(negedge CLK)
begin
drl<=DRL1;
end
always @(negedge CLK)
begin
bus<=BUSY1;
end
CLK_SDI (.CLK_SDI_CLK(CLK),

```

```

        .CLK_reset(reset),
        .CLK_CS(CS),
        .CLK_sdi(sdi),
        .CLK_sdik(sdik),
        .SDI_LED(LED[9])
    );
ADC    (.CLK_ADC(CLK),
        .reset_ADC(reset),
        .BUSY_ADC(bus),
        .DRL_ADC(drl),
        .SDOA(SDOA1),
        .SDOB(SDOB1),
        .MCLK(MCLK1),
        .SCKA(SCKA1),
        .SCKB(SCKB1),
        .RDLA(RDLA1),
        .RDLB(RDLB1),
        .ADC_sdi(SDI1),
        .SYNC_ADC(SYNC1),
        .DATA_A_ADC(DATA1),
        .DATA_B_ADC(DATA3),
        .MI(P_c),
        .INT(int),
        .MU(M));
ADC    (.CLK_ADC(CLK),
        .reset_ADC(reset),
        .BUSY_ADC(BUSY2),
        .DRL_ADC(DRL2),
        .SDOA(SDOA2),
        .SDOB(SDOB2),
        .MCLK(MCLK2),
        .SCKA(SCKA2),
        .SCKB(SCKB2),
        .RDLA(RDLA2),
        .RDLB(RDLB2),
        .ADC_sdi(SDI2),
        .SYNC_ADC(SYNC2),
        .DATA_A_ADC(DATA2),
        .DATA_B_ADC(DATA4),);

//
reg [1:0]trans_timer;
reg [1:0]trans_timer0;
reg [7:0]sig;
always @(posedge CLK or negedge reset)

```

```

begin
if(!reset)
begin
DATA<=32'd0;
end
else
begin
case(bus)
1'b1:DATA<=DATA3+{1'b1,31'd0};
1'b0:DATA<=DATA;
endcase
end
end
//
always @(negedge CLK or negedge reset)
begin
case(M)
4'b0: begin
data_in_1<=DATA[31:28];
data_in_2<=DATA[27:24];
data_in_3<=DATA[23:20];
data_in_4<=DATA[19:16];
data_in_5<=DATA[15:12];
data_in_6<=DATA[11:8];

end
4'b1: begin
data_in_7<=DATA[31:28];
data_in_8<=DATA[27:24];
data_in_9<=DATA[23:20];
data_in_10<=DATA[19:16];
data_in_11<=DATA[15:12];
data_in_12<=DATA[11:8];
end
endcase
end
BIN2HEX (.CLK_BIN2HEX(CLK),
.data_bin(data_in_1),
.reset_BIN2HEX(reset),
.busy_BIN2HEX(CLK),
.data_hex(data_UART_transfer_1),
);
BIN2HEX (.CLK_BIN2HEX(CLK),
.data_bin(data_in_2),

```

```

        .reset_BIN2HEX(reset),
        .busy_BIN2HEX(CLK),
        .data_hex(data_UART_transfer_2),
    );
BIN2HEX ( .CLK_BIN2HEX(CLK),
        .data_bin(data_in_3),
        .reset_BIN2HEX(reset),
        .busy_BIN2HEX(CLK),
        .data_hex(data_UART_transfer_3),
    );

BIN2HEX ( .CLK_BIN2HEX(CLK),
        .data_bin(data_in_4),
        .reset_BIN2HEX(reset),
        .busy_BIN2HEX(CLK),
        .data_hex(data_UART_transfer_4),
    );

BIN2HEX ( .CLK_BIN2HEX(CLK),
        .data_bin(data_in_5),
        .reset_BIN2HEX(reset),
        .busy_BIN2HEX(CLK),
        .data_hex(data_UART_transfer_5),
    );

BIN2HEX ( .CLK_BIN2HEX(CLK),
        .data_bin(data_in_6),
        .reset_BIN2HEX(reset),
        .busy_BIN2HEX(CLK),
        .data_hex(data_UART_transfer_6),
    );

BIN2HEX ( .CLK_BIN2HEX(CLK),
        .data_bin(data_in_7),
        .reset_BIN2HEX(reset),
        .busy_BIN2HEX(CLK),
        .data_hex(data_UART_transfer_7),
    );

BIN2HEX ( .CLK_BIN2HEX(CLK),
        .data_bin(data_in_8),
        .reset_BIN2HEX(reset),
        .busy_BIN2HEX(CLK),
        .data_hex(data_UART_transfer_8),
    );

BIN2HEX ( .CLK_BIN2HEX(CLK),

```

```

        .data_bin(data_in_9),
        .reset_BIN2HEX(reset),
        .busy_BIN2HEX(CLK),
        .data_hex(data_UART_transfer_9),
    );
BIN2HEX    ( .CLK_BIN2HEX(CLK),
        .data_bin(data_in_10),
        .reset_BIN2HEX(reset),
        .busy_BIN2HEX(CLK),
        .data_hex(data_UART_transfer_10),
    );
BIN2HEX    ( .CLK_BIN2HEX(CLK),
        .data_bin(data_in_11),
        .reset_BIN2HEX(reset),
        .busy_BIN2HEX(CLK),
        .data_hex(data_UART_transfer_11),
    );
BIN2HEX    ( .CLK_BIN2HEX(CLK),
        .data_bin(data_in_12),
        .reset_BIN2HEX(reset),
        .busy_BIN2HEX(CLK),
        .data_hex(data_UART_transfer_12),
    );

UART    (.CLK_UART(CLK),
        .reset_UART(reset),
        .UART_tx(UART_TX),
        .CLKusb(bin2hex_clk),
        .data_UART_1(data_UART_transfer_1),
        .data_UART_2(data_UART_transfer_2),
        .data_UART_3(data_UART_transfer_3),
        .data_UART_4(data_UART_transfer_4),
        .data_UART_5(data_UART_transfer_5),
        .data_UART_6(data_UART_transfer_6),
        .data_UART_7(data_UART_transfer_7),
        .data_UART_8(data_UART_transfer_8),
        .data_UART_9(data_UART_transfer_9),
        .data_UART_10(data_UART_transfer_10),
        .data_UART_11(data_UART_transfer_11),
        .data_UART_12(data_UART_transfer_12),
        .uart_drl(drl),
    );
assign LED[0]=1'b1;
endmodule

```

## II. Characteristics of ADC with Averaging digital filter

FILTER TYPE	DOWN-SAMPLING FACTOR (DF)	OUTPUT DATA RATE		-3dB BANDWIDTH		FILTER LENGTH	GROUP DELAY (f <sub>SAMPL</sub> = 1Msps)	DYNAMIC RANGE (dB)	NOISE (μV RMS)
		f <sub>SAMPL</sub> = 1Msps	f <sub>SAMPL</sub> = 1.024Msps	f <sub>SAMPL</sub> = 1Msps	f <sub>SAMPL</sub> = 1.024Msps				
Averaging	2	500ksps	512ksps	227.34kHz	232.8	2	1μs	106.4	17.57
	4	250ksps	256ksps	113.85kHz	116.58kHz	4	2μs	109.1	12.87
	8	125ksps	128ksps	55.75kHz	57.08kHz	8	4μs	112.2	9.09
	16	62.5ksps	64ksps	27.73kHz	28.40kHz	16	8μs	115.5	6.19
	32	31.25ksps	32ksps	13.85kHz	14.18kHz	32	16μs	118.4	4.42
	64	15.6ksps	16ksps	6.92kHz	7.09kHz	64	32μs	121.2	3.21
	128	7.8ksps	8ksps	3.46kHz	3.54kHz	128	64μs	124	2.31
	256	3.9ksps	4ksps	1.73kHz	1.77kHz	256	128μs	127.4	1.56
	512	1.95ksps	2ksps	865.13Hz	885.89Hz	512	256μs	130.4	1.1
	1024	977sps	1ksps	432.57Hz	442.95Hz	1024	512μs	133.1	0.81
	2048	488sps	500sps	216.28Hz	221.47Hz	2048	1024μs	136	0.58
	4096	244sps	250sps	108.14Hz	110.74Hz	4096	2048μs	138.3	0.44
	8192	122sps	125sps	54.07Hz	55.37Hz	8192	4096μs	141.4	0.31
	16384	61sps	62.5sps	27.04Hz	27.68Hz	16384	8192μs	143.3	0.25

**Tab. 4 Performance of the programmable digital filter.**

## Publication

	Title	Journal/Conference	Authors
<b>Papers</b>			
I	Sensor Circuit for a Full-Sample Magneto-Impedance Gradiometer	IEEE Magnetics Letters, Volume: 10, 8109004, (2019)	Ke Shi* Tsuyoshi Uchiyama
II	A full sample-type magneto-impedance (MI) magnetometer with programmable circuit for high compatibility	AIP Advances Volume: 10, 015026, (2020), Published Online	Ke Shi* Tsuyoshi Uchiyama
<b>International conference</b>			
I	Sensor Circuit for a Full-Sample Magneto-Impedance Gradiometer	International Baltic Conference on Magnetism 2019, Russia, Poster, (2019)	Ke Shi* Tsuyoshi Uchiyama
II	A full sample-type magneto-impedance (MI) magnetometer with programmable circuit for high compatibility	The 64th Annual Conference on Magnetism and Magnetic Materials (MMM 2019), America, Oral, (2019)	Ke Shi* Tsuyoshi Uchiyama
<b>Conference in Japan</b>			
I	高分解能ADコンバーターTADを用いたデジタル差分型MIグラジオメータ	日本磁気学会(2016), 日本, 口頭発表	Ke Shi* T. Takiya Tsuyoshi Uchiyama
II	FPGAを用いた適応型MIセンサシステムの開発とADコンバータの最適化	日本磁気学会(2019), 日本, 口頭発表	Ke Shi* Tsuyoshi Uchiyama

## References

- [1] J.E.Lenz, "A review of magnetic sensors," Proceedings of the IEEE, Volume: 78, Issue: 6, pp. 973-989, DOI: 10.1109/5.56910, 1990.
- [2] X. Y. Liu; et al., "Overview of spintronic sensors with internet of things for smart living," IEEE transactions on magnetics, Volume: 55, Issue: 11, No: 0800222, DOI: 10.1109/TMAG.2019.2927457, 2019.
- [3] G. Mathias, Fundamentals of magnetism, ISBN: 978-3-540-31152-2: Springer, 2008.
- [4] A. Fert; et al., "Giant Magnetoresistance of (001)Fe/(001)Cr magnetic superlattices," Physical review letters, Volume: 61, Issues: 21, pp. 2472-2475, DOI: <https://doi.org/10.1103/PhysRevLett.61.2472>, 1988.
- [5] P. Grünberg; et al., "Enhanced magnetoresistance in layered magnetic structures with antiferromagnetic interlayer exchange," Physical review B, Volume. 39, Issue: 7, pp. 4828-4830, DOI:<https://doi.org/10.1103/PhysRevB.39.4828>, 1989.
- [6] F. Kou; M. Oogane; Y. Ando, "Development of highly sensitive terrestrial sensor using TMR junctions," Journal of the magnetics society of japan, Volume: 32, Issue: 3, pp. 361-365, DOI: <https://doi.org/10.3379/msjmag.32.361>, 2008.
- [7] J. G. Deak; et al., "Tunneling magnetoresistance sensor with pT level 1/f magnetic noise," AIP advances, Volume: 7, Issue: 5, No: 056676, DOI: <https://doi.org/10.1063/1.4978465>, 2017.
- [8] G. Musmann, Fluxgate Magnetometers for space research, ISBN: 9783839137024: BoD – Books on Demand, 2010.
- [9] R. C. Snare, A history of vector magnetometry in space, DOI: <https://doi.org/10.1002/9781118664391.ch12>: Geophysical Monograph Series, 1998.
- [10] 毛利 佳年雄, 磁気センサ理工学—センサの原理から電子コンパス応用まで 増補版, ISBN: 978-4-339-00882-1: コロナ社, 2015.
- [11] 登 三浦, "磁場中の計測技術," 計測と制御, 26 巻, 6 号, pp. 520-527, DOI: <https://doi.org/10.11499/sicejl1962.26.520>, 1987.
- [12] 上原 弦, 賀戸 久, "超伝導量子干渉素子(SQUID)技術の現状," 応用物理, 61 巻 (1992) 5 号, pp. 464-471, DOI: <https://doi.org/10.11470/oubutsu1932.61.464>, 1992.
- [13] 松田 瑞史, 栗城 眞也, "SQUID の原理とシステム化技術," 応用物理, 71 巻, 12 号, pp. 1534-1537, DOI: <https://doi.org/10.11470/oubutsu1932.71.1534>, 2002.
- [14] J. Malmivuo, Bioelectromagnetism, Theory of biomagnetic measurements, Chapter: 12, pp.227-254: Oxford university press, 1995.
- [15] A. S. Edelstein; J. Burnette; G. A. Fischer, "Advances in magnetometry through miniaturization," Journal of vacuum science & technology A, Volume: 26, Issue: 4, pp. 757-762, DOI: <https://doi.org/10.1116/1.2841516>, 2008.
- [16] S. Zuo; H. Heidari; D. Farina; K. Nazarpour, "Miniaturized magnetic sensors for implantable magnetomyography," Advanced materials technologies, Volume: 5, Issue: 6, No: 2070033, DOI: <https://doi.org/10.1002/admt.202000185>, 2020.
- [17] K. Mohri; M. Yamamoto; T. Uchiyama., "Application topics of amorphous wire CMOS IC

Magneto-Impedance micromagnetic sensors for I-o-T smart society,” *Journal of sensors*, Volume: 2019, No: 8285240, DOI: 10.1155/2019/8285240, 2019.

- [18] K. Mohri; T. Uchiyama; L. V. Panina, “Recent advances of amorphous wire cmos ic magneto-impedance sensors: innovative high-performance micromagnetic sensor chip,” *Journal of sensors*, Volume: 2015; No: 718069, DOI: <https://doi.org/10.1155/2015/718069>, 2015.
- [19] E. P. Harrison; G. L. Turney; H. Rowe, “Electrical properties of wires of high permeability,” *Nature*, Volume: 135, Issue: 3423, pp. 961, DOI:<https://doi.org/10.1038/135961a0>, 1935.
- [20] E. P. Harrison; G. L. Turney; H. Rowe; H. Gollop, “The electrical properties of high permeability wires carrying alternating current,” *Proceedings of the royal society of london. series a, mathematical and physical sciences*, Volume 157, Issue 891, pp. 451-479, DOI: <https://doi.org/10.1098/rspa.1936.0208>, 1936.
- [21] K. Mohri; T. Kohsawa; K. Kawashima; H. Yoshida; L. V. Panina, “Magneto-inductive effect (MI effect) in amorphous wires,” *IEEE transactions on magnetics*, Volume: 28, Issue: 5, pp. 3150-3152, DOI: 10.1109/20.179741, 1992.
- [22] L. V. Panina; K. Mohri; K. Bushida; M. Noda, “Giant magneto-impedance and magneto-inductive effects in amorphous alloys (invited),” *Journal of applied physics*, Volume: 76, Issue: 10, pp. 6198-6203, DOI:<https://doi.org/10.1063/1.358310>, 1994.
- [23] S. Sandacci; D. Makhnovskiy; L. V. Panina; K. Mohri; Y. Honkura, “Off-diagonal impedance in amorphous wires and its application to linear magnetic sensors,” *IEEE transactions on magnetics*, Volume: 40, Issue: 6, pp. 3505-3511, DOI: 10.1109/TMAG.2004.835676, 2004.
- [24] Y. Arai; M. Ikeno, “A time digitizer CMOS gate-array with a 250 ps time resolution,” *IEEE journal of solid-state circuits*, Volume: 31, Issue: 2, pp. 212-220, DOI: 10.1109/4.487998, 1996.
- [25] Y. Arai; T. Ohsugi, “TMC-a CMOS time to digital converter VLSI,” *IEEE transactions on nuclear science*, Volume: 36, Issue: 1, pp. 528-531, DOI: 10.1109/23.34495, 1989.
- [26] T. Watanabe; T. Mizuno; Y. Makino, “An all-digital analog-to-digital converter with 12- $\mu$ V/LSB using moving-average filtering,” *IEEE journal of solid-state circuits*, Volume: 38, Issue: 1, pp. 120-125, DOI: 10.1109/JSSC.2002.806263, 2003.
- [27] T. Watanabe; S. Yamauchi; T. Terasawa, “A 0.0027-mm<sup>2</sup> 9.5-bit 50-MS/s all-digital A/D converter TAD in 65-nm digital CMOS,” 2009 16th IEEE international conference on electronics, circuits and systems - (ICECS 2009), pp. 271-274, DOI: 10.1109/ICECS.2009.5410988, 2010.
- [28] 渡辺 高元, 中村 三津男, 増田 純夫, “An All-Digital A/D converter for fast conversion with 4-TAD parallel construction using moving-average filtering,” *Denso technical review / デンソーテクニカルレビュー 編*, Volume: 10, Issue: 2, pp. 65-69, Reprinted from “Proceedings of the 8th International workshop on ADC modelling and testing (2003.9) in Perugia”, 2005.
- [29] S.Tajima; Y. Okuda; T. Watanabe; H. Aoyama; M. Yamamoto; T. Uchiyama, “High-resolution magneto-impedance sensor with TAD for low noise signal processing,” *IEEE transactions on magnetics*, Volume: 50, Issue: 11, No: 4005504, DOI:

10.1109/TMAG.2014.2332178, 2014.

- [30] S.Tajima; Y. Okuda; T. Watanabe; H. Aoyama; M. Yamamoto; T. Uchiyama, "High-resolution magneto-impedance sensor with TAD for low noise signal processing," *IEEE transactions on magnetics*, Volume: 50, Issue: 11, No: 4005504, DOI: 10.1109/TMAG.2014.2332178, 2014.
- [31] Y. Honkura; S. Honkura, "The development of a micro-coil-on-ASIC type GSR sensor driven by GHz pulse current," *Journal of magnetism and magnetic materials*, Volume 513, No: 167240, <https://doi.org/10.1016/j.jmmm.2020.167240>, 2020.
- [32] H. Heidari; E. Bonizzoni; G. Umberto; M. Franco, "A CMOS current-mode magnetic hall sensor with integrated front-end," *IEEE transactions on circuits and systems I: regular papers*, Volume: 62, Issue: 5, pp.1270-1278, DOI: 10.1109/TCSI.2015.2415173, 2015.
- [33] S. Kawahito; A. Cerman; Y. Tadokoro, "A digital fluxgate magnetic sensor interface using sigma-delta modulation for weak magnetic field measurement," *IMTC/2002. Proceedings of the 19th IEEE Instrumentation and measurement technology conference (IEEE Cat. No.00CH37276)*, pp. 257-260, DOI: 10.1109/IMTC.2002.1006849, 2002.
- [34] K. Chang; et al., "Two-Pole Integrator SQUID readout electronics with high slew rate and small closed-loop frequency response peak," *IEEE transactions on applied superconductivity*, Volume: 25, Issue: 4, No: 1602903, DOI: 10.1109/TASC.2015.2427361, 2015.
- [35] M. Ozaki; et al, "Magnetic Search Coil (MSC) of Plasma Wave Experiment (PWE) aboard the Arase (ERG) satellite," *Earth planets and space*, Volume: 70, No: 76, DOI: 10.1186/s40623-018-0837-1, 2018.
- [36] B. Esteban; J. R. Riba; G. Baquero; C. Ferrater, "An eddy-current-based sensor for preventing knots in metallic wire drawing processes," *Nondestructive testing and evaluation*, Volume: 26, Issue: 02, pp. 169-180, DOI: <https://doi.org/10.1080/10589759.2010.545128>, 2011.
- [37] L. V. Panina; et al., "Off-diagonal magnetoimpedance in amorphous microwires for low-field magnetic sensors," *Physica status solidi (A) applications and materials*, Volume: 213, Issue: 2, pp. 341-349, DOI: 10.1002/pssa.201532578, 2015.
- [38] T. Uchiyama; N. Hamada; C. M. Cai, "Highly sensitive CMOS magnetoimpedance sensor using miniature multi-core head based on amorphous wire," *IEEE transactions on magnetics*, Volume: 50, Issue: 11, No: 4005404, DOI: 10.1109/TMAG.2014.2326658, 2014.
- [39] A. Asfour; M. Zidi; J. P. Yonnet, "High frequency amplitude detector for GMI magnetic sensors," *Sensors 2014*, Volume: 14, Issue: 12, pp. 24502-24522, DOI: <https://doi.org/10.3390/s141224502>, 2014.
- [40] K. Ludek, "Nonlinear magnetoimpedance in field- and stress-annealed amorphous ribbons," *IEEE transactions on magnetics*, Volume: 46, Issue: 2, pp. 428-431, DOI: 10.1109/TMAG.2009.2032836, 2010.
- [41] E. B. Alexandrov, "Recent progress in optically pumped magnetometers," *Physica scripta*, Volume: 2003, No: T105, DOI: 10.1238/Physica.Topical.105a00027, 2006.

- [42] 田所嘉昭, “計測・センサ工学,” オーム社, ISBN-10 : 4274132064, 2000.
- [43] H. Nhalil; T. Givon, “Planar Hall effect magnetometer with 5 pT resolution,” *IEEE sensors letters*, Volume: 3, Issue: 12, No: 2501904, DOI: 10.1109/LESENS.2019.2947681, 2019.
- [44] R. Pavel, “Advances in fluxgate sensors,” *Sensors and actuators A: physical*, Volume: 106, Issues: 1-3, pp. 8-14, [https://doi.org/10.1016/S0924-4247\(03\)00094-3](https://doi.org/10.1016/S0924-4247(03)00094-3), 2003.
- [45] O. Dezuari; E. Belloy; S. E. Gilbert; M. A. M. Gijs, “Printed circuit board integrated fluxgate sensor,” *Sensors and actuators A: physical*, Volume: 81, Issues: 1–3, pp. 200-203, DOI: [https://doi.org/10.1016/S0924-4247\(99\)00088-6](https://doi.org/10.1016/S0924-4247(99)00088-6), 2000.
- [46] T. Uchiyama; K. Mohri; S. Nakayama, “Measurement of spontaneous oscillatory magnetic field of guinea-pig smooth muscle preparation using pico-tesla resolution amorphous wire magneto-impedance sensor,” *IEEE transactions on magnetics*, Volume: 47, Issue: 10, pp. 3070-3073, DOI: 10.1109/TMAG.2011.2148165, 2011.
- [47] K. Mohri; T. Uchiyama; L. P. Shen; C. M. Cai; L. V. Panina, “Amorphous wire and CMOS IC-based sensitive micro-magnetic sensors (MI sensor and SI sensor) for intelligent measurements and controls,” *Journal of magnetism and magnetic materials*, Volume: 249, Issues: 1–2, pp. 351-356, DOI: [https://doi.org/10.1016/S0304-8853\(02\)00558-9](https://doi.org/10.1016/S0304-8853(02)00558-9), 2002.
- [48] N. Kawajiri; M. Nakabayashi; C. M. Cai; K. Mohri; T. Uchiyama, “Highly stable MI micro sensor using CMOS IC multivibrator with synchronous rectification [for automobile control application],” *IEEE transactions on magnetics*, Volume: 35, Issue: 5, pp. 3667-3669, DOI: 10.1109/20.800625, 1999.
- [49] M. Zidi; A. Asfour; J. P. Yonnet, “RMS-to-DC converter for GMI magnetic sensor,” *IEEE transactions on magnetics*, Volume: 51, Issue: 1, No: 4001604, DOI: 10.1109/TMAG.2014.2357073, 2015.
- [50] P. S. Traoré; A. Asfour; J. P. Yonnet, “Off-diagonal GMI sensors with a software-defined radio detector: implementation and performance,” *IEEE transactions on magnetics*, Volume: 53, Issue: 4, No: 4000907, DOI: 10.1109/TMAG.2016.2625803, 2016.
- [51] Y. Honkura, “Development of amorphous wire type MI sensors for automobile use,” *Journal of magnetism and magnetic materials*, Volume: 249, Issues: 1–2, pp. 375-381, [https://doi.org/10.1016/S0304-8853\(02\)00561-9](https://doi.org/10.1016/S0304-8853(02)00561-9), 2002.